Weathering pathways and limitations in biogeochemical models: Application to Earth system evolution

Benjamin J. W. Mills

September 2012

A thesis submitted to the School of Environmental Sciences of the University of East Anglia in partial fulfilment of the requirements for the degree of Doctor of Philosophy

Abstract

Current biogeochemical box models for Phanerozoic climate are reviewed and reduced to a robust, modular system, allowing application to the Precambrian. It is shown that stabilisation of climate following a Neoproterozoic snowball Earth should take more than 10^7 years, due to long-term geological limitation of global weathering rates. The timescale matches the observed gaps between extreme glaciations at this time, suggesting that the late Neoproterozoic system was oscillating around a steady state temperature below the snowball threshold. In the model, the period of disequilibrium following snowball glaciations is characterised by elevated ocean nutrient and organic burial rates, providing fair correlation with available geochemical proxies. Extending the analysis to consider carbon removed from the ocean via seafloor carbonatization does not result in a significant reduction in stabilisation time.

Model timeframe is extended over the last 2Ga. Predicted oxygen concentration is shown to depend on the balance between terrestrial and seafloor weathering, which alters the global nutrient delivery rate and therefore global productivity. Under reasonable assumptions, broad predictions for Proterozoic climate fall within, or close to the bounds imposed by geological proxies. A mechanism for atmospheric oxygenation over Earth history is proposed: the combination of declining mantle heat flux and increasing continental area, aided by colonising land biota, results in a steadily increasing ocean nutrient supply, driving increasing rates of organic carbon burial.

Methods currently used for assessing Phanerozoic O_2 assume only terrestrial weathering fluxes, and are found to give unreasonable results when applied to the Precambrian. Phanerozoic predictions from the model developed here show a significant reduction in the large oxygen peak at 300Ma found in previous studies. This is due to consideration of terrestrial and seafloor weathering balance, and to the longer model timeframe - which allows prediction of crustal abundances in the Cambrian, rather than assuming present day conditions.

I would like to thank my supervisors Andrew Watson, Tim Lenton and Colin Goldblatt. I could not have wished for a more dedicated and friendly supervisory team. Thanks also to Richard Boyle for his continuing contributions, and to everybody else who has answered questions, commented on manuscripts and supplied data, code or papers: Bob Berner, Noam Bergman, Graham Shields, Claire Belcher, Galen Halverson, Nathan Sheldon and Martin Johnson to name but a few. Thanks to the examiners of this thesis, Andy Ridgwell and Mark Claire, for raising useful criticisms, and to the anonymous reviewers of my first paper for the same. Thanks to Phil Underwood for answering all my computing queries. Thanks to the UEA for the Dean's studentship, and for sending me to international conferences. Thanks to the stewards aboard the RRS James Cook who made writing a thesis on a ship a surprisingly enjoyable experience.

Lastly, but most importantly, thanks to all the excellent friends, family, musicians, footballers, aggressive cycling enthusiasts and special people who have helped make the last 4 years so varied and enjoyable.

Benjamin Mills.

Contents

1 Introduction

1.1 Earth history

1.1.1 Formation, age and geological time

The Earth was formed around 4.5 billion years ago (Ga) in a circumstellar disc around the young Sun. In models of planetary formation, gas and fine dust surrounding the stellar body undergoes accretion to first form small planetesimals, then larger planetary embryos, which eventually collide to form planets (e.g. Chambers (2004)). The process takes between 10-100 million years (Myr). It is thought that the Moon was formed near the end of Earth's accumulation (Canup and Asphaug, 2001) from mass ejected during a collision between the young Earth and a Mars-sized body (Benz et al., 1986; Hartmann and Davis, 1975).

The oldest crustal material known is dated to 4.3-4Ga (Bowring and Williams, 1999; ONeil et al., 2008) and there is some evidence for existence of continental crust and oceans on the Earth at 4.4Ga (Wilde et al., 2001), however, lack of preservation causes the abundance of rocks to decline exponentially with age (Garrels and Mackenzie, 1969), making early-Earth material scarce today. Figure 1.1.1 shows the currently agreed chronostratigraphic timeline (ICS, 2012) alongside proxy data for atmospheric composition and the timing of glacial periods.

1.1.2 Earth's surface environment

Multiple geologic proxies are used to infer climatic conditions throughout Earth history. The composition of the atmosphere is thought to have changed significantly since the formation of the planet, but appears to have remained suitable for life (Kasting, 1989). Pillow basalts dated to 3.8Ga provide the first direct evidence of liquid water (Polat et al., 2002), which is a requirement for all known organisms. This indicates that the ocean was not completely frozen at this time, however, placing constraints on early Earth temperature is very difficult. The limited geological evidence suggests a temperate-to-hot Archean climate, but also indicates glacial periods (Kasting and Ono, 2006). Temperature extremes at the local or global level may have been crucial to the origin of life (Bada et al., 1994; Wachtershauser, 1998; Schwartzman,

1999).

The Sun is known to have increased in luminosity over time, implying that with contemporary greenhouse gas concentration and planetary albedo, global temperature would be expected to be well below the freezing point of water in the Archean (Sagan and Mullen, 1972). Thus it has been inferred that concentrations of greenhouse gasses must have been higher on the early Earth (Kasting, 1993). Evidence from paleosols (Rye et al., 1995), mineralogy of banded iron formations (Rosing et al., 2010) and ancient river gravels (Hessler et al., 2004) place Archean CO_2 concentration between 1-100 times PAL (present atmospheric level), which is lower than the concentration required to maintain clement surface temperature after consideration of other plausible greenhouse gasses (Haqq-Misra et al., 2008). It has been suggested that lower planetary albedo due to the lack of continents (Rosing et al., 2010) and increased atmospheric pressure due to likely higher nitrogen concentration (Goldblatt et al., 2009a) may have compensated for the weaker solar flux by raising surface temperature. However, recent models allowing for these effects still fail to resolve the paradox (Goldblatt and Zahnle, 2011; Goldblatt et al., 2009a). Mineralogical constraints implying very low Archean CO_2 concentration may suffer from lack of thermodynamic equilibrium between the assemblage and the atmosphere and are at best uncertain (Dauphas and Kasting, 2011; Reinhard and Planavsky, 2011).

Glacial evidence is found sporadically throughout Earth history (see fig 1.1.1), indicating periods of low global temperature. Absence of glacial strata is assumed to represent warm global temperature. Several glacial periods appear to have been long lasting with ice sheets extending to, or very close to the equator. These events occur in the Paleoproterozoic (Papineau, 2010; Evans et al., 1997; Bekker et al., 2001) and Neoproterozoic (Hoffman et al., 1998; Arnaud et al., 2011). Other large but less extensive glaciations occur in the Permo-Carboniferous (330-260Ma) and the Cenozoic (30-0Ma) (Crowley, 1998).

The concentration of atmospheric oxygen has changed by many orders of magnitude over Earth history. Recent reviews of the geological constraints roughly bracket oxygen concentration below 10^{-5}PAL before 2.4 Ga, between 0.01-0.2 PAL during the period 2.4-0.58 Ga, and above $0.6 - 0.8$PAL for 400Ma-present (Papineau et al., 2007; Pavlov and Kasting, 2002; Kump,

2008; Canfield, 2005; Jones and Chaloner, 1991; Belcher and McElwain, 2008). This oxygen window is shown in figure 1.1.1. Note the apparent correlation between increasing oxygen concentration and deep glaciation.

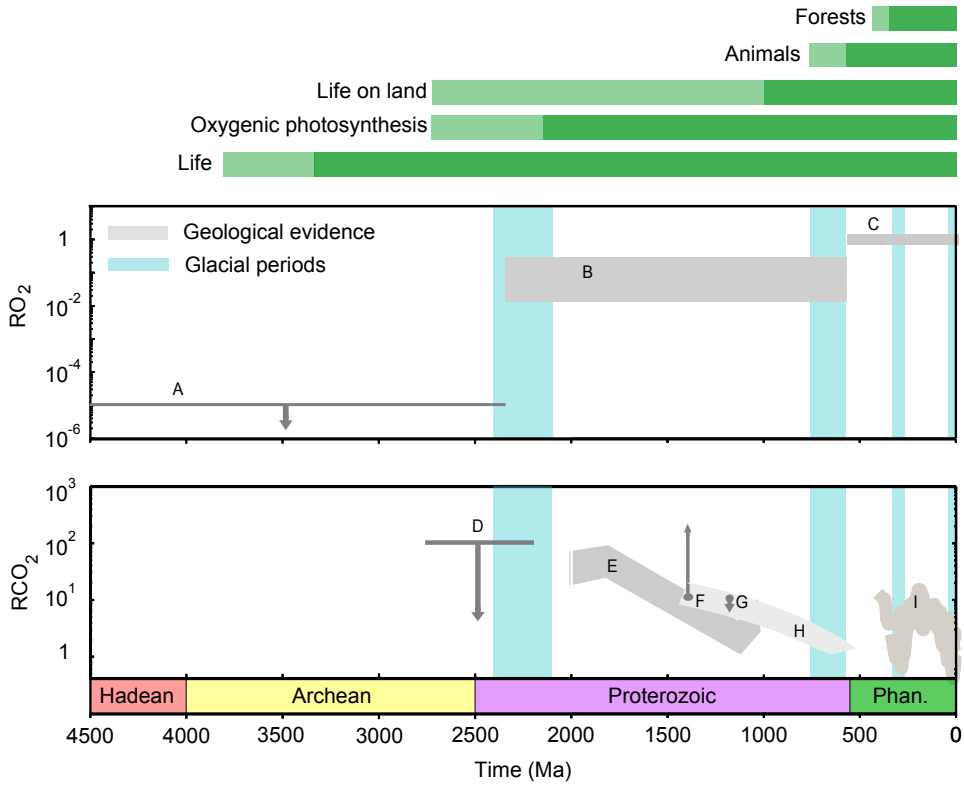

Figure 1.1.1: Compilation of evidence for environmental and biological changes over Earth history. Grey shaded areas show proxy constraints on atmospheric O_2 and CO_2, plotted relative to their present day concentrations. Constraints for oxygen (A,B,C) show the three distinct windows described in the text, and follow the review of Kump (2008). Proxy data for CO_2 show estimates from paleosol data (D) (Rye et al., 1995), (E) (Sheldon, 2006), carbon isotope modelling (H) (Kah and Bartley, 2004) and a compilation of Phanerozoic indicators from paleosols, plankton and stomatal density (I) (Royer et al., 2004). Grey circles with arrows show upper and lower bound estimates from composition of fossil acritarchs (F) (Kaufman and Xiao, 2003) and cyanobacteria (G) (Kah and Riding, 2007). Blue shaded areas represent times of substantial glaciation (see text). Dark green lines show the earliest agreed evidence for evolutionary advancements, with the light green areas showing the uncertainty, as described in the text. Original in colour.

1.1.3 Life and Evolution

It is thought that the Earth could have been habitable by 10-20 Myrs after the Moon-forming impact (Zahnle et al., 2007). Isotopically light carbon[1] found in 3.8Ga sediment sequences (Mojzsis et al., 1996) is the earliest indicator of the presence of life, as no abiotic processes are known to cause such high degrees of carbon isotope fractionation. Sedimentary structures called stromatolites, which today are produced by microorganisms, are found in increasing numbers beginning at 3.5Ga (Schopf et al., 2007; Hofmann, 2000; Schopf, 2006) although to prove beyond doubt that they are organic in nature is currently not possible due to lack of an associated fossilised microbiota (Grotzinger and Knoll, 1999).

Hard evidence for life comes in the form of microfossils, which are found beginning 3.32Ga (Walsh and Lowe, 1985; Walsh, 1992; Knoll and Barghoorn, 1977). A combination of analytical techniques are used to verify the biological morphology and carbonaceous chemistry of proposed fossils at the micron-scale (House et al., 2000; Boyce et al., 2001; Kudryavtsev et al., 2001; Schopf, 2006), following a rigorous criteria for establishment of biogenicity (Schopf, 2004).

The increasing complexity of life over time can be established from the fossil record, which displays numerous remarkable evolutionary transitions (Szathmry and Maynard Smith, 1995). Chemical composition of carbonaceous matter dated to 3.416 Ga indicate the presence of photosynthetic anoxic microbes (Tice and Lowe, 2004, 2006). Fossils resembling cyanobacteria are found beginning 2.15Ga (Hofmann, 1976), indicating oxygenic photosynthesis was present by this time. Fossilised lipids in rocks dated to 2.7Ga are characteristic of cyanobacteria (Brocks et al., 1999; Summons et al., 1999), however these biomarkers are now known to be non-primary (Rasmussen et al., 2008). It is currently uncertain whether the evolution of oxygenic photosynthesis occurred sometime before, or coincidentally with the 2.4Ga

[1]Organic matter is depleted in the heavy ^{13}C isotope due to biological preference for the lighter ^{12}C isotope (Mook, 1986). The $\delta^{13}C$ record shows the relative abundance of the heavy isotope in marine carbonates compared to the standard Pee Dee Belemnite ($\delta^{13}C_{PDB}$=0), and has been traditionally taken as a rough measure of the fraction of total carbon that is buried organically. Bacterial sulphate reduction similarly produces H_2S in which the sulphur is isotopically light. The standard here is the Canyon Diablo Troilite ($\delta^{34}S_{CDT}$=0).

great oxygenation event. Eukaryotic cells, which unlike earlier prokaryotes contain complex internal structures (organelles) likely evolved around 2 Ga (Lenton and Watson, 2011), with the first indisputably eukaryotic fossils found at 1.2Ga (Butterfield, 2000). Elemental ratios and isotopic composition of 2.6-2.7Ga organic matter suggest that terrestrial biomass may have been present at this point (Watanabe et al., 2000), the first evidence for microbial structures on land is found around 1.2-1 Ga (Prave, 2002) and protein sequence analysis suggests fungi had evolved by this time (Heckman et al., 2001). Fossil land plant fragments appear at 460 Ma (Wellman et al., 2003) and forest ecosystems with rooted trees were present by the Devonian period (415-360Ma) (Retallack, 1997). Animals may have evolved as early as 760Ma (Brain et al., 2012), and oxygen-breathing land animals are found by 428 Ma: the millipede *Pneumodesmus Newmani* possesses breathing holes called spiracles that are utilised by modern insects (Wilson and Anderson, 2004). The first recorded mammals are early Cretaceous (145-66 Ma) monotreme fossils (Archer et al., 1985). Rising temperature due to stellar evolution is expected to limit the future of the complex biosphere on Earth to $\sim$1 Gyr (Lenton and Bloh, 2001).

1.2 Biogeochemical modelling

The oceans, atmosphere and lithosphere are in constant flux, however their compositions appear to have remained relatively stable over millions of years. This is attributed to the operation of negative feedback loops in global elemental cycles, which rely on a combination of biological, geophysical and chemical processes. Stabilisation of environmental conditions in the ranges suitable for life was first discussed as part of the Gaia hypothesis (Lovelock, 1972; Margulis and Lovelock, 1974; Lovelock, 1979), which proposed that tight coupling between life and its environment constitutes a global cybernetic system, and should tend towards homoeostasis. A hypothetical model demonstrating this idea, Daisyworld (Watson and Lovelock, 1983) showed that on a planet that was gradually heating up due to increasing solar flux, competition between two types of organism that had opposite effects on climate (in this case, black and white daisies that respectively warmed or cooled the planet) could lead to regulation of planetary temperature at the level

most suitable for the survivability of the biosphere as a whole.

The level of control exerted by the biosphere, if any, is both contraversial and uncertain, however, numerous stabilising mechanisms have been identified in the Earth system, and modelling studies incorporating these have led to an improved understanding of biogeochemical cycles, as well as providing causal relationships for observed paleoclimatic changes. An early attempt to model an existing Earth system feedback loop was the 'WHAK' model, named after the authors Walker, Hays and Kasting (Walker et al., 1981). This work highlighted that the rate of removal of carbon dioxide from the atmosphere via continental weathering and deposition in sediments is dependent on global temperature. Rising temperature should boost the kinetics of weathering reactions and increase the rate of continental runoff, leading to increased CO_2 removal, which would reduce atmospheric greenhouse gas concentration and therefore act to nullify the original temperature rise.

Further models added this feedback loop (Berner et al., 1983; Berner and Barron, 1984), and others (Lenton, 2000; Lasaga and Ohmoto, 2002) to representations of geochemical cycling in order to arrive at predictions for the composition of ancient atmospheres. Currently, feedback-based geochemical box models are used to predict the evolution of climate over the Phanerozoic Eon (Berner, 2006a; Bergman et al., 2004; Arvidson et al., 2006), and allow multiple predictions including concentration of oxygen, ocean sulphate and nutrient levels in addition to carbon dioxide and temperature. For shorter term analysis (e.g. millennial timescale), intermediate complexity Earth system models (e.g. Lenton et al. (2006); Ridgwell and Hargreaves (2007)) allow for a 3D spatial approach and explicit representation of sedimentary processes and ocean circulation. General Circulation Models (e.g. Marotzke et al. (1999)) add further complexity and reduce the timscale of operation accordingly due to computational constraints. Intermediate complexity models or GCMs are well suited to analysing future climate trends, and to compare possible future events to those recorded in the geologic record (e.g. Ridgwell and Schmidt (2010)). Many feedback mechanisms do however remain poorly understood, for example the relation between ocean gas emissions and cloud formation (Charlson et al., 1987).

1.3 This work

The models considered and developed in this thesis are applied over long timescales (10^6-10^9 years) and consist of simplified systems of differential equations that represent global biological, chemical and geophysical processes. The aim is to construct a robust model framework based on current box models for the Phanerozoic, and to apply this model to the study of Proterozoic climate. Simple carbon cycle models have previously been applied to the Proterozoic period (e.g. Sleep and Zahnle (2001); Hayes and Waldbauer (2006)) but climate predictions are limited to temperature and CO_2.

In Chapter 2 the current Phanerozoic modelling techniques are reviewed. Code is obtained for the GEOCARB and COPSE models and the controlling processes in these models are assessed.

Chapter 3 focusses on the development of a model framework based on GEOCARB and COPSE. The new 'Minimal Model' is validated against the previous works and shows good agreement for the Phanerozoic. The timeframe of the Minimal Model is extended to the Neoproterozoic, predicted oxygen concentration and causes for the deep glaciations at this time are then investigated.

In Chapter 4, the Minimal Model is modified to allow for snowball Earth (Hoffman et al., 1998) type glaciations by introduction of a ice-albedo positive feedback. The system is then used to test the effect of geological weathering limitation on the time taken to recover from a post-snowball CO_2 crisis. The main body work from this chapter has been published (Mills et al., 2011) and is reproduced here with some extension and further discussion.

In Chapter 5, new fluxes and boxes are added to the model framework to represent long term cycling between the surface system and the mantle. The extended model is used to investigate the effect of changing carbon removal pathways (e.g. Caldeira (1995)) on ocean nutrient levels and oxygen concentration over the last 2Ga. The work in this chapter, including some work from chapter 3, is currently being prepared for submission.

2 Phanerozoic carbon cycle modelling

2.1 Introduction

In this chapter I review the literature on the modelling of the long term carbon cycle over the Phanerozoic eon (542-0Ma). Various models have attempted to reconstruct the flow of carbon through the atmosphere, oceans and sediments over this period, and in doing so have provided key estimates for atmospheric CO_2, temperature and O_2 concentration. Here I focus on two popular Phanerozoic models, GEOCARBSULF (Berner, 2006a) and COPSE (Bergman et al., 2004), which are commonly used as benchmarks from which to test theories on paleoatmospheric conditions (e.g. Belcher et al. (2010)).

Whilst there are many apparent similarities between the two models, for some periods of Earth history they produce significantly different results. In this chapter I attempt to trace the root of these differences and assess the key processes controlling model predictions. Estimates for Phanerozoic CO_2 and O_2 are cross-examined and compared to proxy data. The goal of this analysis is to define a reduced set of critical processes and parameters that can be used to construct a new, simpler model. It is hoped that the new model can reproduce the broader scale predictions of the established work, but with significant improvements in flexibility, robustness and mathematical simplicity that will allow application to Precambrian climate. The model runs in this section are performed using original code for the 2004 COPSE model (Bergman et al., 2004) and for the 2009 'GEOCARBSULFvolc' model (Berner, 2009), obtained directly from the respective authors.

2.2 The GEOCARB model

The first GEOCARB model (Berner, 1991) was a dramatic step forwards in understanding the link between the carbon cycle and global climate over geological time. Following only the cycle of carbon allowed for substantial simplification of a previous model of the carbonate-silicate cycle, which had included explicit representation of the calcium and magnesium cycles (Berner et al., 1983). This step led to improved computational efficiency and allowed the first reconstruction of climate for the whole Phanerozoic.

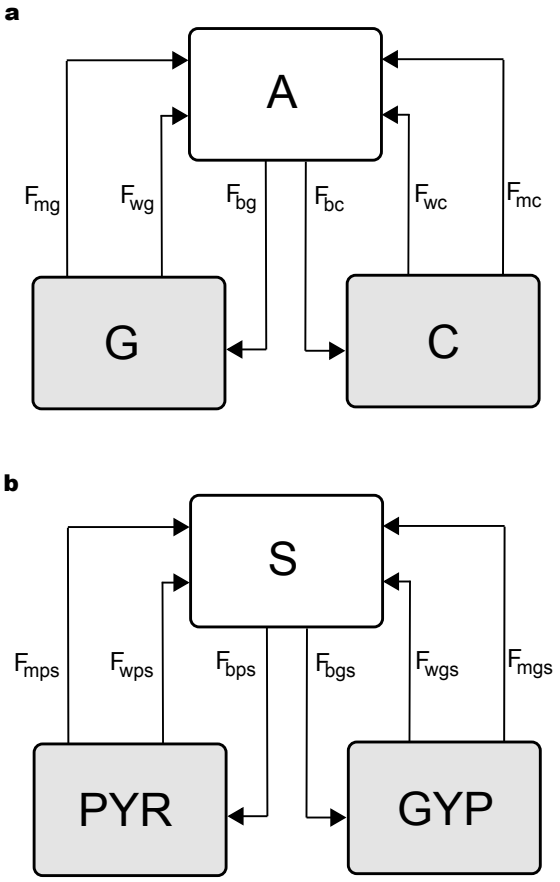

Figure 2.2.1: Long term carbon and sulphur cycle schematic, as used in GEOCARB and COPSE models. Clear boxes denote the combined atmosphere/ocean reservoirs, grey boxes represent crustal reservoirs. Flux subscripts 'b', 'w' and 'm' refer to burial, weathering and metamorphic/degassing respectively. **a,** Carbon cycle, G: Organic (reduced) carbon, C: Carbonate (oxidised) carbon, A, Atmosphere and ocean carbon. **b,** Sulphur cycle, PYR: Pyrite (reduced) sulphur, GYP: Gypsum (oxidised) sulphur, S: Ocean sulphate.

The original GEOCARB model uses a 3-box system to simulate the transfer of carbon between the hydrosphere and crust, which is shown in figure 2.2.1 **a**. Carbon is assumed to exist as CO_2 in the combined atmosphere and ocean (which is modelled as a single box), and as either oxidised carbonates or reduced organic matter in the crust. Carbon is transferred between the boxes via burial, weathering and degassing. Over long timescales ($> 10^6$ yrs) other elements of the global carbon cycle can be considered to be at steady state, allowing for an estimation of the carbon content of the atmosphere and

ocean over the Phanerozoic based on knowledge of the fluxes between these boxes. The GEOCARB model has been extended many times (Berner, 1994; Berner and Kothavala, 2001; Berner, 2006a,b, 2009), and the more recent models include a similar 3-box treatment for the cycling of sulphur species, shown in figure 2.2.1 **b**. Sulphur is assumed to exist as oxidised sulphate in the atmosphere/ocean and as gypsum (oxidised) sulphur and pyrite (reduced) sulphur in the crust. In the later versions of GEOCARB the crustal boxes are each split into 'young' and 'ancient' partitions to explore isotope fractionation effects, but this does not affect the total fluxes between hydrosphere and crust. Further additions include a routine for calculating oxygen concentration, and more complex treatment of volcanism.

The series of GEOCARB models do not contain explicit biological processes, and the biologically-influenced burial of organic carbon and pyrite sulphur are estimated based on the isotopic ratios δ^{13}C and δ^{34}S (see introduction), which are imposed as an external forcing.

2.3 The COPSE model

COPSE uses the same box and flux scheme as GEOCARB for the carbon and sulphur cycles, without assuming a partition between young and ancient rock. The scheme is combined with a previously designed box model for ocean productivity and oxygen (Lenton and Watson, 2000a,b). This adds two boxes to the GEOCARB system which represent the major limiting nutrients phosphate and nitrate, allowing calculation of burial rates for reduced carbon and sulphur via the modelled nutrient concentrations. Calculating organic burial in this manner means that COPSE does not require the isotope record to be used as a model forcing, and allows the model to instead produce predictions for stable isotope fractionation, however additional forcings are required for the nutrient system to function. Figure 2.3.2 shows the fluxes controlling nutrient concentrations, which in turn drive productivity and burial of organic species.

A popular and more complex model, MAGic (Arvidson et al., 2006), is not discussed in length here. My aim in this thesis is to understand the factors controlling atmospheric and ocean composition over long periods of Earth history in the simplest terms, I therefore do not analyse the MAGic

system in detail, as it can be effectively reduced to the simpler COPSE system whilst maintaining the general results. In MAGic, the rate of organic burial is estimated from ecosystem productivity, which is based on delivery of nutrients via weathering. This treatment is similar to the COPSE model, and the resulting predictions for Phanerozoic climate are very similar (see Arvidson et al. (2006)).

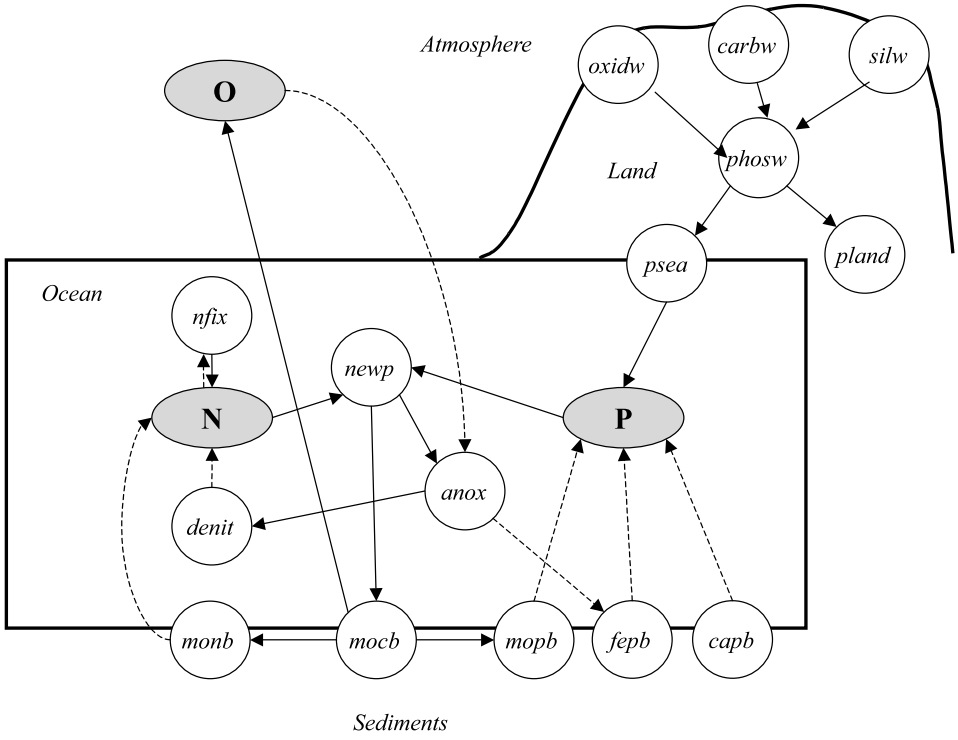

Figure 2.3.2: Feedback-based nutrient system for COPSE model O: Oxygen, N: Nitrate, P: Phosphate. Fluxes ending with 'b' denote burial, 'w' denotes weathering. *psea* and *pland* represent the proportion of weathered phosphate delivered to the land biosphere and the ocean. *newp* is new production, $nfix$ and *denit* represent nitrogen fixation and denitrification fluxes and *anox* represents the ocean anoxic fraction. Here arrows do not represent fluxes but show the ability of one variable to alter another. Solid lines show a positive relationship, dashed lines show an inverse relationship. See Bergman et al. (2004) for a full description.

2.4 Flux calculation and forcing sets

For both models, the fluxes between boxes are calculated using knowledge of their present day magnitude and a variety of proposed scaling relationships

to both internal model variables and external forcing functions. As noted previously, one key difference between GEOCARB and COPSE is in the calculation of the organic burial fluxes. Another important difference is in the model forcing sets - the GEOCARB model uses many more external forcings than COPSE. For both models, the magnitude of the external forcing functions (i.e. F) is defined relative to present day, with typical magnitude $0.5 < F < 1.5$. The full forcing sets are shown in figure 2.4.3, and described below. Both models are also subject to an increase in solar luminosity over the Phanerozoic (not shown), which affects the global temperature (Caldeira and Kasting, 1992).

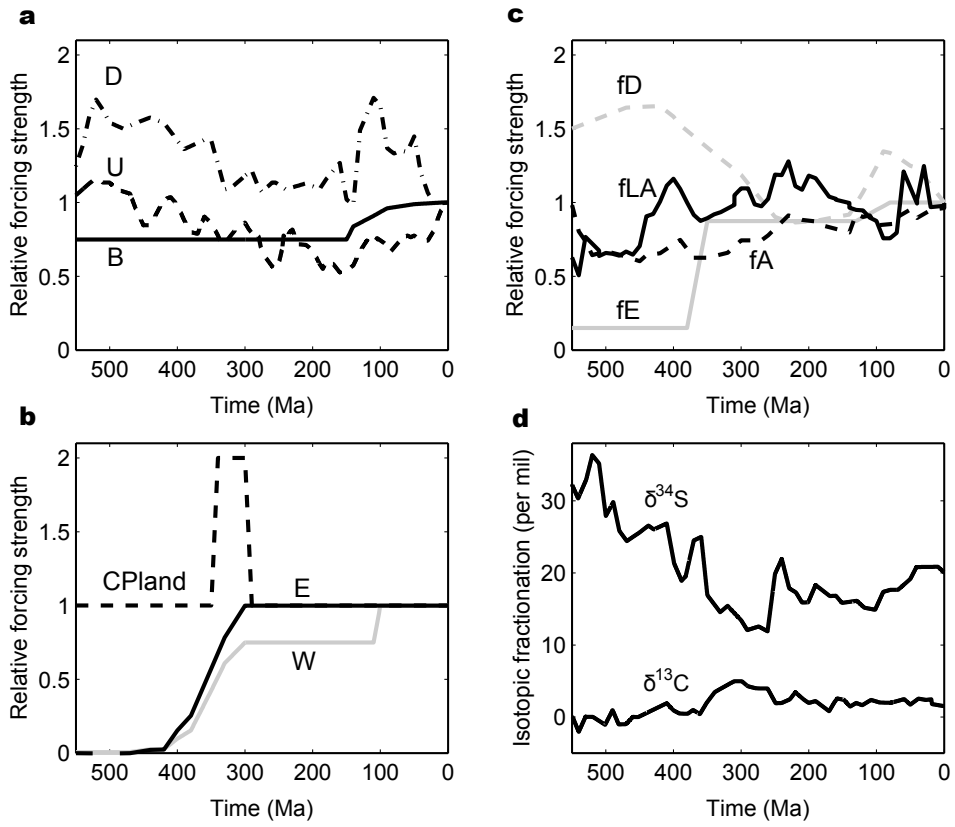

Figure 2.4.3: Model forcings a, Forcings common to both models. U: Uplift, D: Volcanic degassing, B: Shallow/deep carbonate burial. **b,** Additional forcings for COPSE model. CPland: Carbon-to-phosphorus burial ratio on land, E: Land plant evolution, W: Land plant weathering enhancement. **c,** Additional forcings for the GEOCARB model. fD: Relative runoff rate, fLA: Carbonate land area, fA: Land area, fE: Land plant evolution. **d,** Isotopic forcings for GEOCARB model.

2.4.1 Forcings common to both models (figure 2.4.3a)

U: uplift rate

The rate of continental uplift over the Phanerozoic has been estimated from a strontium isotope mass balance model (Berner, 1994). This model reconstructs changes in seawater $^{87}Sr/^{86}Sr$ in the absence of Sr input from terrestrial weathering, which is then compared to data to estimate the weathering contribution. The results agree well with data for terriginous sediment abundance (Ronov, 1993). In both models, the uplift/erosion parameter affects the rate of continental weathering via supply of material.

D: degassing rate

The GEOCARB and COPSE models use a sea level inversion method (Gaffin, 1987) to calculate the sea floor spreading rate, which is used to estimate global degassing rates (Franck and Bounama, 1997; Lasaga et al., 1985). The degassing forcing controls the rate of release of buried carbon and sulphur into the atmosphere via recycling at subduction zones.

B: burial depth of marine carbonates

Both models include a forcing affecting carbonate degassing, attributed to the evolution of calcareous plankton at ∼150Ma, which are deposited in deep water. Their evolution is thought to have increased the amount of carbonate entering subduction zones and hence undergoing thermal decomposition (Volk, 1989).

2.4.2 Additional forcings for COPSE (figure 2.4.3b)

W: weathering rate enhancement due to biosphere changes

The colonisation of the land surface by vascular plants by ∼350Ma is thought to have dramatically enhanced continental weathering rates (Stewart and Rothwell, 1983). Roots exudate organic acids, amplifying rates of chemical weathering, as well as physically breaking up rock. Enhancement of weathering by vascular plants is seen in field studies but results vary greatly, therefore the global effect of vascular plant evolution remains uncertain (Cawley et al., 1969; Berner, 1998). Further weathering enhancement is thought to have occurred due to the evolution of angiosperm plants at ∼100Ma, due to their higher rubisco specificity factor (the preference of the enzyme for CO_2

over O_2 (Igamberdiev and Lea, 2006)), and less efficient recycling of nutrients (Knoll and James, 1987). The W forcing in COPSE acts to enhance terrestrial weathering rates as the biosphere evolves.

E: evolution of biological feedbacks on land

The effect of the terrestrial biosphere on geochemical cycling is dependent on various local factors such as temperature, CO_2 concentration and O_2 concentration, which affect productivity both directly (Caldeira and Kasting, 1992; Volk, 1987) and via the rate of biosphere burning due to fires (Wildman et al., 2004; Watson, 1978). The E forcing in COPSE acts to 'switch on' these feedbacks once the land biosphere has evolved.

CPland: carbon-to-phosphorous burial rate on land

The burial ratio of carbon to phosphorus on land is doubled in the Permo-Carboniferous in the COPSE model. This represents the expectation that extensive burial of organics occurred in coal swamps during this time (Berner and Canfield, 1989; Kump, 1993).

2.4.3 Additional forcings for GEOCARB (figure 2.4.3c,d)

The most recent GEOCARBSULF model uses a large forcing set, adding the forcings shown in 2.4.3**c** and 2.4.3**d** to the forcings in 2.4.3**a**. The forcing set has grown substantially since the first GEOCARB model, as more processes have been identified as being important to the geological carbon cycle.

fE: weathering rate enhancement due to biosphere changes

GEOCARB was the first model to include the effects of plant evolution on the carbon and sulphur cycles (Berner, 1991). The fE forcing in GEOCARB expresses a 2-step increase over the Phanerozoic, from which the COPSE forcing W is derived. There is no equivalent to the COPSE 'E' forcing in GEOCARB, as the model does not have an explicit representation of biospheric feedbacks.

fD: runoff rate

The assumed changes to continental runoff due to paleogeography are derived by calculating runoff rates for 10 degree 'latitude slices' in a reconstruction of Phanerozoic continental drift (Tardy et al., 1989; Berner, 1990). The runoff forcing is assumed to influence the terrestrial weathering rates by increasing

rate of flow of material through weathering zones.

fA: total land area
The total land area is also derived from paleogeographic reconstructions (Barron et al., 1980; Ronov, 1976), and influences bulk weathering rates by changing the area exposed to weathering.

fLA: carbonate land area
The relative land area that is underlain by carbonate rocks. Derived from the relative land area forcing, fA, and the paleogeographic maps of Bluth and Kump (1991). This forcing affects the weathering of carbonates.

δ^{13}C and δ^{34}S : productivity forcings Using data for the fractionation of marine carbonates as a proxy for paleoatmospheric fractionation allows estimation of the rates of organic carbon burial by the biosphere, assuming that the total carbon burial and the fractionation of the crustal reservoirs is known. This isotopic mass balance technique was explored by Garrels and Lerman (1984) and Berner (1987) before being incorporated into the first GEOCARB model (Berner, 1991). The same technique is used in later models to estimate the rate of organic pyrite sulphur burial, based on the isotopic ratio δ^{34}S. Isotope mass balance techniques will be explored further in section 2.7.3.

2.4.4 Summary

The GEOCARB and COPSE models share a simple set of forcings: global uplift and degassing rates, and the changes brought about by the evolution of land plants and calcareous plankton. GEOCARB adds further abiotic forcings, and importantly, adds a forcing for the productivity of the biosphere, which is used to prescribe the rates of organic burial. The COPSE model assumes that burial rate of organic carbon and pyrite is governed by the rate of marine new production, which itself is assumed to depend on ocean nutrient concentration. Additional assumptions are therefore required to predict the rate of organic carbon burial via the nutrient model: a complex dependency of the mass of the terrestrial biosphere on atmospheric conditions, and the additional biotic forcings E and CPland, shown in figure 2.4.3**b**.

2.5 Negative feedback on temperature and CO_2

The atmospheric and oceanic reservoir of carbon is around 10^6 times larger than the yearly fluxes into and out of it, while for oxygen this factor is 10^7. Therefore an imbalance in fluxes may deplete either reservoir on a timescale far shorter than the duration of the Phanerozoic eon ($\sim 5 \times 10^8$ years). Stability (or homeostasis) in the carbon cycle is achieved via naturally occurring negative feedback mechanisms. A key process for model stability is the temperature-dependence of the silicate weathering process (Walker et al., 1981). Weathering of silicates, followed by transfer to the ocean and eventual burial in sediments results in a net transfer of CO_2 from the hydrosphere to the crust. Temperature influences the rate of chemical reaction and therefore an increase in temperature results in an increased removal of CO_2 from the surface system, lowering the radiative forcing from this gas and therefore lowering temperature. This mechanism is thought to have been extremely important throughout Earth history to stabilise CO_2 at levels that permit the removal flux by weathering to equal the input flux from degassing, and was the central focus of carbon cycle models preceding GEOCARB (e.g. Berner et al. (1983). The equation adopted by GEOCARB and COPSE is based on the field work of Berner (1994), combining a term for the rate of chemical dissolution with a term for the rate of runoff:

$$f_B(T) = e^{0.09(T-T_0)} \cdot (1 + 0.038(T - T_0))^{0.65} \tag{2.5.1}$$

Where f_B is the effect of temperature on the global rate of silicate weathering, T is global average surface temperature and $T_0 = 288K$ is the present day average surface temperature. The full equation for the silicate weathering flux also includes dependence on model forcings, as well as effects of CO_2 fertilization of vascular plants (Berner, 1994).

2.6 Phanerozoic CO_2 predictions

2.6.1 Summary of predictions

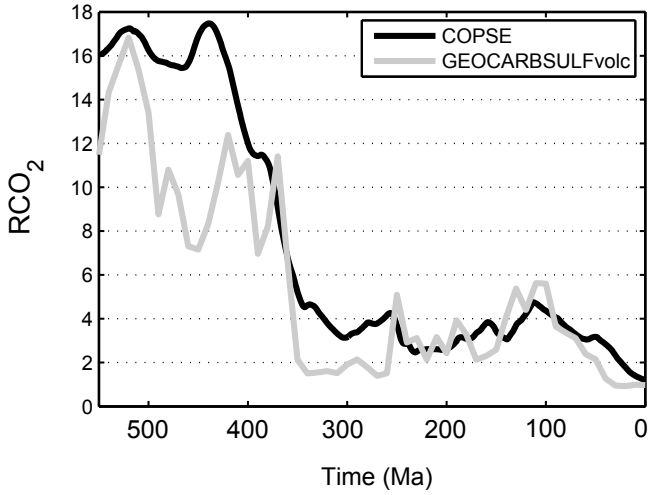

Figure 2.6.4: Phanerozoic CO_2 predictions. RCO_2 denotes atmospheric carbon dioxide concentration relative to the present day (pre-industrial) concentration. The COPSE model (Bergman et al., 2004) is shown in black, the GEOCARBSULFvolc model (Berner, 2009) is shown in grey.

Figure 2.6.4 shows baseline Phanerozoic CO_2 predictions for the COPSE model and the GEOCARBSULFvolc model (GEOCARB hereafter). The overall pattern predicted by both models is of elevated (10-20 times present day) CO_2 from 550-350Ma, dropping to around 1-5 times present day concentration for the period 350-0Ma. From this plot we can highlight three distinct features:

1) Agreement between modelled carbon dioxide concentrations is very strong from the Mesozoic onwards (250-0Ma).

2) Model CO_2 predictions from 550-250Ma follow a similar overall trajectory, but GEOCARB predicts lower concentrations than COPSE for this time period.

3) The COPSE CO_2 path is smoother than the GEOCARB prediction, with less scatter.

To understand the critical processes in these models it is important to provide a reason for each of these observations.

2.6.2 Calculation for carbon dioxide concentration

Both models estimate the change in the atmosphere and ocean carbon reservoir using the flux calculation shown in equation 2.6.1, which sums the sources and sinks of the A resevoir, as shown in figure 2.2.1**a**.

$$\frac{dA}{dt} = F_{wg} + F_{mg} + F_{wc} + F_{mc} - F_{bg} - F_{bc} \tag{2.6.1}$$

Here, subscript prefixes 'w', 'm' and 'b' refer to weathering, metamorphic/degassing and burial. Subscript suffixes 'g' and 'c' refer to organic and carbonate carbon (see figure 2.2.1). Burial of both reduced and oxidised carbon constitutes a sink for atmosphere and ocean CO_2, with the sources being the degassing and weathering of both of the crustal carbon reservoirs. All of these fluxes are affected by changes in model forcings and internal variables such as global average temperature.

2.6.3 Serial modification of model forcing sets

In order to explain the observed differences in output, the models are now compared under different forcing groups. The results are shown in figure 2.6.5. The assumed enhancement of terrestrial weathering due to the evolution of vascular plants differs between models. COPSE uses a 7-fold increase, as used in the first GEOCARB model (Berner, 1991), whilst GEOCARBSULFvolc uses a more conservative 4-fold increase (Berner and Kothavala, 2001). In figure 2.6.5**a**, the GEOCARB model is altered to increase the enhancement factor to match that used in COPSE. The modification does not alter results for 0-350Ma, but brings the model predictions closer to COPSE for 350-550Ma. Note that allowing a larger enhancement of the silicate weathering sink at 350Ma does not alter CO_2 predictions for 350-0Ma, as might be expected, but results in a higher CO_2 prediction for 550-350Ma. This is because model fluxes are inferred from the present day Earth system, thus the assumption of a '7-fold increase' in weathering efficiency after 350Ma is actually modelled as a 7-fold decrease in efficiency before 350Ma.

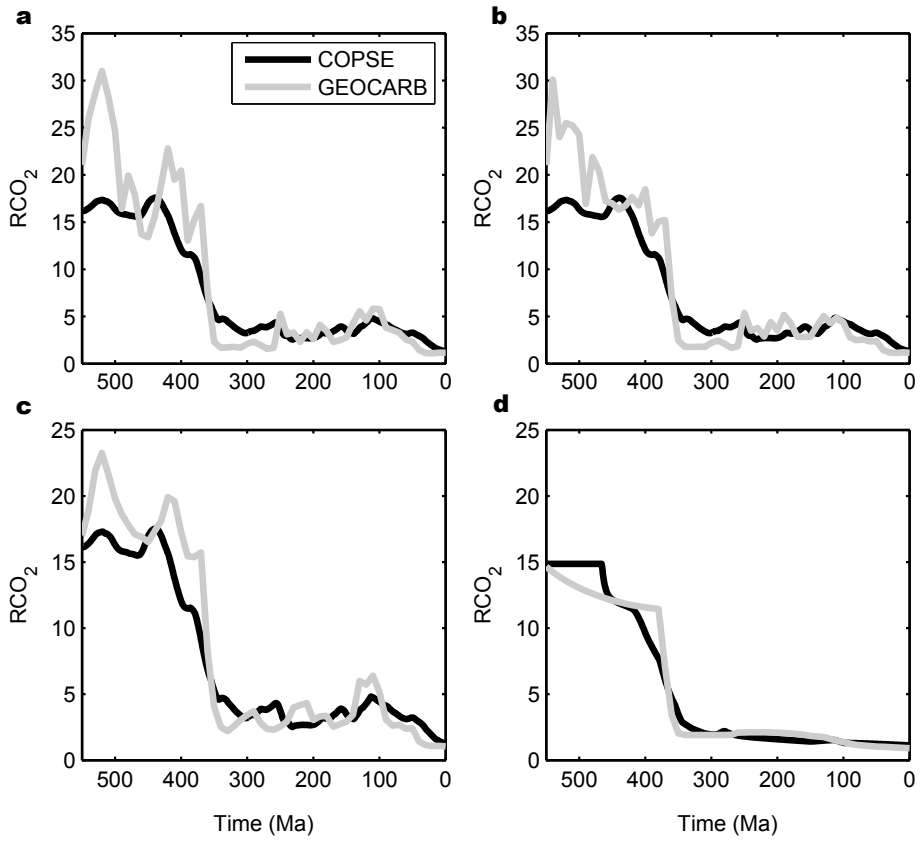

Figure 2.6.5: Serial modification of COPSE and GEOCARB models. COPSE model (Bergman et al., 2004) shown in black and GEOCARB model (Berner, 2009) shown in grey. **a,** GEOCARB is adjusted so that both models use the same value for vascular plant weathering enhancement (7 fold). **b,** GEOCARB is further adjusted to include only the uplift and degassing forcings, as used in COPSE. **c,** as **b** with exclusion of isotope forcings from GEOCARB. **d,** as **c** with exclusion of uplift and degassing forcings from both models. Note the change to the y-axis scale in panels **c**,**c**

In figure 2.6.5 **b**, GEOCARB is simplified by removing all abiotic forcings except for uplift and degassing (i.e. everything shown in figure 2.4.3**c**), thereby limiting the abiotic forcings to the same set used in COPSE. Interestingly, this modification does not significantly impact the model predictions for CO_2. In figure 2.6.5 **c**, the productivity forcings derived from the isotope record are also removed from GEOCARB, leaving uplift, degassing and evolutionary forcings only. The forcings for GEOCARB now mimic those in COPSE (with the exception that no biological forcings are now present).

This results in almost identical predictions for CO_2. Finally, in figure 2.6.5 **d** the uplift, degassing, and carbonate burial depth forcings are removed from both models. The sole forcing is now the enhancement of weathering due to evolution of the land biota. Note that the qualitative shape of CO_2 predictions is preserved in both models. Differences remain due to the implementation of various shared parameters such as temperature functions and the land plant evolution forcing.

2.6.4 Perturbation experiments

The CO_2 predictions from the GEOCARB model show a more pronounced response to forcings than those from COPSE, this can be seen most clearly in figure 2.6.5**c**, where the identical forcing sets result in similar CO_2 variation, only the magnitude of variation is generally smaller in COPSE. COPSE appears to include stronger negative feedback on CO_2 concentration, this is likely to arise from the systematic treatment of the biosphere. For instance, in both models, an increase in CO_2 concentration increases temperature and amplifies the silicate weathering rate, leading to increased burial of atmospheric carbon until CO_2 concentration is reduced. In the COPSE model system, this increase in weathering rate also delivers more nutrient to the land and ocean biospheres, increasing the organic carbon burial rate as well as the silicate weathering rate. This should result in increased negative feedback on CO_2, and is tested below.

In figure 2.6.6, all forcings except for the solar increase (which is hard-coded in GEOCARB) are removed from both models, and a rise in either degassing or uplift rate is imposed from 200Ma-100Ma. Increased negative feedback is apparent in the COPSE model, which displays damping of imposed changes and slightly reduces their overall effect. Figure 2.6.6**c** shows the relative variation from the standard run, which is reduced in COPSE.

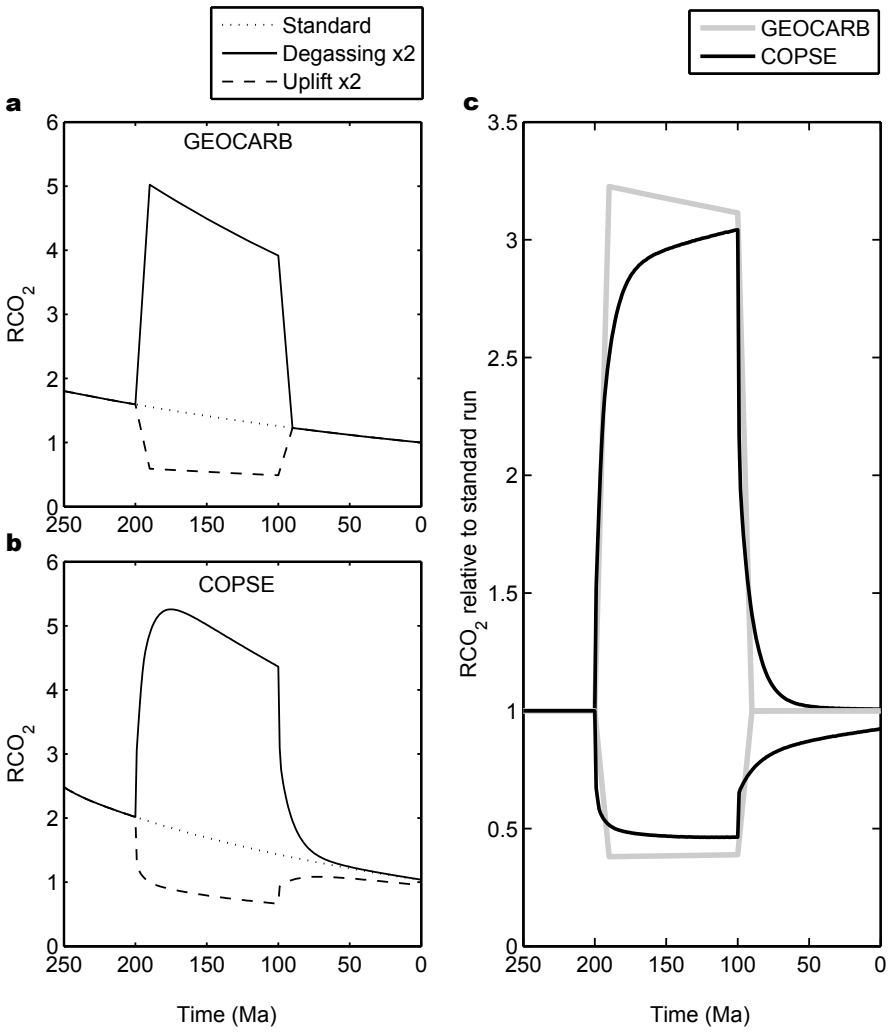

Figure 2.6.6: Effect of perturbations on GEOCARB and COPSE model. All forcings are held at present day except for solar luminosity, and a doubling of either uplift rate or degassing rate is applied for the period 200Ma-100Ma. **a,** Effects on GEOCARB system for doubling uplift or degassing. **b,** Effects on COPSE system for doubling uplift or degassing. **c,** Results for both models shown as a fraction of the unforced result.

2.6.5 Factors controlling model CO_2 predictions

It is apparent here that the COPSE and GEOCARB predictions for Phanerozoic CO_2 are controlled almost entirely by the model forcing sets. The long term pattern is a stepwise decrease in CO_2 concentration around 350Ma due to the enhancement of the silicate weathering carbon sink by the colonising

vascular plants. The dominance of this forcing is easy to see when considering the magnitude of all forcings used: the evolutionary forcing invokes a 4-7 fold enhancement, other forcings have a range of between a half and two times the present day magnitude (see fig 2.4.3). Figure 2.6.7 shows the degree of sensitivity to the assumed magnitude of weathering enhancement inferred by vascular plants. Sensitivity is extreme in both models, suggesting that CO_2 concentration closer to the present day cannot be ruled out for the early Phanerozoic based on model results alone.

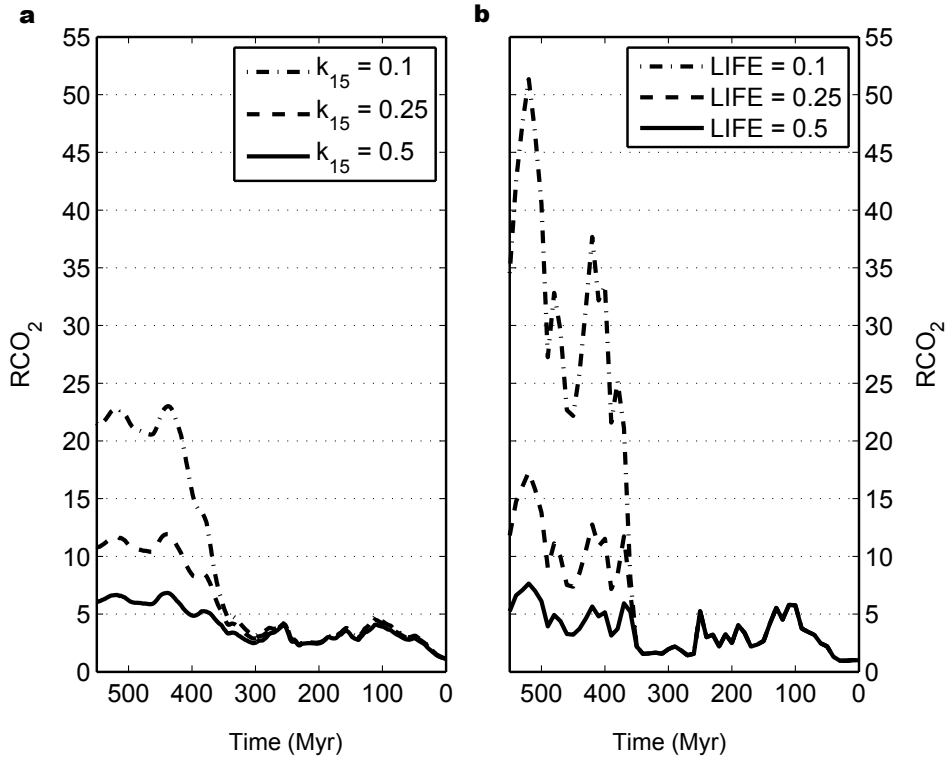

Figure 2.6.7: Effect of changing assumed vascular plant weathering enhancement factor. a, COPSE model. **b,** GEOCARB model. Variable denoting relative pre-plant weathering enhancement denoted k_{15} and LIFE respectively.

Revisiting the points of interest described in the summary (2.6.1), the reason GEOCARB predicts lower CO_2 for the period 550-350Ma is due to the use of a different value for the reduction in weathering efficiency before the evolution of vascular plants. Addressing this discrepancy brings the model predictions very close together, which explains the observed strong model agreement for the post-vascular-plant world. The rapid oscillations in CO_2

predictions from the full GEOCARB model can be seen to be a result of the isotope-productivity forcings, which are defined more densely than the other forcing functions. This effect is no longer seen once these forcings are removed (see figure 2.6.5**c**). As discussed above, the COPSE model has increased negative feedback from the linked biological model, causing CO_2 concentration to remain closer to present day, whilst GEOCARB has additional abiotic forcings which can combine to increase the degree of variation in CO_2. There are many more proposed negative feedback processes controlling long term climate, and it is possible that current models may over estimate the impact of forcings because they lack representations of sufficient negative feedbacks.

An additional smaller-scale feature of the predicted CO_2 records is a rise in concentration from 300-150Ma followed by a gradual decline to the present day. The rise is due to the evolution of calcareous plankton and associated increase of carbonate degassing, which combines with a significant peak in the degassing forcing (see fig 2.4.3) to increase atmospheric carbon dioxide concentration. Relaxation of the degassing rate and the evolution of angiosperms causes CO_2 to fall gradually from 100ma to the present day. The final finding is that the additional abiotic forcings employed in the later GEOCARB models do not significantly alter the model predictions, which has been discussed in the GEOCARB papers (e.g. Berner and Kothavala (2001)) as the model has evolved.

2.6.6 Comparison of Phanerozoic models to CO_2 proxy data

Figure 2.6.8 shows available proxy data for Phanerozoic CO_2 concentration plotted against model predictions and the glacial record, adapted from Royer et al. (2004); Crowley (1998). Proxy data shown are a combination of estimates derived from $\delta^{13}C$ of pedogenic minerals in paleosols (Cerling, 1991; Yapp and Poths, 1992), the $\delta^{13}C$ of phytoplankton (Freeman and Hayes, 1992; Pagani et al., 1999), stomatal distribution in the leaves of C3 plants (Van der Burgh et al., 1993; McElwain and Chaloner, 1995) and the $\delta^{11}B$ signature of planktonic foraminifera (Pearson and Palmer, 2000). See Royer et al. (2004) for individual proxy information. It is important to note that the sampling frequency for this data drops dramatically for more ancient pe-

riods (see 2.6.8**c**), at the time of writing no reliable proxies could be found for the period 550-450Ma.

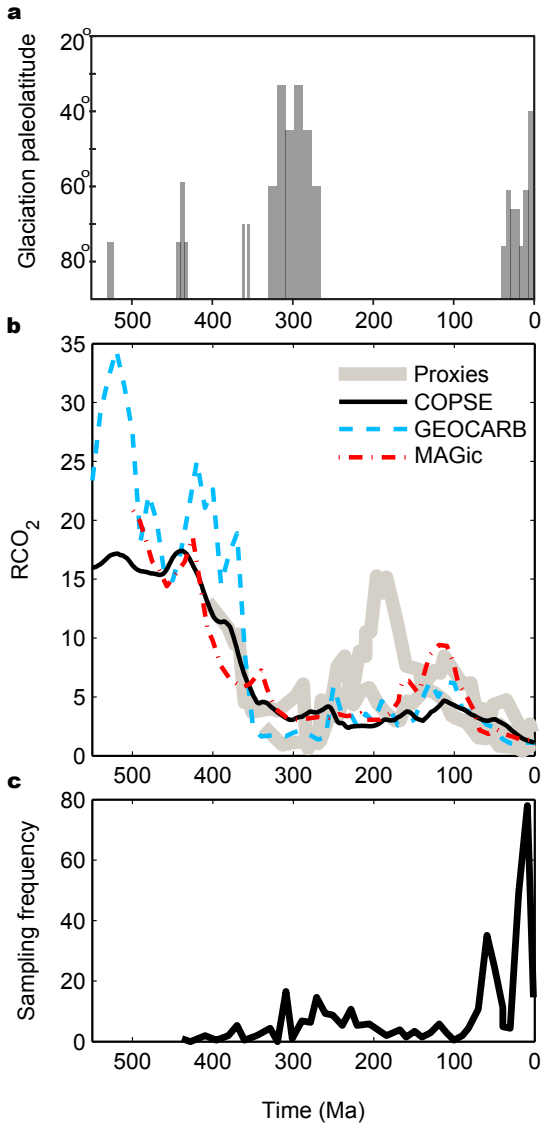

Figure 2.6.8: Model CO_2 predictions against proxy data. a, Paleolatitude of continental glaciations. **b,** Combined proxy data from paleosols, phytoplankton, stomata and boron are shown in grey. Plotted in black are model predictions from COPSE (black), GEOCARB (blue) and MAGic (Arvidson et al., 2006) (red). **c,** Sampling frequency for proxy data in **b**. Data from Royer et al. (2004). Original in colour

The models shown are GEOCARB, COPSE and MAGic (Arvidson et al., 2006). The MAGic model is considerably more complex than COPSE and GEOCARB, including explicit representation of the silicate rock reservoir and interaction with the shallow mantle. However, results for CO_2 are very close to the previous models, implying that control is exerted by the same dominant processes.

Models and proxies show good agreement for 400-0Ma, and the predicted low CO_2 in the Permo-Carboniferous and Cenozoic era fit well with the glacial data in fig 2.6.8**a**. Predicted high Mezozoic CO_2 also agrees with the lack of glacial strata from this era, however the proxies disagree somewhat with regard to the magnitude of the CO_2 increase here. The stepwise decrease in CO_2 concentration from 400-300Ma predicted by all models and hinted at by proxies does not fit as well with the glacial data. $CO_2 \geq$ 15PAL is predicted for the early Phanerozoic (and presumably time before this), simple energy balance models (Caldeira and Kasting, 1992) imply an average surface temperature of around 20°C for this carbon dioxide concentration at 500Ma. We would not expect a world this hot to be glaciated, however there is evidence for continental glaciation in the Ordovician as well as the early Cambrian. Further back, the Neoproterozoic era (1000-541Ma) contains several extremely large glacial events (Macdonald et al., 2010; Halverson et al., 2005), which are very hard to reconcile with the assumed high CO_2 due to the lack of vascular plants. A small amount of proxy data in figure 2.6.8**b** does show elevated CO_2 at ∼400Ma, but it is not known whether this is a transient rise or a step change, as currently suggested by models.

Figure 2.6.9 shows a reconstruction of paleo-temperature using the $\delta^{18}O$ values of shallow marine carbonates, reproduced from Royer et al. (2004) ($\delta^{18}O$ data from Veizer et al. (2000)). When adjusted for Ca^{2+} concentration and CO_2 concentration either from data or from the GEOCARB model, it shows fair correlation with the glacial record. The authors of the study argue that current CO_2 predictions are therefore broadly correct, and that CO_2 is responsible for the major temperature changes over the Phanerozoic. However, there is still significant uncertainty in the early Phanerozoic, and a lower model prediction for CO_2 here would improve the correlation. Estimations of CO_2 concentration from carbon and strontium isotope data (Rothman, 2001) are shown in figure 2.6.10. This data suggests $CO_2 \leq$ 5PAL for the

whole Phanerozoic, which is permissible in the models if a lower vascular plant enhancement is assumed, i.e. a doubling of weathering efficiency (see figure 2.6.7).

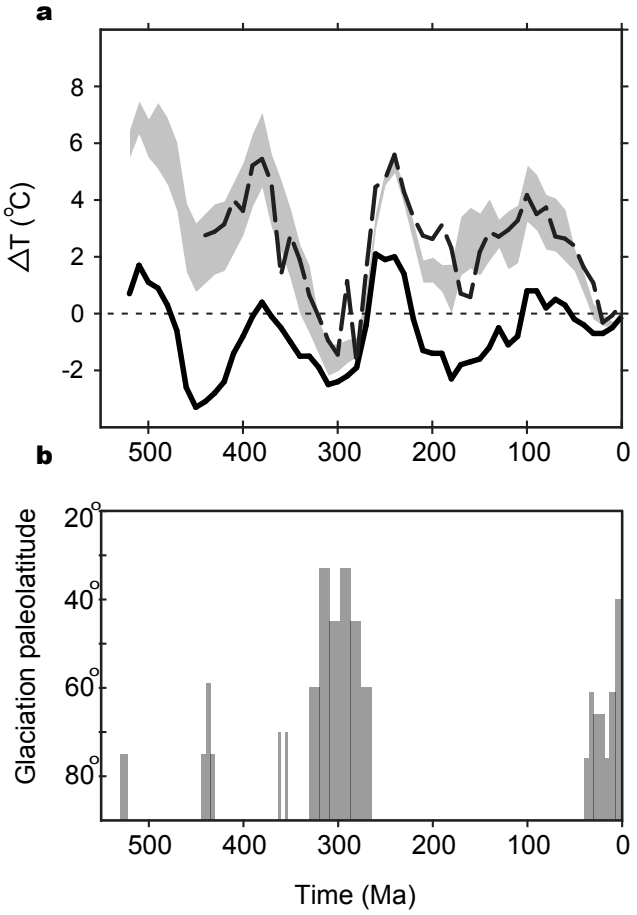

Figure 2.6.9: Temperature predictions based on δ^{18}O data. a, Calculated average surface temperature relative to present day. Solid line shows uncorrected curve (Shaviv and Veizer, 2003), dashed line shows curve corrected for seawater Ca^{2+} concentration (Horita et al., 2002) and CO_2 proxies (as shown in fig 2.6.8). Grey shaded area shows corrections for Ca^{2+} and GEOCARB model CO_2. **b,** Paleolatitude of continental glaciations (as in fig 2.6.8). Figure modified from Royer et al. (2004).

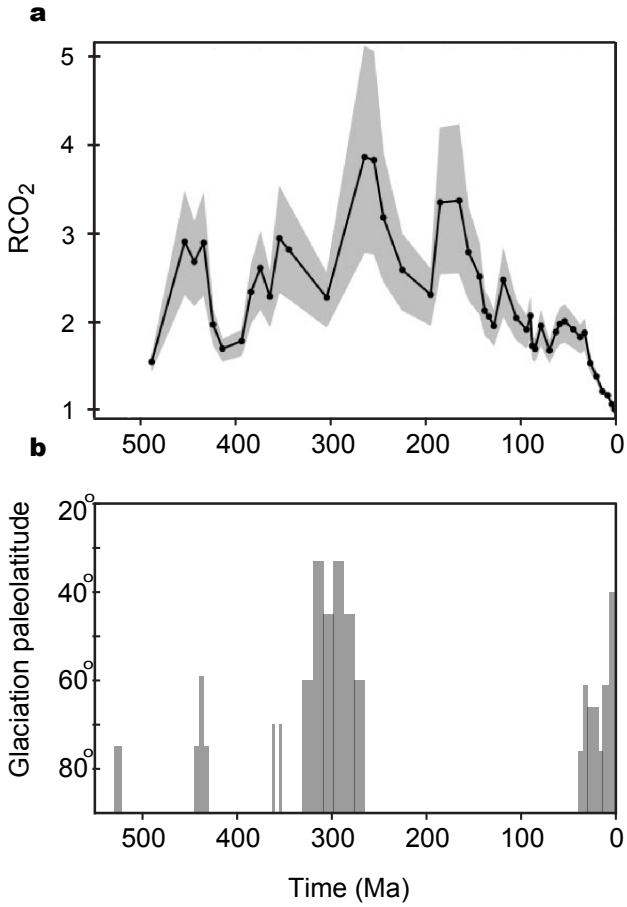

Figure 2.6.10: Phanerozoic CO_2 predictions from combined carbon and strontium isotope data, from Rothman (2001) **a,** CO_2 concentration relative to present day. **b,** Paleolatitude of continental glaciations (as in fig 2.6.8).

2.7 Phanerozoic O_2 predictions

2.7.1 Summary of O_2 predictions

The GEOCARB and COPSE models produce similar predictions for Phanerozoic CO_2. However, there are significant differences in the predictions for oxygen concentration, which are shown alongside the model CO_2 reconstructions in figure 2.7.11.

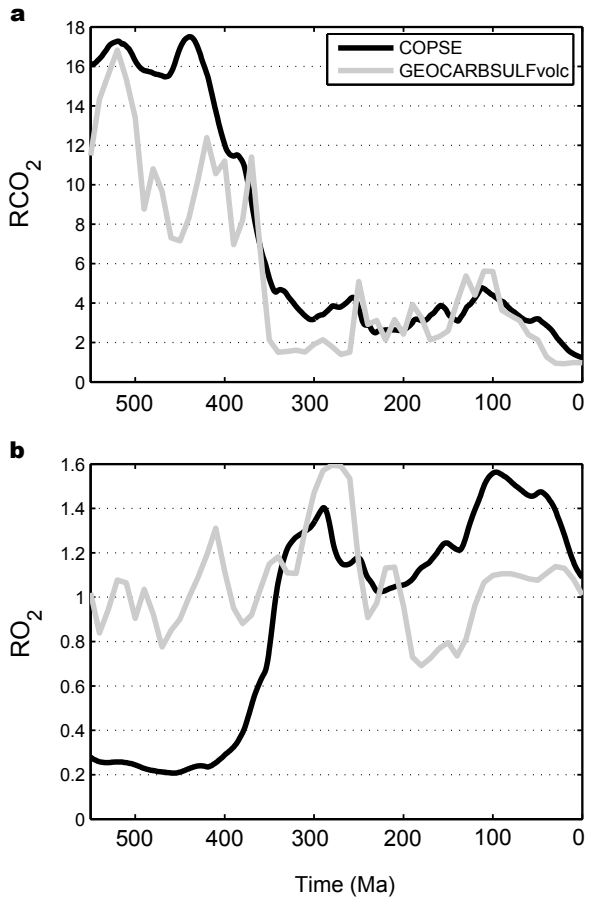

Figure 2.7.11: Phanerozoic O_2 and CO_2 predictions. a, Relative CO_2. **b,** Relative O_2. COPSE model (Bergman et al., 2004) in black, GEOCARBSULFvolc model (Berner, 2009) in grey.

As with the CO_2 predictions, there are several observations to note:

1) Both models show a significant peak in O_2 at around 300Ma, coincident with the evolution of vascular plants. Another peak is predicted in both models around 100Ma coincident with angiosperm evolution.

2) COPSE results show a step change in oxygen concentration over the period 400-300Ma, with early Phanerozoic O_2 predicted to be around 0.2PAL. The GEOCARB system predicts no step change in O_2 over the Phanerozoic, and early Cambrian O_2 concentration is predicted to be close to present day.

3) Between 200-100Ma the GEOCARB model predicts oxygen lower than present day, dropping below 0.7PAL ($\sim$ 15% of the atmosphere). In contrast, the COPSE model predicts oxygen concentration in excess of present day for this time.

4) The COPSE system produces oxygen predictions in antiphase with CO_2 for 550-300Ma, and in phase with CO_2 for 300-0Ma. GEOCARB shows no clear link between CO_2 and O_2.

2.7.2 Calculation of oxygen concentration

The GEOCARB and COPSE models estimate the change in oxygen concentration using an identical flux calculation, shown in equation 2.7.1.

$$\frac{\mathrm{dO}}{\mathrm{dt}} = \mathrm{F_{bg}} - \mathrm{F_{wg}} - \mathrm{F_{mg}} + k\left(\mathrm{F_{bps}} - \mathrm{F_{wps}} - \mathrm{F_{mps}}\right) \tag{2.7.1}$$

Here $\mathrm{F_{bg}}$ and $\mathrm{F_{bps}}$ are the burial fluxes of organic carbon and pyrite sulphur respectively, $\mathrm{F_{wg}}$, $\mathrm{F_{wps}}$ denote weathering of the organic carbon and pyrite sulphur reservoirs, $\mathrm{F_{mg}}$, $\mathrm{F_{mps}}$ denote metamorphic/degassing fluxes (see figure 2.2.1). COPSE does not make the distinction between weathering and degassing fluxes and represents both weathering and degassing with $\mathrm{F_{wg}}$ and $\mathrm{F_{wps}}$. Burial of these reduced species oxidises the surface system, whilst weathering of reduced species in the crust takes up oxygen from the atmosphere and ocean. The constant k represents the amount of oxygen taken up or released during the weathering and burial of pyrite sulphur. GEOCARB takes the value $\frac{15}{8}$ based on the stoichiometry of the burial and weathering reactions (Berner and Canfield, 1989) whilst COPSE simplifies this to 2 (changing between these values in the model runs has a negligible effect on predicted oxygen concentration). The observed differences in oxygen concentration must lie in the calculation of the fluxes $\mathrm{F_{bg}}$, $\mathrm{F_{bps}}$, $\mathrm{F_{wg}}$, $\mathrm{F_{wps}}$, $\mathrm{F_{mg}}$, $\mathrm{F_{mps}}$.

2.7.3 Method for calculating organic burial in GEOCARB

The GEOCARB method follows very closely previously described isotope mass balance modelling techniques, in which the isotope records of carbon and sulphur are used to aid calculation of the organic burial rates (Berner,

1987, 2001). The method was originally proposed by Garrels and Lerman (1984), who estimated changes in seawater sulphate concentration from the δ^{34}S record of evaporate gypsum. The overall mass of each carbon and sulphur isotope must be conserved, and assuming the long term balance of the cycles of carbon and sulphur gives the following equations:

$$(\delta_A - \alpha_A) \cdot F_{\mathrm{bg}} + \delta_A F_{\mathrm{bc}} = \delta G \cdot F_{\mathrm{wg}} + \delta G \cdot F_{\mathrm{mg}} + \delta C \cdot F_{\mathrm{wc}} + \delta C \cdot F_{\mathrm{mc}} \quad (2.7.2)$$

$$(\delta_S - \alpha_S) \cdot F_{\mathrm{bps}} + \delta_S F_{\mathrm{bgs}} = \delta_{PYR} \cdot F_{\mathrm{wps}} + \delta_{PYR} \cdot F_{\mathrm{mps}} + \delta_{GYP} \cdot F_{\mathrm{wgs}} + \delta_{GYP} \cdot F_{\mathrm{mgs}} \quad (2.7.3)$$

where δ_A,δ_G and δ_C are the δ^{13}C values for the reservoirs A, G and C respectively, and δ_S,δ_{PYR} and δ_{GYP} are the δ^{34}S values for the reservoirs S, PYR and GYP respectively. α_A and α_S are the fractionation effects associated with organic carbon burial and pyrite sulphur burial respectively.

Knowledge of the input fluxes to the surface system and the isotopic fractionation of the model reservoirs therefore allows calculation of the burial fluxes F_{bg} and F_{bps}. To solve the equations requires the assumption that the carbon and sulphur cycles are at steady state, hence $F_{\mathrm{bg}} = F_{\mathrm{wg}} + F_{\mathrm{mg}}$ and the equivalent expressions for the other crustal boxes in figure 2.2.1. Equations 2.7.2 and 2.7.3 then reduce to:

$$F_{\mathrm{bg}} = \frac{1}{\alpha_A} \left((\delta_A - \delta_G) \cdot (F_{\mathrm{wg}} + F_{\mathrm{mg}}) + (\delta_A - \delta_C) \cdot (F_{\mathrm{wc}} + F_{\mathrm{mc}}) \right) \quad (2.7.4)$$

$$F_{\mathrm{bps}} = \frac{1}{\alpha_S} \left((\delta_S - \delta_{PYR}) \cdot (F_{\mathrm{wps}} + F_{\mathrm{mps}}) + (\delta_S - \delta_{GYP}) \cdot (F_{\mathrm{wgs}} + F_{\mathrm{mgs}}) \right) \quad (2.7.5)$$

In GEOCARB, δ_A and δ_S are prescribed as model forcings, following the geological record of δ^{13}C and δ^{34}S. The isotopic composition of the other reservoirs is allowed to vary during the model run, thus allowing a semi-dynamic calculation of organic burial rates. Unlike earlier isotope mass balance models (Garrels and Lerman, 1984; Berner, 2001), the size of the

material reservoirs is allowed to change over time in the GEOCARB analysis. However, this does not cause significantly different oxygen predictions to the original works (see fig 17 in Berner (2006a) for a comparison), which closely follow the shape of the carbon isotope record used for forcing. High values in the δ^{13}C record translate to increased organic carbon burial by increasing the value of δ_A in equation 2.7.4. The same is true of the sulphur system, and the production flux of oxygen is also influenced by pyrite burial, however the present day burial rate of organic carbon is around an order of magnitude greater than the burial rate of pyrite, meaning that there is less contribution from the δ^{34}S record.

Additional assumptions are required to allow for sensible oxygen predictions via the isotope mass balance method (Kump and Garrels, 1986). The GEOCARB models explore both 'rapid recycling' between the atmosphere/ocean and younger rock reservoirs, and a dependence of fractionation effects on oxygen concentration. Figure 2.7.12 shows the rapid recycling system from Berner (1987), which is also used in GEOCARB. Each crustal reservoir is split into a 'young' and 'ancient' partition, young reservoirs undergo more rapid weathering and are smaller than the ancient reservoirs, thus are responsible for the majority of interaction with the surface system. Whilst this does not change the overall fluxes of carbon and sulphur, it leads to changes in isotopic fractionation, amplifying any isotopic signals.

In the event of an atmospheric positive isotopic excursion, for instance, the young reservoirs will quickly become isotopically heavy and will 'rapidly recycle' this signal back to the atmosphere via weathering and degassing, leading to an amplification of the original excursion. Without rapid recycling, the signal would be diluted by the large crustal reservoir size. When the isotope mass balance model is applied to the rapid recycling scheme, the resulting estimates for organic carbon and pyrite sulphur burial are lower than for the original scheme (Berner, 1987). With a higher rate of recycling, a lower burial rate is inferred from the same δ^{13}C curve.

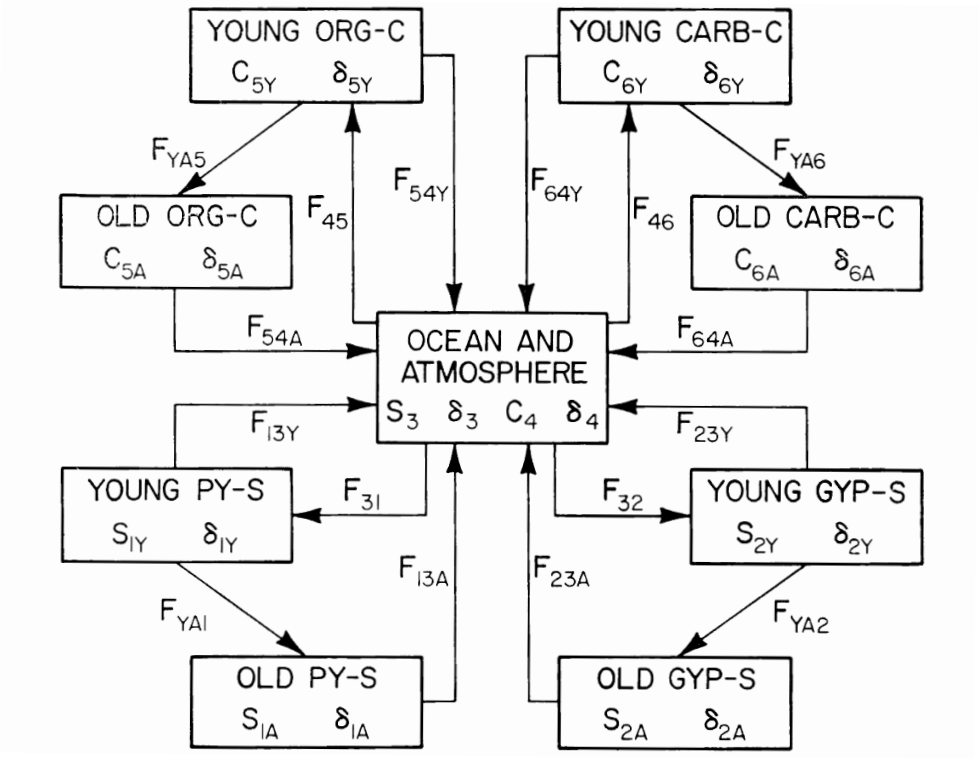

Figure 2.7.12: Rapid recycling diagram from Berner (1987). S and C denote atmosphere/ocean sulphate and carbon respectively. F describes a flux, with the subscript numbers defining the flux direction. Here Y represents fluxes of young rock, A represents fluxes of ancient rock.

Lack of negative feedback in isotope mass balance models leads to unrealistic oxygen predictions, even with the addition of rapid recycling (see fig 2 in Berner (2001)). An important feedback added to the GEOCARB isotope mass balance model is the dependence of isotopic fractionation on oxygen concentration. High oxygen levels are associated with increased plant photorespiration (Jackson and Volk, 1970), which would allow CO_2 to build up in the plant cell and could lead to increased isotopic fractionation, as is observed under high O_2 in laboratory studies (Berner et al., 2000). In GEOCARB, the parameters J and n are added to represent the dependence of isotopic fractionation on pO_2.

$$\alpha_c = 30 + J\left(\frac{\mathrm{O_2}}{\mathrm{O_2}(0)} - 1\right) \tag{2.7.6}$$

$$\alpha_s = 35\left(\frac{\mathrm{O_2}}{\mathrm{O_2}(0)}\right)^n \tag{2.7.7}$$

Here α_c denotes the isotopic difference between carbonate carbon and organic carbon in per mille (‰). Similarly α_s denotes the difference between pyrite and gypsum sulphur. A sensitivity analysis is preformed on these parameters in Berner (2001), finding that in addition to the rapid recycling scheme, values of $J = 3, n = 1$ are required to prevent negative results for $\mathrm{O_2}$. The latest GEOCARB model uses $J = 4$, $n = 1.5$ (Berner, 2009).

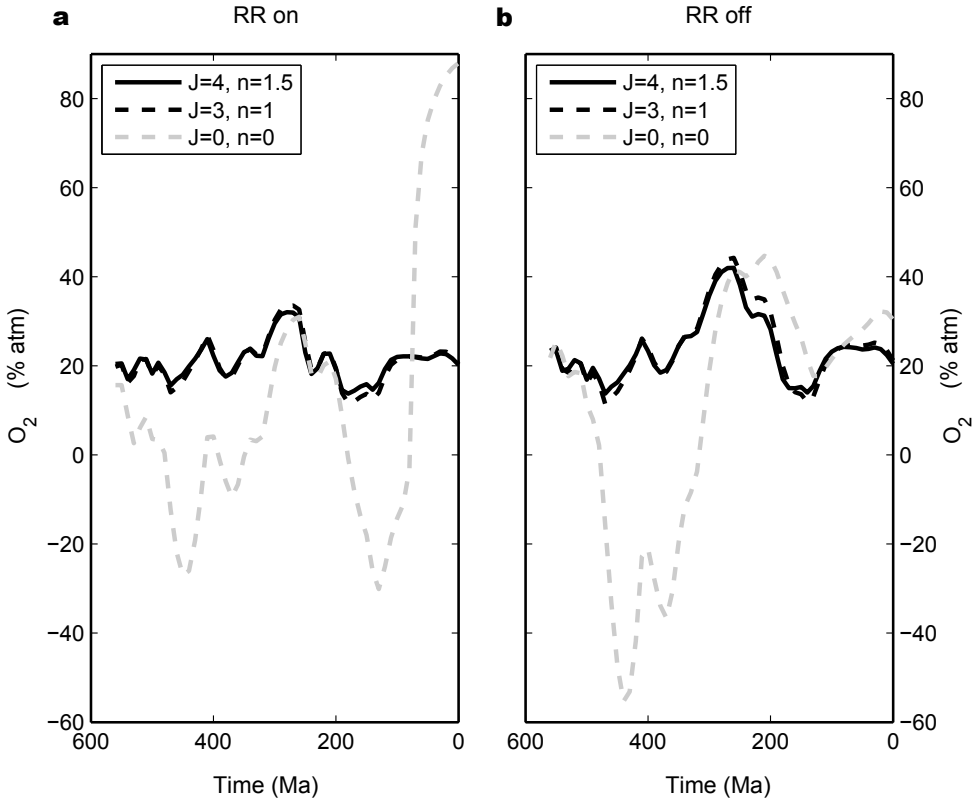

Figure 2.7.13: Strength of rapid recycling feedback in GEOCARB. Also shown are the effects of altering isotope fractionation feedback parameters J and n. **a,** Rapid recycling (standard model). **b,** Rapid recycling nullified.

To analyse the sensitivity of the GEOCARB system, it is modified to effectively nullify the rapid recycling scheme: The weathering rates of the

young and ancient reservoirs are altered so that they are weighted by reservoir mass. In figure 2.7.13 the model is run for different choices of J and n, with the rapid recycling scheme switched on or off. The figure shows that realistic oxygen concentration in the model is not possible without the negative feedback provided by oxygen-dependent fractionation (controlled by parameters J and n). The rapid recycling scheme adds further negative feedback but is not strictly required for sensible predictions, although the maximum of $\sim$ 0.4atm produced in this case is higher than believed possible due to the increased rate of biosphere burning at this concentration (Watson and Lovelock, in press), which would be expected to drastically limit the oxygen source from organic burial (Kump, 1988; Lenton, 2000).

Both the rapid recycling scheme and the isotope fractionation parameters J and n apply negative feedback to the system, which brings the oxygen predictions closer to the present day level. Another possibility is shown in figure 2.7.14, here the δ^{13}C record used for the calculation in the GEOCARB model is smoothed, producing a similar effect to the negative feedbacks. This figure also highlights the strong dependence of predicted oxygen concentration on the carbon isotope record. Running the model with constant isotope fractionation results in constant oxygen concentration (at 21%), highlighting a potential problem with extending this method further back in time than the Phanerozoic - the δ^{13}C record has remained remarkably stable throughout the whole of Earth history (Shields and Veizer, 2002) and would imply relatively stable oxygen concentration by this method, however it is widely believed that oxygen concentration has varied by many orders of magnitude (Scott et al., 2008; Papineau et al., 2007). The solution to this apparent long-term inconsistency may require the consideration of additional fractionation effects in the carbon cycle, such as those associated with hydrothermal carbonatization of oceanic crust (Bjerrum and Canfield, 2004).

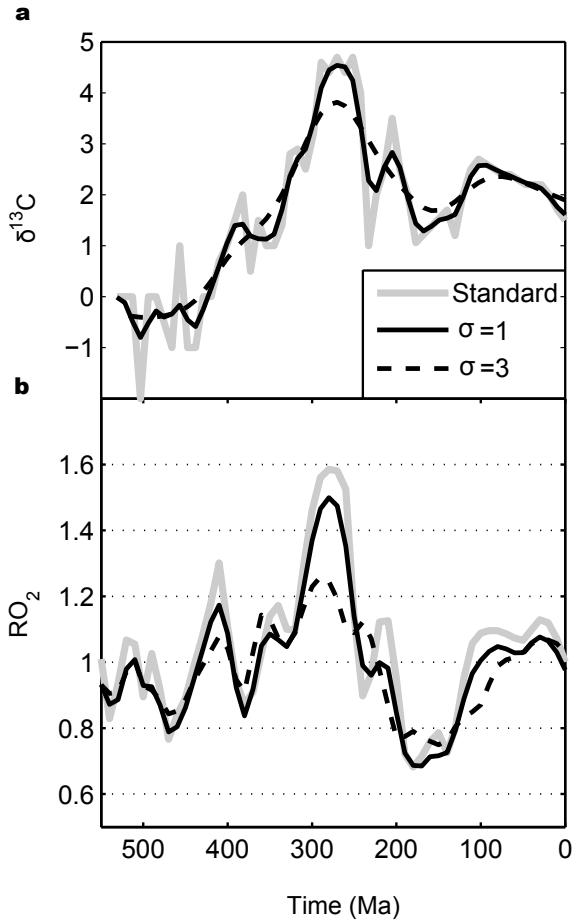

Figure 2.7.14: Effect of smoothing isotope records in GEOCARB. a, Gaussian kernel smoothing with $\sigma = 1$ and $\sigma = 3$ applied to isotope record, which is used as a forcing in GEOCARB. **b,** Model results for RO_2 subject to forcing.

2.7.4 Method for calculating organic burial in COPSE

Burial of organic carbon and pyrite in COPSE is based on an assumed biological productivity, which is calculated from the other model variables. New production scales linearly with concentration of limiting nutrient, and the sedimentation rate is assumed proportional to the square of the new production rate (see Lenton and Watson (2000a,b) and references within). Ocean nutrients nitrate and phosphate are modelled in the same way as the carbon and sulphur species, with fluxes controlling their production and removal from the surface system estimated from the present day rates and assumed dependences on model forcings and variables. Input of ocean phosphate from

weathering is calculated based on analogy to silicate, carbonate and oxidative weathering fluxes, following VanCappellen and Ingall (1994, 1996). Removal of phosphate from the ocean by burial is dependent on the rate of new production and the carbon to phosphorous ratio of organic matter. Input of nitrate is assumed to depend on the rate of nitrogen fixation, with outputs via denitrification and organic nitrate burial. The nutrient feedbacks used in COPSE are shown in figure 2.3.2. This scheme provides a simple mechanistic understanding of the nutrient and oxygen cycles that responds to changes in other model parameters, forming a closed system that requires minimal biological forcings. However, this requires a number of assumptions both in the weathering and burial fluxes, and the exact relationships between ocean nutrient and burial of organic material are uncertain (Berner, 2006a).

Figure 2.7.15 shows the effects of perturbation experiments in COPSE. The model is run in the standard manner, but all forcing functions are held constant at present day values for the entire run. At 200Ma a single forcing is doubled to observe the effects on both CO_2 and O_2. In figure 2.7.15**a**, the uplift rate (U) is doubled at 200Ma, which acts to enhance global weathering rates. Increased weathering of silicates draws down CO_2 until the system is stabilized at a lower CO_2 concentration. The weathering spike during the switch between stable states causes a brief increase in nutrient delivery, however oxygen concentration can be seen to fall in the figure. This is because the uplift rate also increases the rate of oxidative weathering on land - which draws down oxygen until the limitation on weathering due to low oxygen compensates for the increased uplift, and the system is balanced. Figure 2.7.15**b** shows the effects of a two fold increase in volcanic degassing (D) at 200Ma. This increases the volcanic CO_2 source, and atmospheric concentration rises. The system becomes stable once atmospheric CO_2 has reached such a level that the temperature-dependent CO_2 burial flux is equal to the degassing rate. The higher global weathering rates in this situation cause an increase in nutrient delivery, and in ocean nutrient concentration. This allows for a greater rate of organic carbon and pyrite burial, which increases the oxygen concentration. In 2.7.15**c**, the biotic weathering enhancement parameter W is doubled at 200Ma. W is only assumed to impact the weathering of silicates and carbonates, not oxidative weathering. The CO_2 response is very similar to figure 2.7.15**a**, due to the increased draw down via silicate weathering.

However, without the associated increase in oxidative weathering, the additional nutrient delivery as the system readjusts causes only a small transient spike in oxygen concentration.

As with the GEOCARB system, it may be problematic relating the oxygen predictions of COPSE to time before the Phanerozoic. Degassing rates were likely several times higher than present day during the Proterozoic Eon (Franck and Bounama, 1997), which would imply greatly elevated organic carbon burial rates and oxygen concentration under the COPSE assumptions.

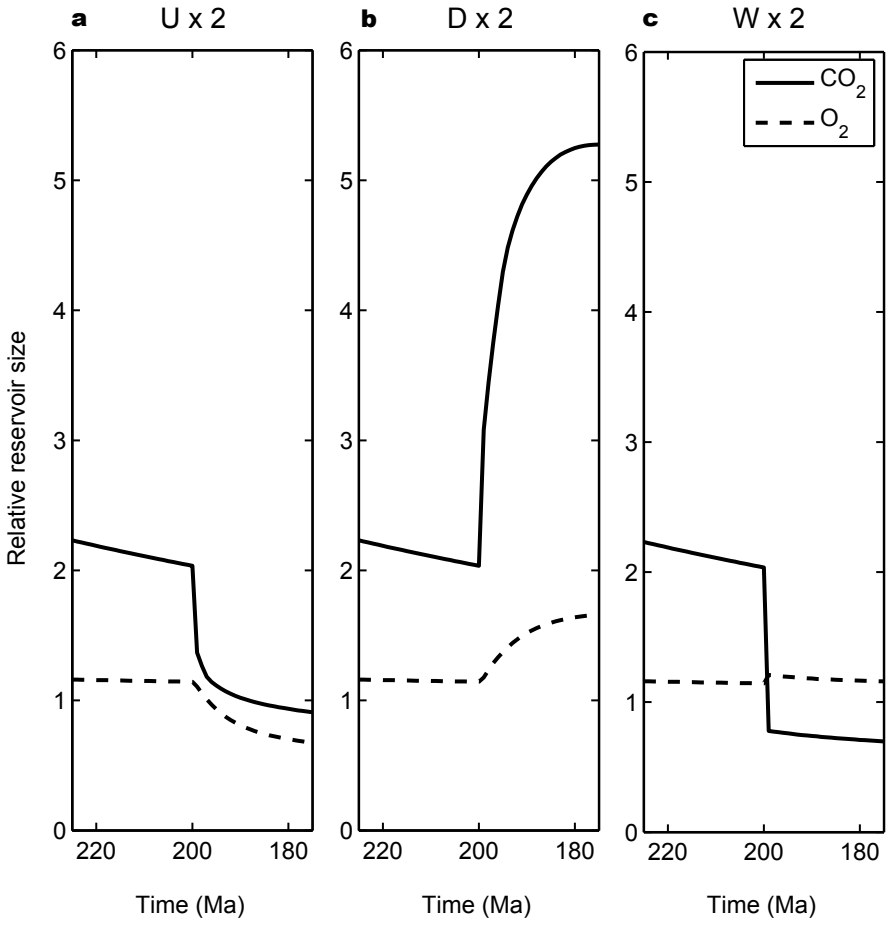

Figure 2.7.15: Effect of perturbations on CO_2 and O_2 COPSE model. All forcings are held at present day except for solar luminosity, forcings are applied for the period 200Ma-100Ma. **a,** Uplift is doubled. **b,** Degassing is doubled. **c,** Silicate/carbonate weathering is doubled. For all panels, solid line shows CO_2, dashed line shows O_2.

2.7.5 Factors controlling model O_2 predictions

Figure 2.7.15 relates the oxygen predictions from COPSE (panel a-c) and GEOCARB (panel d-f) to the model processes and forcings which most impact the estimates. Burial of organic carbon is the major oxygen source, and it can be seen in both models that the predicted oxygen concentration follows very closely the calculated rate of organic carbon burial. The weaker oxygen source from pyrite burial, and the variation in the weathering and degassing sinks also impact the predictions, but do not exert significant control. The bottom panels attempt to distinguish the forcing functions that control the organic carbon burial rate in both models.

In COPSE, the rate of organic burial depends predominantly on three model forcings (figure 2.7.16**c**). The carbon-to-phosphorus burial ratio on land ($\sim$ 1000 mol/mol) is greater than in the ocean ($\sim$ 250 mol/mol), meaning the same nutrient supply results in greater rates of burial after the evolution of land plants (E). The beginning of land-based carbon burial causes the step change in oxygen concentration at around 350ma in COPSE. An additional model forcing (CPland) doubles the carbon-to-phosphorus burial for the Permo-Carboniferous period, representing the abundance of coal swamps at this time (Bergman et al., 2004). This causes a significant transient peak in carbon burial, which then declines as the forcing is relaxed. The second carbon burial and oxygen peak at $\sim$100Ma is due primarily to the peak in the degassing forcing (D) at this time, and corresponds to the situation in fig 2.7.15**b** where degassing is doubled.

In GEOCARB, the rate of organic burial can be seen to follow the qualitative shape of the δ^{13}C curve, as with other isotope mass balance models (Berner, 1987, 2001). Addition of strong negative feedbacks on burial rate results in O_2 predictions that stay close to present day concentration for the whole Phanerozoic. Low oxygen from 250-150Ma is observed in GEOCARB due to the drop in δ^{13}C at this time, which leads to predictions of low organic carbon burial in the isotope mass balance system. This combines with low δ^{34}S and hence a predicted low rate of pyrite burial. In contrast, the low δ^{13}C at the beginning of the Phanerozoic is countered by high fractionation in δ^{34}S at this time, which infers high rates of pyrite burial, keeping the overall oxygen production rate closer to the present day value.

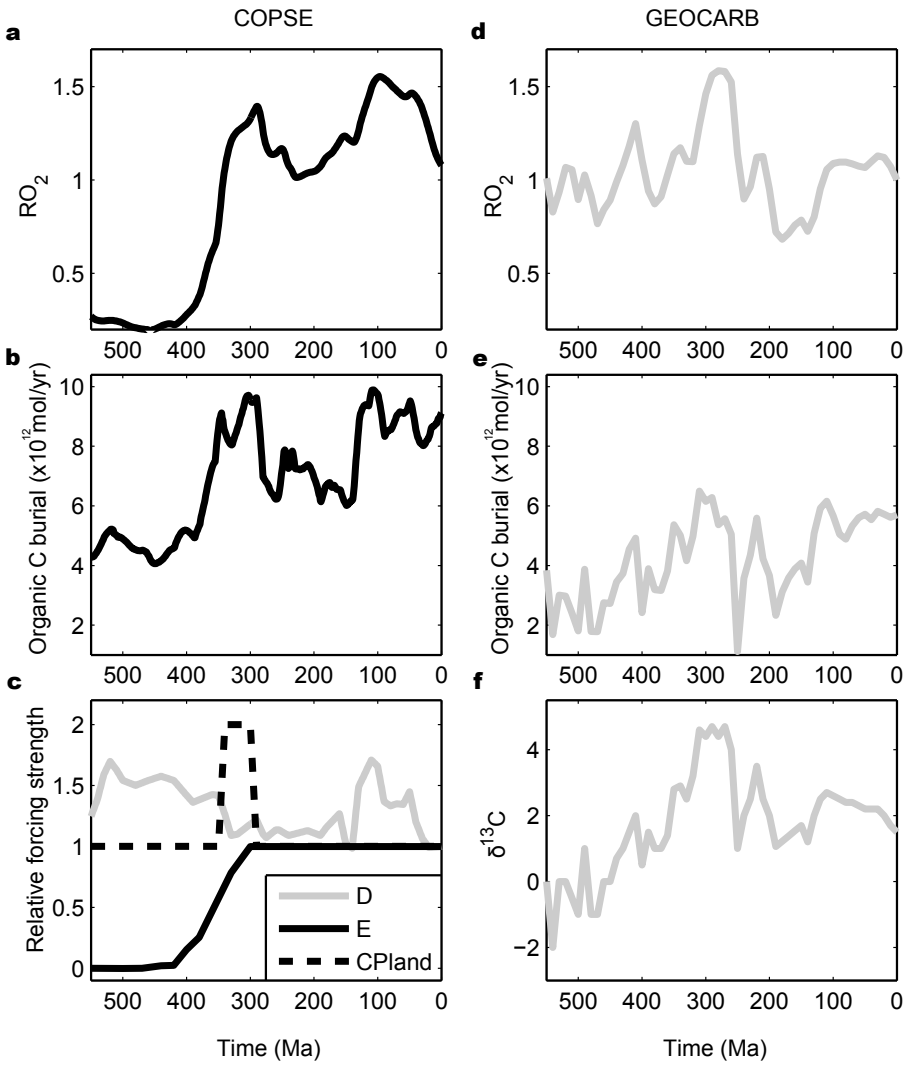

Figure 2.7.16: Controlling factors for oxygen in COPSE (a-c) and GEOCARB (d-f). The oxygen predictions of the COPSE model (**a**) are heavily dependent on the organic carbon burial rate (**b**) which is itself controlled by the degassing, evolution and carbon-to-phosphorus burial ratio forcings (**c**). Oxygen in GEOCARB (**d**) also depends heavily on organic carbon burial (**e**), which in this model is closely related to the carbon isotope fractionation forcing (**f**).

2.7.6 Comparison to O_2 proxy data

There is little direct evidence for oxygen concentration in the geological record, and the evidence that exists usually can only determine order of magnitude changes (e.g. Farquhar et al. (2000); Scott et al. (2008)). The majority of Phanerozoic oxygen predictions therefore come from modelling

investigations such as GEOCARB and COPSE. The key Phanerozoic O_2 proxy is undoubtedly the geological charcoal record, as the presence of charcoal signifies that sufficient oxygen was present for the biosphere to burn. Because charcoal has only been found for the period 400-0Ma, it is thought that during this time oxygen has remained above at least 0.13atm (Jones and Chaloner, 1991), and perhaps above 0.17atm (Belcher and McElwain, 2008; Belcher et al., 2010). As well as defining this 'fire window', predictions for oxygen concentration can be made based on the abundance of inertinite (fossilised charcoal from wildfires (Scott and Glasspool, 2007)).

The O_2 predictions of Glasspool and Scott (2010) are shown in figure 2.7.17, alongside the model predictions from GEOCARB and COPSE. The inertinite predictions group in the range 0.2-0.3atm for the majority of the 400Myr sample, which is broadly similar to the biogeochemical model outputs. The inertinite-based predictions do not support the low O_2 concentration predicted by GEOCARB for 200-100Ma, or the high O_2 predicted by COPSE for the Cenozoic. However this does not directly falsify either GEOCARB or COPSE, the authors assume that atmospheric O_2 is a function of the abundance of inertinite in rock (inert%), calibrated using the assumed Phanerozoic fire window and a power law relationship (Glasspool and Scott, 2010). Whilst this gives an understandable relationship and a useful reconstruction of oxygen, it is likely that inert% is actually a much more complex function of both climatic conditions and biosphereic attributes which define the fuel load and type.

The absence of sedimentary charcoal before 400Ma is attributed to the absence of higher plants, rather than specifically a lack of oxygen, however recent analysis of Mo isotopes and the Mo content of rocks does suggest that a step change in oxygen concentration may have occured at around 400Ma (Dahl et al., 2010). This is a feature of both the inertinite model and COPSE. A reconstruction of Phanerozoic oxygen from the abundances of organic matter in rocks again shows a similar broad result to GEOCARB and COPSE, with pronounced oxygen peaks at around 300Ma and 100Ma (Berner and Canfield, 1989). This model does agree with the lower Mesozoic oxygen concentration predicted by GEOCARB.

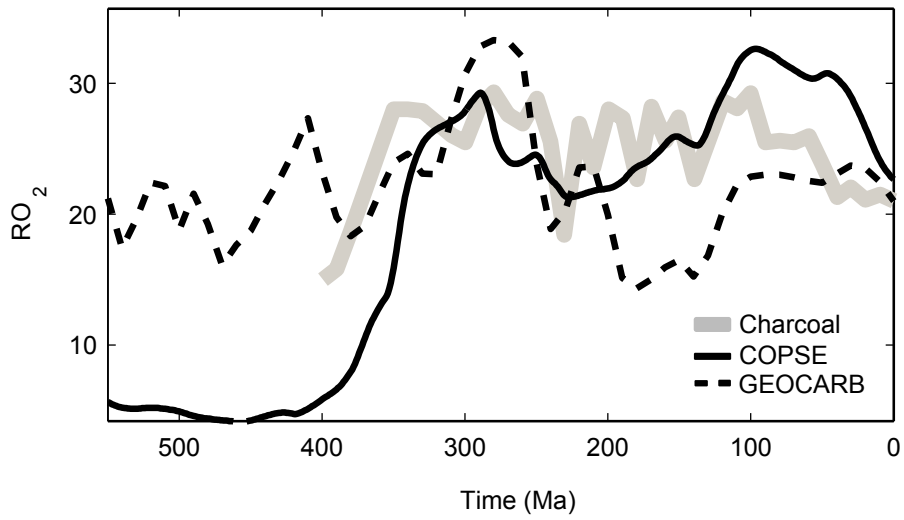

Figure 2.7.17: Phanerozoic oxygen reconstructed from charcoal record. The 'best guess' Phanerozoic O_2 curve from Glasspool and Scott (2010) is shown in grey, alongside COPSE (solid black line) and GEOCARB (dashed black line) model predictions.

Belcher et al. (2010) measured fire propagation under different concentrations of oxygen to calculate a relationship between oxygen concentration and the 'burn probability' of the biosphere as a function of atmospheric O_2. Figure 2.7.18 shows the estimated burn probability throughout the Phanerozoic under the oxygen predictions of the COPSE model (panel A) and GEOCARBSULFvolc model (panel B), these are plotted against the number of burn events recorded in the charcoal record. Very low O_2 predicted by GEOCARB for 200-100Ma is again shown incompatible with observed burn events. However, neither model shows a strong fit to these results.

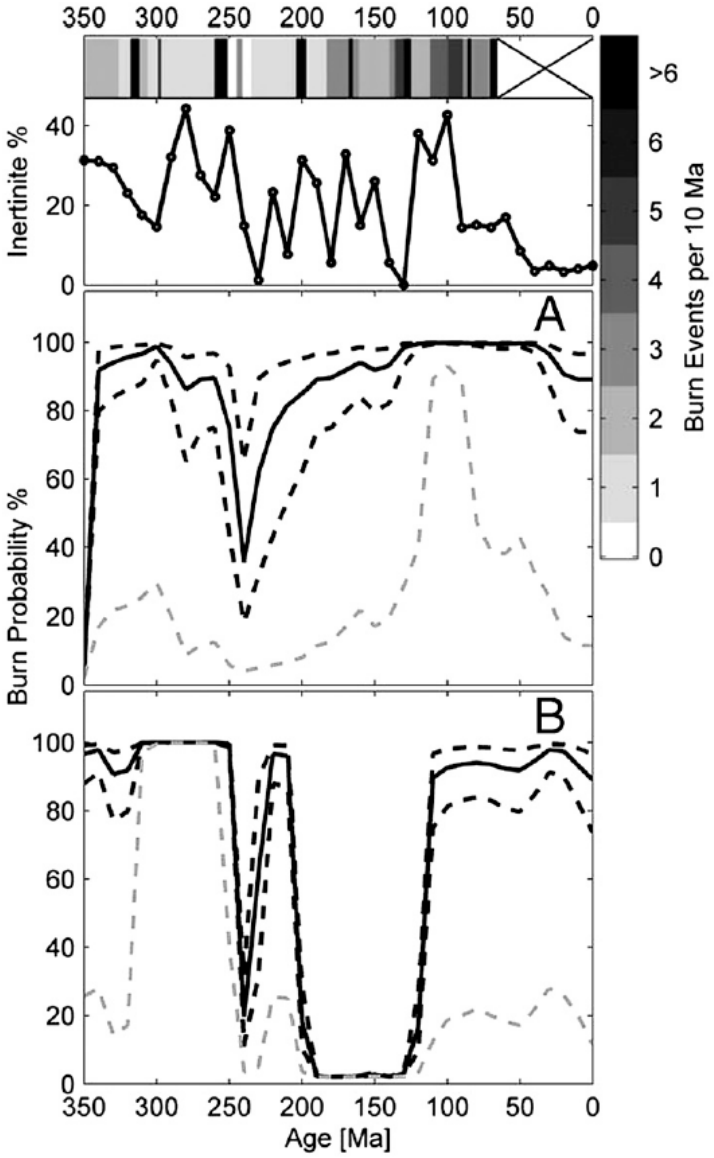

Figure 2.7.18: Burn probability throughout the Phanerozoic. a, Calculated from oxygen prediction of COPSE. **b,** Calculated from oxygen prediction of GEOCARB. Black dashed lines show interquartile range, grey dashed line shows lower 95% quartile. Also shown are the number of burn events per 10Ma (top) and the inertinite record from Glasspool and Scott (2010).

2.8 Chapter conclusions

2.8.1 Main findings

The COPSE and GEOCARB models represent extensions of the same basic system, meaning that they have many similarities. Both models are based on the 3-box carbon cycle described by Berner (Berner, 1991), and include the same 3-box system for sulphur species. Concentrations of oxygen, carbon dioxide and ocean sulphate are calculated by the same methods, which sum the source and sink fluxes between the hydrosphere and the crust.

The key difference between the models is the method of calculating burial of organic carbon and pyrite sulphur. COPSE assumes the burial fluxes are related to ocean nutrient and incorporates the ocean nutrient model of Lenton and Watson (2000a). GEOCARB does not resolve nutrient concentration and instead infers burial fluxes from the isotopic record of carbon and sulphur, incorporating a previously described isotope mass balance model to do this (Berner, 2001). GEOCARB also uses a larger set of abiotic forcings than COPSE, but this is shown not to significantly alter results over the simpler set (see fig 2.6.5). The addition of biological feedbacks in COPSE gives increased negative feedback on CO_2 concentration, allowing less variation in CO_2 than GEOCARB.

Long term predictions for CO_2 concentration in both models are dominated by the weathering enhancement associated with the evolution of vascular plants, leading to predictions of high ($>$ 10PAL) CO_2 before 350Ma, falling to close to present day thereafter. This assumption leads to the prediction of very high global temperatures for the early Phanerozoic, around 5°C warmer than today. These predictions are somewhat inconsistent with glaciations in the Cambrian and Ordovician, although sufficient model forcing (for example, attributed to the evolution of pre-vascular plants (Lenton et al., 2012)) may still drive temperatures sufficiently low for glaciation at this time. Proxy data for CO_2 is well replicated by both models for 350Ma to present, data before this period is sparse and may show elevated CO_2 levels, however the agreement between different proxies is generally poor, and some CO_2 proxy methods imply that CO_2 was relatively close to present day levels throughout the Phanerozoic.

Critically, the oxygen predictions for both models represent damped ver-

sions of the assumed organic carbon and pyrite burial fluxes, and are predominantly controlled by the organic carbon burial flux. Control in these models is placed on the production fluxes of O_2, rather than the sinks - which in general constitute simple negative feedback mechanisms and vary in response to O_2 concentration. Because the models use different methods to calculate the organic burial rates, predictions for Phanerozoic O_2 differ significantly. The O_2 predictions from GEOCARB are dominated by the shape of the $\delta^{13}C$ curve, and the COPSE predictions are controlled by the assumed plant evolution and degassing rate forcings. However, there is no detailed and easily applicable proxy with which to test these predictions, and perhaps with the exception of the low Mesozoic O_2 in the GEOCARB model, both models adequately satisfy the available oxygen constraints imposed by the abundance of fossilised charcoal.

2.8.2 Considerations for developing a Minimal Model

The next chapter will focus on building a Minimal Model of the important processes in Phanerozoic biogeochemistry, which will be used to explore possibilities for Precambrian climate. Following the analysis in this chapter, the following decisions about the model construction can be made:

1) The additional abiotic forcings included in the later GEOCARB models are not required for a Minimal Model. Their impact on predictions is smaller than the uncertainty in other major forcings.

2) The model must allow for calculation of organic burial via either a nutrient system or via isotope mass balance. Both methods produce encouraging results for Phanerozoic O_2 and require testing on a longer timescale.

3) It is highly likely that there are processes important in the Precambrian that are not expressed in these models, therefore the new model framework must be versatile and modular to allow for easy adaption.

3 Modelling the Precambrian carbon cycle

3.1 Introduction

Broadly speaking, both the COPSE and GEOCARB models produce sensible results for the changes in major atmospheric constituents over the Phanerozoic, and are backed up by the majority of available data. The only major disagreement is in the abundance of oxygen, but here the scale of the differences is smaller than can easily be validated by proxies. The intention in this thesis is to apply these analyses to the Precambrian by constructing a Minimal Model of the important processes. In this chapter a model is described and validated for the Phanerozoic against COPSE and GEOCARB. The model is then run from 900Ma to the present day and compared to available proxies. To inform the model construction, a short review of Neoproterozoic climate is necessary.

3.2 Neoproterozoic climate

The Neoproterozoic era (1000-541Ma) is characterised by massive worldwide glaciation (Halverson et al., 2005; Kirschvink, 1992), periodic perturbations to the carbon cycle (Johnston et al., 2012) and an oxygenation event in the deep ocean (Canfield et al., 2008). The timing of the oxidation and glacial events are reasonably well constrained (Macdonald et al., 2010; Scott et al., 2008), but the specific dynamics of oxygen, greenhouse gas and temperature variations are uncertain.

In figure 3.2.1 the glacial paleolatitude reconstruction of Royer et al. (2004) is extended to include the estimated timing and paleolatitudes of glaciations in the Neoproterozoic (from Hoffman and Li (2009); Condon et al. (2005); Halverson et al. (2005); Zhang et al. (2009)). The Kaigas glaciation at $\sim$ 750Ma is shown in a lighter grey, reflecting uncertainty about its global significance (Macdonald et al., 2010). Other light grey sections denote the uncertainties in the extent of the Sturtian (ending at $\sim$700Ma) and Marinoan (ending at $\sim$635Ma) glaciations. It has been suggested that these two glaciations may be examples of 'snowball Earth' events (Kirschvink, 1992; Hoffman et al., 1998), in which positive feedback between planetary ice cover and albedo causes ice sheets to reach the equator, locking the planet into a

high albedo state. This state would persist until sufficient volcanic CO_2 had accumulated in the atmosphere to trigger melting, which would be expected to take $\sim 10^7$ years (Le Hir et al., 2008). Glacial evidence has been found at very low paleolatitudes for both glacial periods, and the inferred durations from the isotope record of carbon are similar to those predicted in the snowball scenario. However these observations may be equally well explained by a series of large glaciations happening over each period (Allen and Etienne, 2008). The Gaskiers glaciation (580Ma) is well constrained and it is unlikely that it extended to low latitudes, although there is some data that suggests this may be a possibility (Hoffman and Li, 2009).

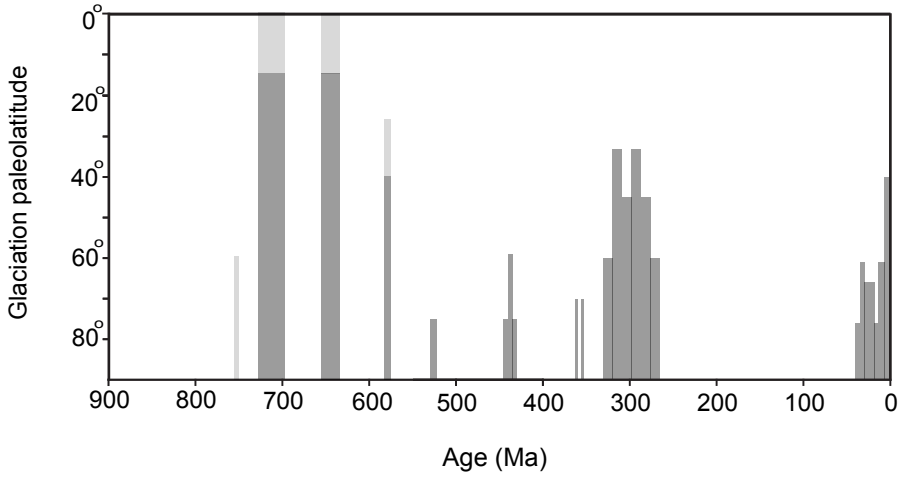

Figure 3.2.1: Glacial paleolatitude for 900-0Ma Record of Royer et al. (2004) extended using data from Hoffman and Li (2009); Condon et al. (2005); Halverson et al. (2005); Macdonald et al. (2010); Zhang et al. (2009).

To trigger the severe glaciations in the Neoproterozoic era, global average surface temperature must have been significantly lower than today, perhaps around 10°C (Hoffman and Schrag, 2002). CO_2 concentration during the Neoproterozoic must have therefore been sufficiently low to allow for these temperatures, although the trigger for the events may not have been CO_2 related (Pavlov et al., 2003). Estimates for Neoproterozoic CO_2 concentration have been made by using an isotope model to account for changes in the marine carbon reservoir size (Kah and Bartley, 2004), the results show CO_2

declining from $\sim$ 10PAL to $\sim$ 1PAL over the era, which correlates broadly with glaciation in the late Neoproterozoic.

The deep ocean was likely anoxic and ferruginous throughout the Neoproterozoic era, with some surface oxygenation in the late Neporoterozoic and deep ocean ventilation occurring after the Gaskiers glaciation (580Ma) (Canfield et al., 2007; Scott et al., 2008; Frei et al., 2009). During the earlier Proterozoic, the ocean was anoxic and may have been euxinic (sulphidic and anoxic) (Canfield, 1998). Figure 3.2.2 shows a summary of late Neoproterozoic ocean conditions based on data for the speciation of iron in sedimentary rocks (Canfield et al., 2008). In sediments deposited under oxic conditions, a smaller fraction of the total iron exists in a chemically reactive form (Raiswell and Canfield, 1998), allowing estimation of local redox conditions using the ratio of highly reactive iron (FeHR) to total Fe. Calculating the proportion of FeHR bound as sulphide also allows some distinction between ferruginous and euxinic conditions. These data show possible surface ocean oxygenation throughout the Neoproterozoic, with the oxygenation of the deep ocean occurring around the time of the Gaskiers glaciation.

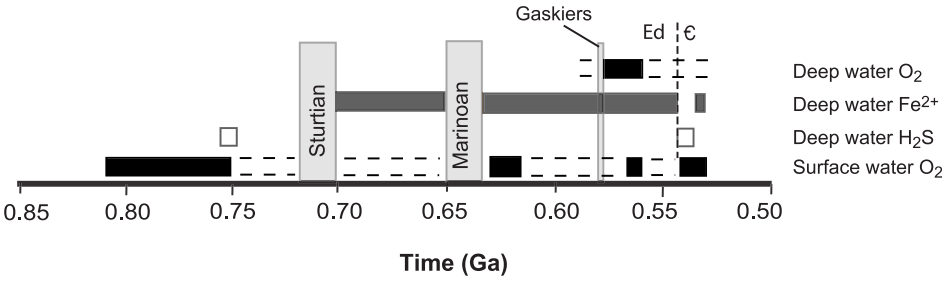

Figure 3.2.2: Ocean chemical conditions as described in Canfield et al. (2008). Solid blocks represent distinct evidence for chemical conditions, dashed lines represent uncertainty. Neoproterozoic glaciations shown as vertical grey bars.

Enrichments of the redox-sensitive metal, molybdenum (Mo) in euxinic black shales also suggest deep ocean oxygenation occurring around 663-551Ma. Figure 3.2.3 shows this enrichment in ppm throughout earth history, which is proposed to represent changes in the input flux from oxidative weathering of the continents (Scott et al., 2008). Note the displayed Mo enrichment earlier in the Precambrian agrees with many other lines of ev-

idence that describe the 'Great Oxidation Event' at 2.4Ga (Holland, 2006; Farquhar et al., 2000; Catling et al., 2001; Kasting, 2001). An isotope mass balance model based on the δ^{98}Mo values of euxinic sediments also supports oxygenation at 580Ma (Dahl et al., 2010).

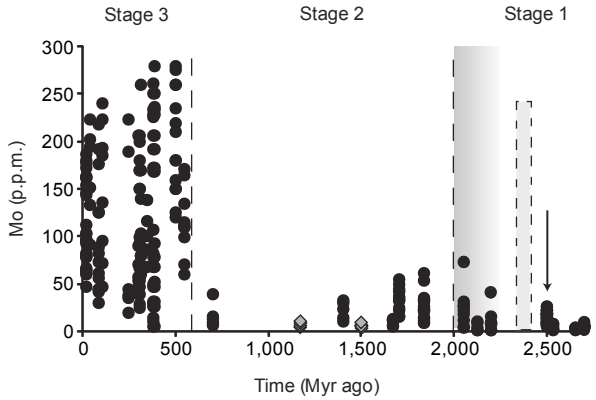

Figure 3.2.3: Mo enrichment in black shales. Black circles are from euxinic environments, grey diamonds are from non-euxinic, organic-rich shales. Figure copied from Scott et al. (2008). Stages 1, 2 and 3 represent stepwise process of planetary oxygenation proposed by the authors. Note the x-axis in this figure is reversed when compared to the other figures in this work.

Whilst there are some quantitative estimates for Neoproterozoic CO_2, the above oxygen proxies do not allow a similar prediction, instead focussing on the major changes in redox state. Radiation of sulphide-oxidising bacteria, and the accompanying increase in sulphur isotope fractionation, is thought to be the result of atmospheric oxygen concentration increasing above a threshold of about $\sim 0.05 - 0.2$PAL during the Neoproterozoic era (Canfield and Teske, 1996). Earlier Proterozoic oxygen concentration has been constrained using paleosol data to ≥ 0.03 atm (0.15PAL) (Rye and Holland, 1998). The Ediacaran biota, which appear at ∼570Ma, have an estimated minimum oxygen requirement of 0.01PAL (Runnegar, 1991), whilst the physiological oxygen requirement for Cambrian animals is proposed to be > 0.1PAL (Rhoads and Morse, 1971). A rough estimation of oxygen concentration based on these combined proxies gives $0.01 - 0.2$PAL for the early Neoproterozoic. After 580Ma the deep ocean becomes oxygenated and atmospheric O_2 concentration rises to between $0.05 - 1$PAL. A model for the Neoproterozoic

carbon and sulphur cycles should allow for oxygen concentration within the expected range of $0.01 - 1$PAL, as well as global average surface temperature $\leq 10°$C.

3.3 Model development

3.3.1 Box scheme and reservoir calculations

A box model is now developed (hereafter the 'Minimal Model') and follows directly the GEOCARB and COPSE formulation (Berner, 1991), using the reservoir and flux definitions from chapter 2, shown in figure 2.2.1. The system equations are shown below:

Carbon cycle

Carbon can exist as CO_2 in the atmosphere/ocean box (A), and either oxidised carbonate (C) or reduced organic carbon (G) in the crust. Following fig 2.2.1, changes in the reservoirs over time are calculated by summing sources and sinks via weathering, degassing and burial.

$$\frac{\mathrm{dA}}{\mathrm{dt}} = \mathrm{F_{mg}} + \mathrm{F_{wg}} + \mathrm{F_{mc}} + \mathrm{F_{wc}} - \mathrm{F_{bg}} - \mathrm{F_{bc}} \tag{3.3.1}$$

$$\frac{\mathrm{dG}}{\mathrm{dt}} = \mathrm{F_{bg}} - \mathrm{F_{mg}} - \mathrm{F_{wg}} \tag{3.3.2}$$

$$\frac{\mathrm{dC}}{\mathrm{dt}} = \mathrm{F_{bc}} - \mathrm{F_{mc}} - \mathrm{F_{wc}} \tag{3.3.3}$$

Sulphur cycle

Sulphur exists in the model as marine sulphate in the atmosphere/ocean box (S), and either oxidised gypsum (GYP) or reduced pyrite (PYR) in the crust. Again following fig 2.2.1 we have:

$$\frac{\mathrm{dS}}{\mathrm{dt}} = \mathrm{F_{wps}} + \mathrm{F_{wgs}} - \mathrm{F_{bps}} - \mathrm{F_{bgs}} + \mathrm{F_{mps}} + \mathrm{F_{mgs}} \tag{3.3.4}$$

$$\frac{\mathrm{dPYR}}{\mathrm{dt}} = \mathrm{F_{bps}} - \mathrm{F_{wps}} - \mathrm{F_{mps}} \tag{3.3.5}$$

$$\frac{\mathrm{dGYP}}{\mathrm{dt}} = \mathrm{F_{bgs}} - \mathrm{F_{wgs}} - \mathrm{F_{mgs}} \tag{3.3.6}$$

3.3.2 Phanerozoic forcings

A subset of the model forcings from the GEOCARB and COPSE models is used, aiming to include the most relevant forcings without overcomplicating the model. To begin with, forcings are only prescribed for the Phanerozoic, following exactly from GEOCARB and COPSE. The current models use differing formulations to express weathering enhancement due to vascular plants, which does not significantly impact results (see figure 2.6.5), for the Minimal Model the COPSE formulation is chosen. GEOCARB and COPSE also use a different expression for global temperature dependence on solar luminosity and CO_2 concentration, however these return very similar values for the parameter ranges that are covered in model runs. For this model I use the change in solar luminosity, and energy balance temperature approximation described by Caldeira and Kasting (Caldeira and Kasting, 1992), as used in COPSE. Model forcings are outlined in the tables below, following the functions and naming conventions from figure 2.4.3. The model is run using a general forcing set in conjunction with either the COPSE or GEOCARB biological forcing set.

Name	**Symbol**	**Source**
Uplift rate	U	GEOCARB,COPSE
Degassing rate	D	GEOCARB,COPSE
Burial depth of carbonates	B	GEOCARB,COPSE
Biotic weathering enhancement	W	COPSE (≈fE in GEOCARB)
Solar luminosity	S	COPSE

Table 1: General forcings for Minimal Model

Name	**Symbol**	**Source**
Evolution of vascular plants	E	COPSE
C-P burial ratio on land	$CPland$	COPSE

Table 2: Additional forcings for COPSE productivity system

Name	Symbol	Source
Atmospheric carbon δ^{13}C	δ_A	GEOCARB
Ocean sulphate δ^{34}S	δ_S	GEOCARB

Table 3: Additional forcings for GEOCARB productivity system

3.3.3 Weathering dependencies and fluxes

Silicate weathering

The expression for the dependence of silicate weathering on temperature and CO_2 concentration is shared by COPSE and GEOCARB. To increase robustness to temperature the derivation of Berner (1994) is followed without making the assumption of temperature close to present day. The linear runoff formulation used in the original models becomes invalid when temperature is very low, and is amended by approximation with an exponential term. The resulting equation is:

$$\mathrm{f_{silw}} = e^{\left(k_{fs1}\frac{T-T_0}{TT_0}\right)}\left(e^{k_{fs2}(T-T_0)}\right)^{0.65}\sqrt{\mathrm{RCO_2}} \tag{3.3.7}$$

here $k_{fs1} = 7537.69$ and $k_{fs2} = 0.03$. T is average surface temperature in Kelvin, T_0 is present day average surface temperature and $\mathrm{RCO_2}$ denotes concentration of CO_2 normalised to pre-industrial concentration. The dependence on $\mathrm{RCO_2}$ for pre-vascular plants is added, but the alteration of this term in the mid Phanerozoic is left out for simplicity.

Carbonate weathering

The expressions for weathering of carbonates and oxidised sulphur are shared by the GEOCARB and COPSE models, again the original linear term is approximated by an exponential to prevent collapse at low temperature:

$$\mathrm{f_{carbw}} = e^{k_{fc}T}\sqrt{\mathrm{RCO_2}} \tag{3.3.8}$$

where $k_{fc} = 0.05$.

Oxidative weathering

Oxidative weathering of reduced organic carbon and pyrite sulphur is allowed a dependence on O_2 concentration as follows:

$$\mathrm{f_{oxidw}} = (\mathrm{RO_2})^a \tag{3.3.9}$$

here RO_2 is the atmospheric oxygen concentration normalised to present. Dependence on oxygen concentration (Lasaga and Ohmoto, 2002) is used in COPSE, but not in GEOCARB. In the Minimal Model, a is allowed to take the value of 0.5 (Lasaga and Ohmoto, 2002) when the COPSE productivity system is used, or a null-dependence of $a = 0$ when the GEOCARB system is used (Berner, 2006a).

Full weathering fluxes

The dependences above are multiplied by the appropriate forcing functions and the size of the flux at present day to arrive at the full flux equation. As in both previous models (Berner, 1994; Bergman et al., 2004), all weathering fluxes are assumed to depend on the uplift rate, U. Silicate and carbonate weathering are assumed to be influenced by an enhancement due to the evolution of land plants, W, and the rates of weathering for the crustal reservoirs are assumed to depend on reservoir size. The weathering flux equations are thus:

$$silw = k_{silw} \cdot (k_{\mathrm{preplant}} + (1 - k_{\mathrm{preplant}})W) \cdot U \cdot \mathrm{f_{silw}} \tag{3.3.10}$$

$$carbw = k_{carbw} \cdot (k_{\mathrm{preplant}} + (1 - k_{\mathrm{preplant}})W) \cdot U \cdot \mathrm{f_{carbw}} \tag{3.3.11}$$

$$oxidw = k_{oxidw} \cdot U \cdot \frac{G}{G_0} \cdot \mathrm{f_{oxidw}} \tag{3.3.12}$$

$$pyrw = k_{pyrw} \cdot U \cdot \frac{PYR}{PYR_0} \cdot \mathrm{f_{oxidw}} \tag{3.3.13}$$

$$gypw = k_{gypw} \cdot U \cdot \frac{GYP}{GYP_0} \cdot \mathrm{f_{carbw}} \tag{3.3.14}$$

Here $silw$ = silicate weathering, $carbw$ = carbonate weathering, $oxidw$ = oxidative weathering, $pyrw$ = pyrite weathering and gyp = gypsum weathering. k_{silw}, k_{carbw}, k_{oxidw}, k_{pyrw} and k_{gypw} denote the present day flux sizes in moles per year. G, C, PYR, GYP are the sizes of the crustal reservoirs. k_{preplant} denotes the reduced weathering efficiency before vascular plants (equivalent to k_{15} in COPSE, or k_{LIFE} in GEOCARB), and represents $1/k_{\mathrm{vp}}$, where k_{vp} is the vascular plant weathering enhancement factor.

3.3.4 Metamorphic/degassing fluxes

Degassing fluxes are assumed to depend only on the global rate of degassing, D, and the relative crustal abundance of each species. Carbonate degassing is assumed to increase in the Mesozoic following the carbonate-burial depth forcing B, as in both the previous models.

$$ocdeg = k_{ocdeg} \cdot D \cdot \frac{G}{G_0} \tag{3.3.15}$$

$$ccdeg = k_{ccdeg} \cdot D \cdot B \cdot \frac{C}{C_0} \tag{3.3.16}$$

$$pyrdeg = k_{pyrdeg} \cdot D \cdot \frac{PYR}{PYR_0} \tag{3.3.17}$$

$$gypdeg = k_{gypdeg} \cdot D \cdot \frac{GYP}{GYP_0} \tag{3.3.18}$$

Where $ocdeg$ = organic carbon degassing, $ccdeg$ = carbonate carbon degassing, $pyrdeg$ = pyrite degassing, $gypdeg$ = gypsum degassing. Constants k_{ocdeg} and k_{ccdeg}, k_{pyrdeg} and k_{gypdeg} are the present day degassing fluxes for organic carbon and carbonates, pyrite sulphur and gypsum.

3.3.5 Burial of oxidised species

Following both previous models, I assume that over long timescales, all the carbon delivered to the ocean via silicate and carbonate weathering is deposited as marine carbonates. Thus:

$$mccb = silw + carbw \tag{3.3.19}$$

The expression for deposition of gypsum sulphur allows dependence on the size of the marine sulphate reservoir (Rees, 1970):

$$mgsb = k_{\mathrm{mgsb}} \cdot \frac{S}{S_0} \tag{3.3.20}$$

Where k_{mgsb} is the present day burial flux.

3.3.6 Optional burial of reduced species via isotope mass balance

The method described in section 2.7.3 is implemented into the model as a set of optional extra equations. Burial of organic carbon and pyrite sulphur follow equations 2.7.4 and 2.7.5. They are subject to the isotope forcings δ_A and δ_S and the oxygen dependent fractionation effects α_c and α_s (shown in equations 2.7.6 and 2.7.7). Calculation of $\mathrm{F_{bg}}$ and $\mathrm{F_{bps}}$ via this method requires knowledge of the isotopic fractionation for the crustal reservoirs at each time step. This is achieved using the same method as employed by GEOCARBSULF (Berner, 2006a): for each reservoir, X, the quantity $X \cdot \delta^{13}\mathrm{C}\,(X)$, expressing the size of the reservoir multiplied by its isotopic fractionation , is calculated. This is simpler than tracking the isotopic value explicitly, and this quantity can be divided by reservoir size to obtain the fractionation value. For simplicity, the rapid recycling scheme (Berner, 1987) is not used in this model.

3.3.7 Optional burial of reduced species via ocean nutrient model

For an alternative model solution, a simplified version of the COPSE nutrient system is employed. A single limiting nutrient is assumed and modelled as phosphate using the COPSE equations (Bergman et al., 2004; VanCappellen and Ingall, 1994, 1996). For nutrient weathering we have:

$$phosw = k_{\mathrm{phosw}} \left(\frac{2}{12} \frac{silw}{k_{\mathrm{silw}}} + \frac{5}{12} \frac{carbw}{k_{\mathrm{carbw}}} + \frac{5}{12} \frac{oxidw}{k_{\mathrm{oxidw}}} \right) \tag{3.3.21}$$

where k_{phosw} is the present day rate of weathering. An assumed quantity of weathered nutrient ($pland$) is used by the land biota (if present), the remaining nutrient ($psea$) is transferred to the ocean.

$$pland = k_{\mathrm{landfrac}} \cdot VEG \cdot phosw \tag{3.3.22}$$

$$psea = phosw - pland \tag{3.3.23}$$

Following COPSE, $k_{\text{landfrac}} = 0.10345$ is the present day fraction of weathered phosphate that is used on land, and VEG represents the relative mass of the terrestrial biosphere, a complex internal variable which depends on the concentration of O_2, CO_2 and the surface temperature and is derived from various previous works (Caldeira and Kasting, 1992; Volk, 1987; Fridovich, 1977; Lenton and Watson, 2000b). This includes a simple temperature relationship, VEG_{T}, which assumes maximum productivity at 25°C, a Michaelis-Menten type dependency on carbon dioxide concentration, VEG_{CO_2}, and a linear representation of the effects of oxygen toxicity and increased rates of photorespiration, VEG_{O_2}. See the COPSE paper for full details (Bergman et al., 2004). As in COPSE, an approximation (VEG_{fire}) is added for damage to vegetation by wildfires based on oxygen concentration, and a dependence on the evolutionary forcing, E, to represent lack of vegetation feedback before vascular plant proliferation.

$$VEG = E \cdot VEG_{\text{O}_2} \cdot VEG_{\text{CO}_2} \cdot VEG_T \cdot VEG_{\text{fire}} \tag{3.3.24}$$

$$VEG_{\text{O}_2} = 2\left(1.5 - 0.5\text{RO}_2\right) \tag{3.3.25}$$

$$VEG_{\text{CO}_2} = \frac{\text{CO}_2(\text{ppm}) - 10}{183.6 + \text{CO}_2(\text{ppm}) - 10} \tag{3.3.26}$$

$$VEG_T = 1 - \left(\frac{T - 298}{298}\right)^2 \tag{3.3.27}$$

$$VEG_{\text{fire}} = \frac{k_{\text{fire}}}{k_{\text{fire}} - 1 + \max\left(586.2 \cdot \text{RO}_2 - 122.102, 0\right)} \tag{3.3.28}$$

Burial of organic carbon on land is now assumed proportional to the nutrient delivery to land, *pland*, and the carbon-to-phosphorus burial ratio for land plants, $CPland$.

$$locb = k_{\mathrm{locb}} \cdot \frac{pland}{pland_0} \cdot CPland \tag{3.3.29}$$

here $pland_0$ represents the present day flux of nutrient to the land biota and the forcing $CPland$ is also defined relative to present day (i.e. $CPland = 1$ for the present). Marine organic carbon burial is assumed to be proportional to the concentration of ocean phosphate, with the addition of a nonlinearity to account for increased burial in shelf regions, following Lenton and Watson (2000a):

$$mocb = k_{\mathrm{mocb}} \left(\frac{P}{P_0} \right)^2 \tag{3.3.30}$$

Burial of pyrite is assumed to occur after bacterial sulphate reduction, and therefore depends on the concentration of marine sulphate (Holland, 1978; Holser et al., 1988) and the rate of organic carbon burial (Raiswell and Berner, 1986). A dependence on oxygen is also added to simulate the inhibition of these anaerobic organisms by increasing oxygen concentration (Berner and Canfield, 1989):

$$mpsb = k_{\mathrm{mpsb}} \cdot \frac{S}{S_0} \cdot \frac{1}{\mathrm{RO}_2} \cdot \frac{mocb}{mocb_0} \tag{3.3.31}$$

Burial of nutrient follows the COPSE system for phosphate burial, assuming three removal pathways to mimic the weathering process: Calcium-associated burial (*capb*), iron-sorbed phosphate removal ($fepb$) and organic phosphate burial (*mopb*) (VanCappellen and Ingall, 1994; Holland, 1994; Broecker and Peng, 1982), with the following dependencies:

$$mopb = k_{\mathrm{mopb}} \frac{mocb}{mocb_0} \tag{3.3.32}$$

$$capb = k_{\mathrm{capb}} \frac{mocb}{mocb_0} \tag{3.3.33}$$

$$fepb = \frac{k_{\text{fepb}}}{k_{oxfrac}} \left(1 - anox\left(O, P\right)\right) \tag{3.3.34}$$

where *anox* is a function representing the degree of ocean anoxia:

$$anox = 1 - k_{\text{oxfrac}} \left(\frac{O}{O_0} \frac{P_0}{P}\right) \tag{3.3.35}$$

here $k_{\text{oxfrac}} = 0.86$ is the present day oxic fraction.

3.3.8 Full model equations

These fluxes are now substituted into the carbon and sulphur cycle schematics shown in figure 2.2.1, allowing $\text{F}_{\text{bg}} = mocb{+}locb$ (for the isotope mass balance model, it is assumed that the calculated organic burial reflects the sum of land and ocean burial), $\text{F}_{\text{bc}} = silw + carbw$, $\text{F}_{\text{bps}} = mpsb$, $\text{F}_{\text{bgs}} = mgsb$, $\text{F}_{\text{wg}} = oxidw$, $\text{F}_{\text{wc}} = carbw$, $\text{F}_{\text{wps}} = pyrw$, $\text{F}_{\text{wgs}} = gypw$, $\text{F}_{\text{mg}} = ocdeg$, $\text{F}_{\text{mc}} = ccdeg$, $\text{F}_{\text{mps}} = pyrdeg$, $\text{F}_{\text{mgs}} = gypdeg$ We now have the following set of ordinary differential equations:

$$\frac{\text{dA}}{\text{dt}} = ocdeg + oxidw + ccdeg - mocb - locb - silw \tag{3.3.36}$$

$$\frac{\text{dG}}{\text{dt}} = mocb + locb - ocdeg - oxidw \tag{3.3.37}$$

$$\frac{\text{dC}}{\text{dt}} = silw - ccdeg \tag{3.3.38}$$

$$\frac{\text{dS}}{\text{dt}} = pyrw + gypw - mpsb - mgsb \tag{3.3.39}$$

$$\frac{\text{dPYR}}{\text{dt}} = mpsb - pyrw - pyrdeg \tag{3.3.40}$$

$$\frac{\text{dGYP}}{\text{dt}} = mgsb - gypw - gypdeg \tag{3.3.41}$$

And for ocean nutrient, P:

$$\frac{\mathrm{dP}}{\mathrm{dt}} = psea - capb - fepb - mopb \tag{3.3.42}$$

Nutrient concentration is ignored if the isotope mass balance model is used. The size of the oxygen reservoir is calculated in the same manner as for the GEOCARB and COPSE models, taking the $\frac{15}{8}$ multiplier from GEOCARB:

$$\frac{\mathrm{dO}}{\mathrm{dt}} = mocb + locb - ocdeg - oxidw + \frac{15}{8}\left(mpsb - pyrw - pyrdeg\right) \tag{3.3.43}$$

The constants required for this model are shown in table 4.

Name	Meaning	Size	Source
k_{silw}	Present day silicate weathering rate	6.65×10^{12} mol C yr^{-1}	For steady state
k_{carbw}	Present day carbonate weathering rate	13.35×10^{12} mol C yr^{-1}	GEOCARB,COPSE
k_{oxidw}	Present day oxidative weathering rate	7.75×10^{12} mol C yr^{-1}	For steady state
k_{phosw}	Present day nutrient (P) weathering rate*	4.35×10^{10} mol P yr^{-1}	For steady state
k_{pyrw}	Present day pyrite sulphur weathering rate	0.45×10^{12} mol S yr^{-1}	GEOCARB
k_{gypw}	Present day gypsum sulphur weathering rate	2×10^{12} mol S yr^{-1}	GEOCARB
k_{ocdeg}	Present day organic carbon degassing rate	1.25×10^{12} mol C yr^{-1}	GEOCARB, COPSE
k_{ccdeg}	Present day carbonate carbon degassing rate	6.65×10^{12} mol C yr^{-1}	GEOCARB, COPSE
k_{pyrdeg}	Present day pyrite sulphur degassing rate	0.25×10^{12} mol S yr^{-1}	GEOCARB
k_{gypdeg}	Present day gypsum sulphur degassing rate	0.5×10^{12} mol S yr^{-1}	GEOCARB
k_{mocb}	Present day marine organic carbon burial rate*	4.5×10^{12} mol C yr^{-1}	COPSE
k_{locb}	Present day land organic carbon burial rate*	4.5×10^{12} mol C yr^{-1}	COPSE
k_{mpsb}	Present day pyrite sulphur burial rate	0.7×10^{12} mol S yr^{-1}	For steady state
k_{mgsb}	Present day gypsum sulphur burial rate	2.5×10^{12} mol S yr^{-1}	For steady state
k_{mopb}	Present day marine organic phosphate burial*	1.8×10^{10} mol P yr^{-1}	COPSE
k_{capb}	Present day Ca-associated phosphate burial*	1.5×10^{10} mol P yr^{-1}	COPSE
k_{fepb}	Present day Fe-associated phosphate burial*	6×10^{9} mol P yr^{-1}	COPSE

Table 4: List of Minimal Model constants with sources, *denotes constants required for nutrient model only.
For the isotope mass balance model $k_{mocb} = 5.5 \times 10^{12}$ mol C yr^{-1}, $k_{locb} = 0$.

3.4 Validation against COPSE and GEOCARB models

The Minimal Model is now run through the Phanerozoic, with burial of reduced species either following the ocean nutrient model of COPSE, or the isotope mass balance model of GEOCARB. Results are plotted against the COPSE and GEOCARB runs, and are shown in figure 3.4.4. Following the original models, the assumed weathering enhancement due to vascular plant colonisation (k_{vp}) is set at 7 for comparisons to COPSE, and at 4 for comparisons to GEOCARB. For the COPSE runs, oxidative weathering is allowed a dependence on oxygen concentration (Lasaga and Ohmoto, 2002), for the GEOCARB runs this is removed, following the original model set up.

When the simplified nutrient system is included, agreement with the COPSE model predictions for Phanerozoic CO_2 and O_2 are very strong (panel **a,b**). This is expected due to the degree of similarity between the Minimal Model and the COPSE system - the only major omission from the full COPSE model is the nitrate nutrient system, shown here to have minimal effect on model results.

Allowing burial rates of reduced species to be calculated via an isotope mass balance model gives results for oxygen that are very close to the predictions of GEOCARBSULFvolc (Berner, 2009) (panel **c,d**). Differences arise because the Minimal Model does not include rapid recycling, or many of the abiotic forcings described in the full model. With the removal of some negative feedback on oxygen, we would expect O_2 predictions to peak at higher values around 300Ma, however the removal of abiotic forcings acts to diminish this peak (see fig 17 of Berner (2006a)), cancelling the effect. Carbon dioxide predictions in the Minimal Model follow the shape of the full GEOCARB model, but variation around long term steady state is reduced due to the smaller abiotic forcing set.

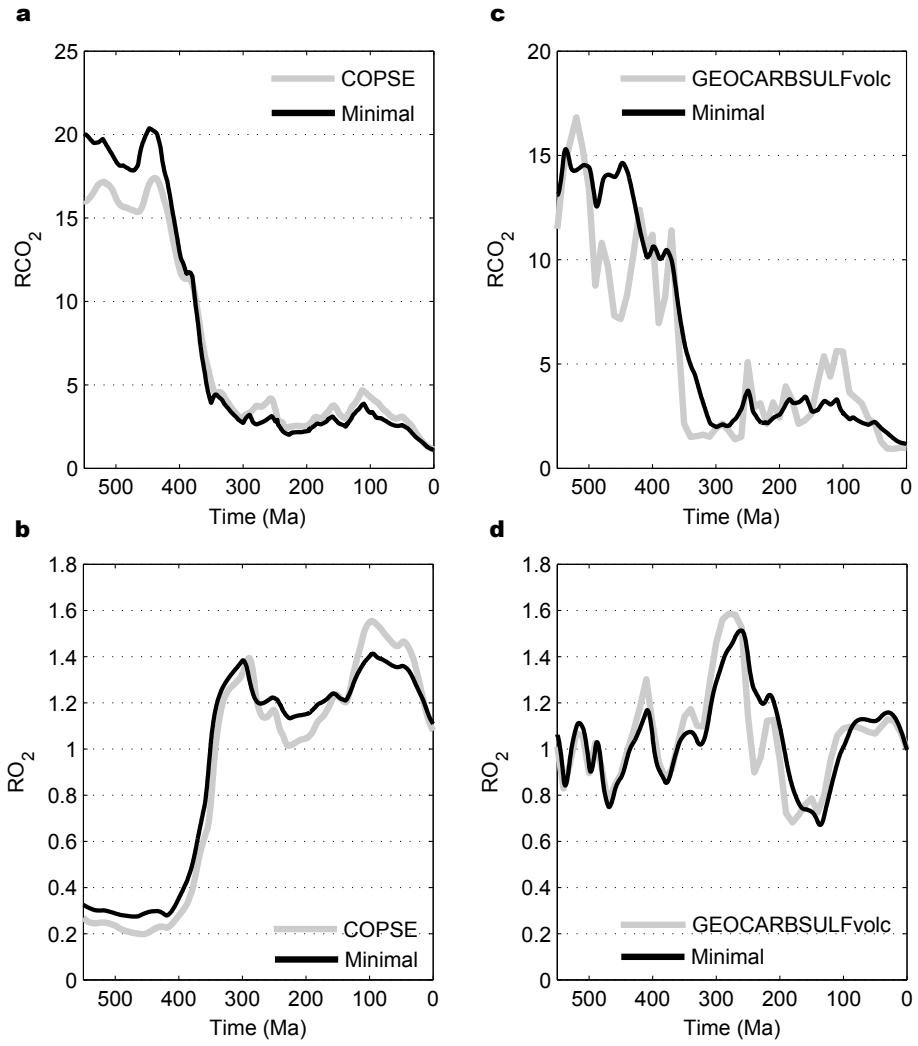

Figure 3.4.4: Minimal Model run for the Phanerozoic (black lines), plotted against previous model output (grey). a,b, Burial of organic carbon and pyrite sulphur controlled by nutrient system, plotted against COPSE model. **c,d,** Burial of organic carbon and pyrite sulphur controlled by isotope mass balance, plotted against GEOCARBSULFvolc.

It can be concluded that the Minimal Model includes the key processes that control current predictions of O_2 and CO_2 concentration over the Phanerozoic, whilst representing a simplification over the models it is based on. A useful feature of the model is its high modularity - the timeframe, forcings and flux calculations can be interchanged easily, and new reservoirs and fluxes can be added. The Minimal Model is also significantly more robust than the original systems, and utilises the MATLAB inbuilt variable timestep solvers

for 'stiff' ODE systems (i.e. where the timescale for alteration varies significantly between variables) (Shampine and Reichelt, 1997; Shampine et al., 2003). These numerical schemes alter the size of the model timestep depending on the rate of change of the model reservoirs, minimising computational error and preventing model crashes when values are very far from steady state. The GEOCARB/COPSE model framework can now be easily applied to the Precambrian.

3.5 Minimal Model predictions for Proterozoic climate

3.5.1 Extension of forcings

The model forcing set is now extended back in time to 1000Ma using available proxy data. In previous models, the global metamorphic/degassing rate is assumed to be proportional the sea floor spreading rate, which has been estimated over the Phanerozoic via sea level inversion (Gaffin, 1987). For the Precambrian, lack of available data means the spreading rate must be estimated based on models for the thermal history of the Earth. Following Franck and Bounama (1997); Franck et al. (1999) the spreading rate, S, can be written as:

$$S = \frac{Q^2 \pi \kappa A_{ocean}(t)}{4k^2 \left(T_m - T_s\right)^2} \tag{3.5.1}$$

where Q is the mantle heat flow, κ is the thermal diffusivity, $A_{ocean}(t)$ is the area of ocean basins at time t, k is the thermal conductivity, T_m and T_s are the average mantle and surface temperatures respectively. Allowing $T_m - T_s \approx T_m$ and combining constants this becomes:

$$S = k_{sr} \frac{Q^2 A_{ocean}(t)}{T_m^2} \tag{3.5.2}$$

where $k_{sr} = \frac{\kappa\pi}{4k^2}$. Changes in mantle average temperature and ocean basin area over Earth history act to cancel each other out, and are smaller than the relative change in heat flow, allowing simplification to:

$$S_{\text{relative}} = \left(\frac{Q}{Q_0}\right)^2 \tag{3.5.3}$$

here S_{relative} is the relative spreading rate and $\frac{Q}{Q_0}$ is the relative heat flow.

Figure 3.5.5**a** shows the relative spreading rate calculated from equation 3.5.3 using the mantle high temperature heat flux estimations from Lowell and Keller (2003). Also shown is the spreading rate calculated from equation 3.5.2 using the same heat flux. Here A_{ocean} is calculated from the relative continental area estimate of McLennan and Taylor (1983), which is used to calculate the heat flux in Lowell and Keller (2003), and conveniently lies towards the average of the many estimates for continental growth (Rino et al., 2004; Fyfe, 1978; Hurley and Rand, 1969; Condie, 1998). Mantle average temperature is taken from Franck and Bounama (1997), assuming a 3000K average temperature at 4.5Ga. As the difference between the two treatments is minimal, the simpler equation 3.5.3 is adopted for the model.

The rate of tectonic uplift in the parent models is estimated via strontium isotope mass balance (Berner, 1994), and extended here using the normalised seawater $\frac{^{87}Sr}{^{86}Sr}$ curve of Shields (2007) as a rough estimate of the relative material influx to the ocean from terrestrial weathering. The Phanerozoic uplift and degassing forcings are shown against the extended forcings in figure 3.5.5. Note that the long term curves used to extend the forcings show good general agreement with Phanerozoic proxies (shown in figure 3.5.5**b,c**).

The isotope mass balance method for inferring organic burial requires knowledge of the isotopic fractionation of sedimentary carbonates and sulphates for the timeframe of interest. The isotope records used in GEOCARB are extended using data from Halverson et al. (2005) for $\delta^{13}C$, and data from Canfield (2005) for $\delta^{34}S$, these are shown in figure 3.5.5**e,f**. The isotope mass balance system does not support large negative carbon isotope fractionation, which causes the system to predict negative burial rates. The maximum negative fractionation for carbon is therefore restricted to -3‰ for the model forcing. The evolutionary forcings required for the nutrient system require no extension as they have no effect before the point at which the given process evolves.

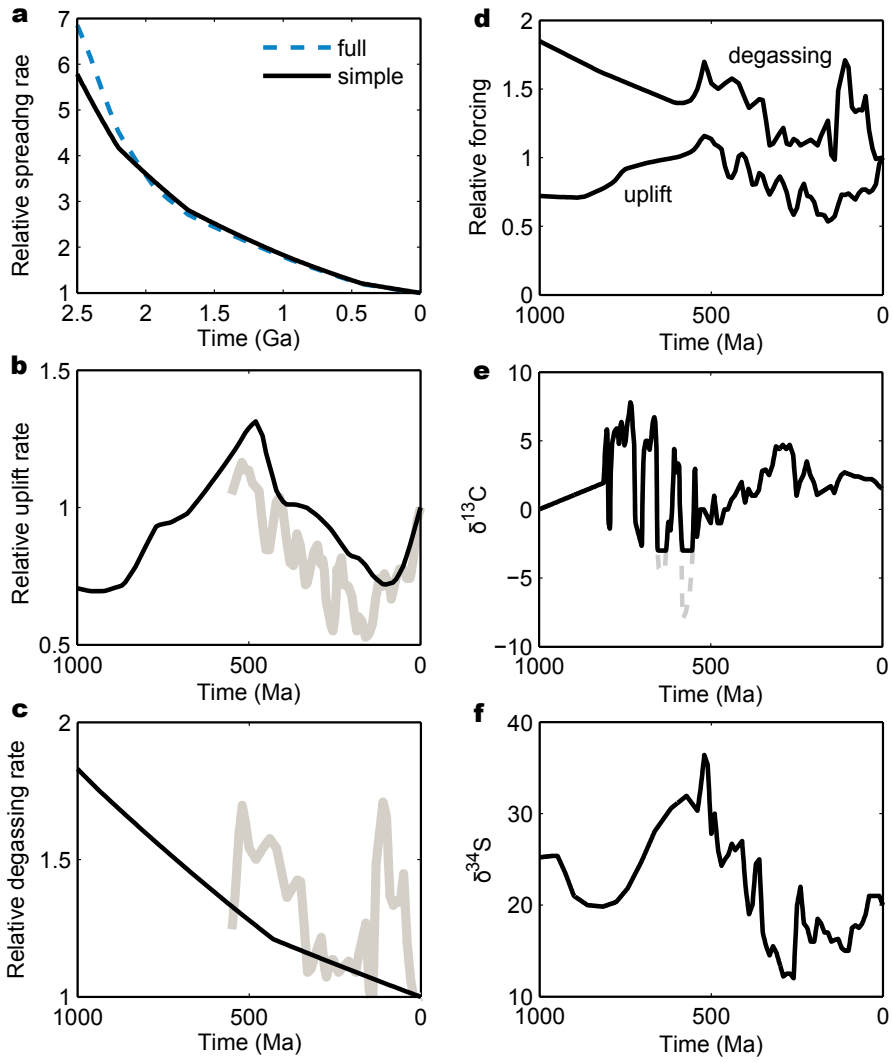

Figure 3.5.5: Forcing extensions for the Precambrian. a, Relative spreading rate calculated from equation 3.5.2 (blue) and equation 3.5.3 (black). **b,** Grey line shows uplift forcing from COPSE and GEOCARB models, black line shows normalised seawater strontium curve from Shields (2007). **c,** Degassing forcing used in COPSE and GEOCARB models shown as grey line, black line shows the spreading rate from Franck et al. (1999). **d,** Resulting extended forcings. **e,** δ^{13}C record used in GEOCARB, extended into the Precambrian with data from Halverson et al. (2005). Grey dashed line shows large negative excursions as reported in the literature, black line shows an artificial limitation of negative excursions to -3‰. **b,** δ^{34}S forcing used in GEOCARB, extended with data from Canfield (2005). Original in colour.

3.5.2 Baseline predictions

Figure 3.5.6 shows model output when subject to the new forcing set and run for the period 1000-0Ma, these are plotted from 900-0Ma to allow for model spinup. The model is run with either the nutrient system from COPSE (panel **a-c**) or the isotope system from GEOCARB (panel **e-g**) used to infer organic burial rates. Note that the Phanerozoic predictions are not noticeably altered by the increased model timeframe.

The high expected rate of degassing in the Precambrian allows more CO_2 to build up in the atmosphere. This acts to increase global temperature and therefore the silicate weathering flux, balancing the system in the long term. Lower solar luminosity and a reduced global uplift rate in the Neoproterozoic act to limit the silicate weathering process, increasing the CO_2 requirement for system stability. Both burial systems predict a gradual drop in CO_2 concentration from $\sim$30PAL at 900Ma to $\sim$15PAL in the late Neoproterozoic. This is consistently higher than the 1-10PAL inferred form carbon isotope modelling (Kah and Bartley, 2004), and the associated temperatures predicted by the model do not correlate well with expected severe glaciation in the late Neoproterozoic. When the isotope system is used to predict organic burial, predictions for CO_2 show variation around the results for the nutrient system. This is due to productivity spikes that follow the carbon isotope record. Carbon dioxide concentration is increased during the glacial negative excursions of the Neoproterozoic due to assumed lower carbon burial, and lowered during the positive excursions during the long 'interglacial' periods, from which high burial is inferred.

Both models show oxygen concentration in the Neoproterozoic reaching higher levels than in the Early Phanerozoic. For the nutrient system, this is due to the assumed higher rate of degassing, which results in a higher rate of continental weathering for system stability. Nutrient delivery from weathering is increased, allowing for a greater rate of burial of organic carbon. As with isotope mass balance models for the Phanerozoic (Berner, 1987), predicted oxygen concentration closely follows the isotopic record of carbon when the isotope system is used. This results in extremely high O_2 predictions that correlate with the large positive C isotope excursions in the Neoproterozoic. Both model predictions for oxygen can be effectively falsified

by the available proxy data, $O_2 > 0.5$PAL at 900Ma is very difficult to reconcile with an anoxic deep ocean, which is suggested by many independent proxies (Canfield et al., 2008; Frei et al., 2009).

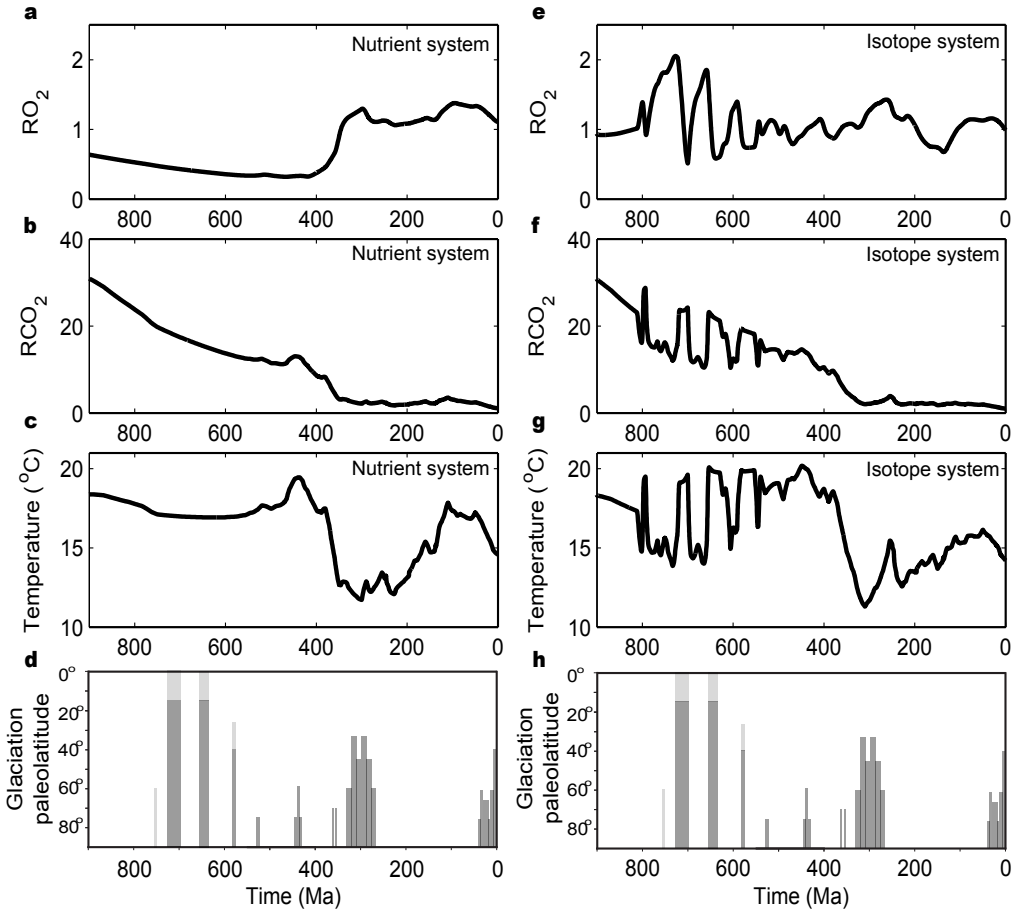

Figure 3.5.6: Minimal Model run for the period 900-0Ma, using COPSE nutrient system (a-c) or GEOCARB isotope mass balance method (e-g) to approximate organic burial. Results shown for relative atmospheric oxygen and carbon dioxide, and average surface temperature. Glaciation paleolatitude (**d**,**h**) shown in each column for comparison.

The conclusion from this preliminary analysis is that the methods used to model oxygen concentration in the Phanerozoic do not produce sensible predictions when extended further back in time. In both model systems, oxygen concentration is tightly coupled to the organic carbon burial rate, which may be reasonable for the Phanerozoic but may not have been the case in earlier Earth history. Modelling the Neoproterozoic oxygen cycle likely

requires additional processes to be considered, with more emphasis on the sinks for oxygen, such as the input of reduced material from the mantle (e.g. Holland (2009)). The results for CO_2 and temperature presented here are however somewhat encouraging. Omitting the isotope forcings, an average temperature of $\sim 17°C$ is predicted over the Neoproterozoic glacial series. Holding oxygen concentration fixed in model runs may therefore allow some evaluation of the Neoproterozoic carbon cycle. The next section explores additional model forcings that may permit the low CO_2 concentration and global temperature suggested by the glacial record.

3.6 Weathering enhancement and temperature in the Neoproterozoic

3.6.1 Continental position, dispersion and composition

Figure 3.6.7 shows a reconstruction of the position of the continents in the late Neoproterozoic (Li et al., 2008). It can be seen that continents are grouped at low latitudes for the period 750-630Ma, drifting to higher latitudes by 600Ma. Higher surface temperature near the equator should allow for more vigorous reaction kinetics, as well as an increase in humidity and therefore runoff rate (Donnadieu et al., 2004). Both of these factors would be expected to enhance the silicate weathering rate (Berner, 1994), allowing for lower global temperature at steady state. The relationship between temperature and runoff is complex and depends on the precipitation and evaporation rates and therefore the size and distribution of the continents, not simply their position. There is only a weak relationship, if any between Phanerozoic continental mean latitude and runoff rate (Otto-Bliesner, 1995). For runoff rate to increase there must be adequate sources of moisture, therefore the dispersal of the continents is a very important consideration. It has been estimated using a coupled climate-geochemical model that the breakup of the supercontinent Rodinia into smaller, dispersed continents between 800-700Ma may have caused a two fold increase in mid latitude runoff, increasing the weathering rate until the system is balanced by a decrease in CO_2 concentration (Donnadieu et al., 2004).

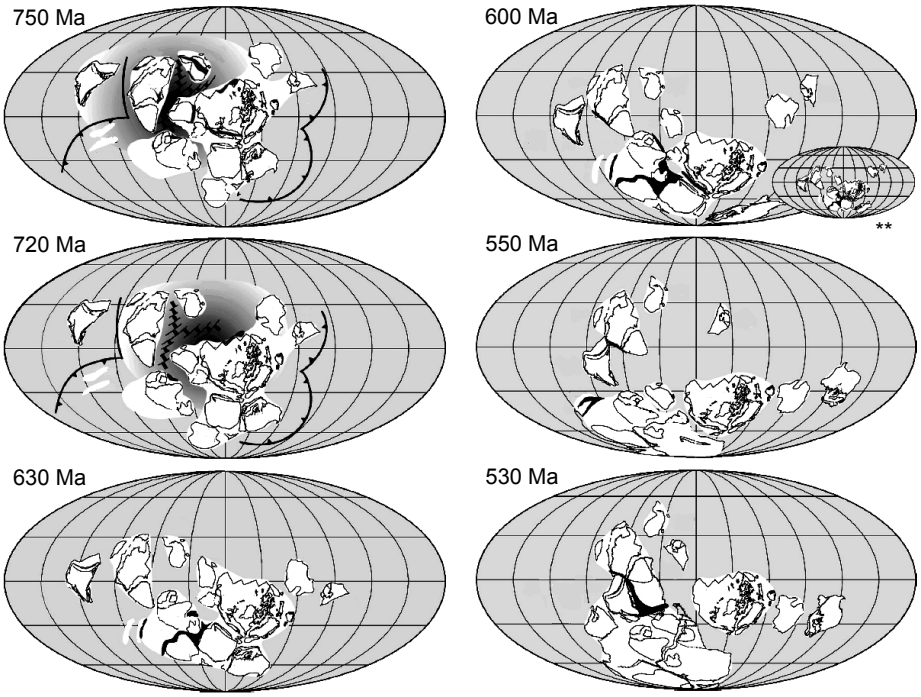

Figure 3.6.7: Continental positions throughout the late Neoproterozoic. Figure modified from Li et al. (2008). Dark shaded area shows mantle superplume, ** shows option of Laurentia at low latitude, see ref (Li et al., 2008) for a more detailed picture.

Another factor influencing the silicate weathering rate is the composition of the continents. Weathering of basaltic areas leads to river water with molar ratios of calcium and magnesium that are higher than for typical silicates. Currently around 8.4% of the global silicate area is basaltic, but this area accounts for $> 30\%$ of the silicate weathering flux (Dessert et al., 2003). Large basaltic provinces appear in equatorial positions at around 800Ma, and have been linked to the onset of the Sturtian glaciation via enhanced continental weathering (Godderis et al., 2003). It is also possible that increased organic burial due to the opening of new continental margins in the Neoproterozoic caused a decline in CO_2 and therefore radiative forcing (Hoffman et al., 1998), a higher rate of organic burial is implied by the carbon isotope record, which shows positive fractionation for much of the period (Halverson et al., 2005).

The combination of dispersed, low latitude continents and an increase in basaltic surface area in the late Neoproterozoic could constitute a significant enhancement of the global silicate weathering rate. As with the weathering enhancement due to vascular plants, evaluation of the magnitude of the continental enhancement at a global scale is extremely difficult. Assuming a 2°C mean surface temperature anomaly between the high latitudes and equatorial regions (Hansen et al., 2006) and following the kinetic rate equation of Berner (1994) yields a 25% increase in the weathering rate. Assuming the majority of continents reside in the tropics could also add a maximum ∼2 fold enhancement to this due to increased runoff (Donnadieu et al., 2004). A major uncertainty is the area and position of basaltic rock, as it is responsible for such a large amount of the total weathering flux. Following Godderis et al. (2003), an 8-fold enhancement in the weathering of basalts over granitic provinces is assumed. Allowing this increase for an area of 6×10^6km (Godderis et al., 2003), or 4% of the continental area, produces a global weathering rate enhancement of $\sim 30\%$. Taking the factors of continental paleolatitude, dispersion and composition into consideration, and assuming a simplistic multiplicitive relationship, it is perhaps possible that the degree of abiotic weathering enhancement in the late Neoproterozoic may have been up to 3-fold ($1.25 \times 1.3 \times 2 = 3.25$).

3.6.2 Weathering enhancement prior to vascular plant evolution

The assumed enhancement of global weathering by vascular plants at around 400Ma implies that reaction kinetics were less influenced by global temperature before this time (i.e. throughout the Precambrian), requiring a much higher surface temperature to balance the carbon cycle (see figure 3a in Sleep and Zahnle (2001)). This leads to the high temperature predictions for the early Phanerozoic in current carbon cycle models (Berner, 2006a; Bergman et al., 2004; Arvidson et al., 2006). Taking this view, a significant enhancement of global weathering is required in the Neoproterozoic to cause the apparent low temperature. However it is likely that the current assumed global weathering enhancement associated with the evolution of vascular plants (around 4-fold (Berner, 2006a)) is excessive. Although this degree of enhancement has been measured in well designed field studies (see Moul-

ton and Berner (1996); Bormann et al. (1987); Berner (1998)), it is unlikely that this enhancement would have been realised globally. Mountainous areas with high relief and erosion rates do not permit formation of stable soils, and are not suited to deep-rooted plants, however it is these areas that supply a large fraction of the present day silicate weathering flux (Gaillardet et al., 1999). Also in many continental cratons and areas where erosion is slow, the silicate weathering rate is limited by transport of material, not by the reaction kinetics (West et al., 2005; Millot et al., 2002), meaning that absence of higher plants from these areas may not necessarily change the weathering dynamics. Further to this, it is also possible that the long term weathering enhancement from vascular plants is less significant than the short term enhancements measured in field studies.

3.6.3 Model results for Neoproterozoic temperature

To demonstrate the effects of the above observations on Neoproterozoic climate, the Minimal Model is now run the period 900-400Ma with oxygen concentration fixed at 0.01atm. The nutrient system is used to calculate productivity so that the model has greater predictive power (i.e. carbon burial is not imposed but calculated from the other parameters). An additional enhancement of silicate and carbonate weathering (k_{cf}) is imposed for the period 750-600Ma, reflecting the effect of continental position, increased basaltic area and supercontinent dispersion occurring over this time (Li et al., 2008; Donnadieu et al., 2004). Figure 3.6.8 shows both a 3-fold and 2-fold enhancement (solid and dashed lines respectively) alongside the default run with no enhancement (dotted lines). The black curves show the proposed 4-fold vascular plant enhancement, the grey lines show a more conservative 2-fold enhancement following the reasoning above.

The effect of imposing low oxygen in the model is a reduction in the weathering rate of buried organic carbon, which is a major CO_2 source. This leads to lower CO_2 and temperature predictions some $1-2^{\circ}$C lower than those of the full system for the late Neoproterozoic. Still, the maximum conceivable weathering enhancement is required to push global temperature to the theoretical snowball trigger ($\sim 10^{\circ}$C (Hoffman and Schrag, 2002)) when $k_{\mathrm{vp}} = 4$.

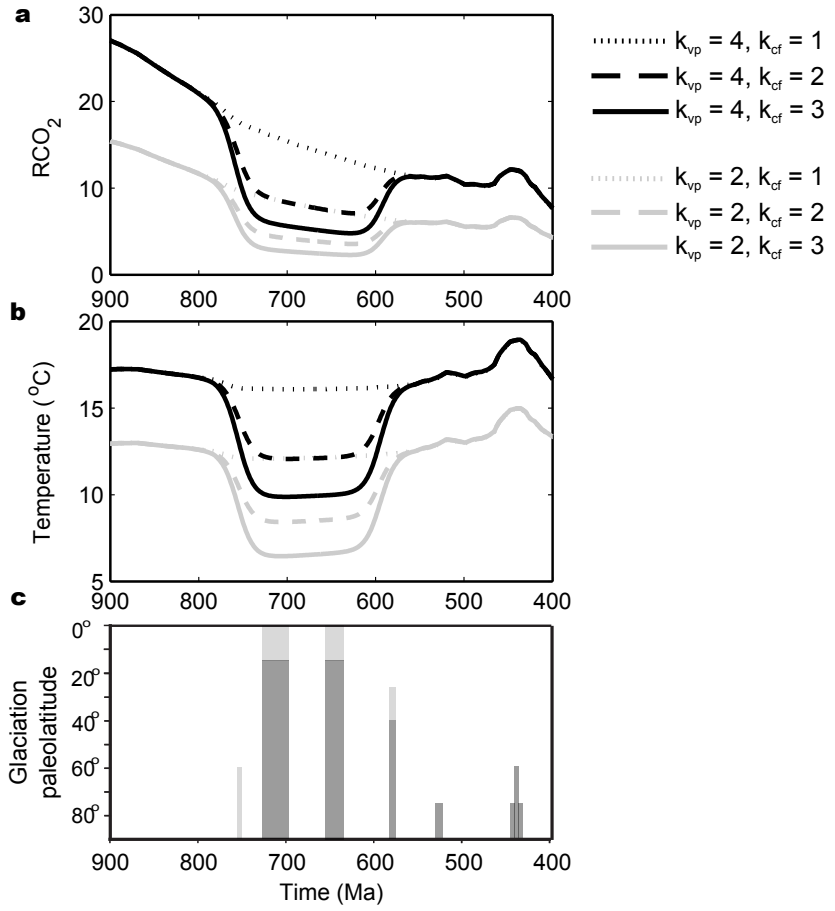

Figure 3.6.8: Model CO_2 and temperature for the period 900-0Ma. Here the nutrient model is used to estimate burial of reduced species, but oxygen is not calculated. Use of isotope mass balance model would yield similar results, but with CO_2 fluctuating in the Neoproterozoic, following the isotope record. **a,** Relative atmosphere/ocean CO_2 concentration. **b,** Model temperature. **c,** Glacial paleolatitude as in figure 3.2.1. Black lines show 4-fold vascular plant weathering enhancement at 400Ma, grey lines show 2-fold enhancement. Dashed lines show a 2-fold weathering enhancement from 750-600Ma, solid lines show a 3-fold enhancement.

If a 2-fold enhancement of continental weathering rates is assumed at 400Ma, the enhancement required for deep glaciation is relatively small - here a 2-fold increase in weatherability in the late Neoproterozoic results in sustained average global surface temperature below the hypothesised snowball trigger. In this case early Phanerozoic global temperature remains below 15°C, permitting glaciations in the Cambrian and Ordovician. However, rising oxygen concentration around 580Ma and the expected increase in CO_2

release from weathering of buried organic carbon is not included here, and would act to increase both CO_2 and temperature estimates.

3.7 Chapter conclusions

Simplification and extension of current Phanerozoic Earth system modelling techniques allows for reasonable predictions for CO_2 and temperature over the last 900Myr. As with the Phanerozoic results, these predictions rely heavily on external forcings. As noted by other authors (Godderis et al., 2003; Donnadieu et al., 2004), a combination of continental position at low latitudes, tendency towards smaller and dispersed continents, and a large area of basaltic rock in the late Neoproterozoic may provide sufficient enhancement of the weathering process to allow for the low temperatures required for global glaciation.

The extreme enhancement of silicate weathering associated with the evolution of vascular plants causes problems when attempting to reconcile atmospheric composition and climate during the Neoproterozoic. The predicted high CO_2 concentration before vascular plant evolution requires a massive reduction in radiative forcing to produce conditions which could be expected to trigger the low latitude 'snowball' glaciations at $\sim$ 730Ma and $\sim$ 650Ma. Reducing global temperature sufficiently via CO_2 drawdown requires a 3-fold enhancement of the silicate weathering flux, which is towards the maximum estimate from a combination of proposed climatic forcings. However, it is likely that the assumed degree of enhancement of the weathering process due to vascular plant evolution may be overestimated, which would relax considerably the required continental forcing.

The methods employed by Phanerozoic biogeochenical models COPSE and GEOCARB for estimating atmospheric oxygen concentration do not give sensible results when extended into the Neoproterozoic. It is also very difficult to test if the current Phanerozoic predictions are correct. It is therefore likely that a significant long term process is missing from the aforementioned models.

Unknown quantities of greenhouse gases other than CO_2 are a major limitation of the method explored here. It is likely that a higher concentration of methane would have been present in the more reducing Proterozoic atmo-

sphere (Pavlov et al., 2003), meaning that a greater reduction in CO_2 would be required to initiate global glaciation.

Previous assessments of Neoproterozoic conditions using a coupled climate-geochemical model have shown that sufficiently low global temperature for snowball glaciations is possible given the likely paleogeographical forcings (Donnadieu et al., 2004; Godderis et al., 2003). The model used by these authors allows for a global degassing rate of $\pm 20\%$ present day rate. The results in this chapter suggest that glaciation is still possible when a higher degassing rate is used (the spreading rate approximation yields around a 50% increase in degassing during the Neoproterozoic). The work here also considers the effects of paleouplift rate, and absence of climatically important biota such as vascular plants and calcareous plankton (Volk, 1989).

These results constrain the long-term ($> 10^6$yr) steady state temperature, and do not consider system changes occuring on smaller timescales. Steady state temperature $< 10°$C is not a solid prerequisite for low-latitude glaciation, and it has been shown for example that severe and long-lasting glaciation may instead be the result of amplification of an initial perturbation via feedback on sea level change and related shifts in depositional environments (Ridgwell et al., 2003). This mechanism does not require steady state temperature and CO_2 concentration in the Neoproterozoic to be exceptionally low.

4 Neoproterozoic snowball glaciations and limitations on global weathering rates

4.1 Introduction

A Neoproterozoic 'cold period', as described in the previous chapter, does not explain the apparently periodic sequence of extreme glaciations seen in the geological record (Halverson et al., 2010). Following both multimillion year glaciations is a ∼50Myr interglacial period, far longer than the assumed timescale on which the carbon cycle is stable (∼ 1Myr). The late Neoproterozoic also sees dramatic positive and negative excursions in carbonate $\delta^{13}C$ (Halverson et al., 2005; Macdonald et al., 2010). Both the cause and global applicability of these excursions has been questioned, with authors suggesting either diagenesis (Derry, 2010) or the oxidation of a large organic carbon reservoir as a solution (Rothman et al., 2003), however recent data shows co-variance between the fractionation in organic carbon and in carbonate carbon, indicating that the signal may indeed be both primary and globally significant (Johnston et al., 2012).

To analyse the finer scale dynamics of the Neoproterozoic carbon cycle, a simple ice-albedo feedback was added to the Minimal Model, allowing a 'flip' to high albedo when global average temperature falls below 10°C to imitate the proposed snowball Earth scenario (Hoffman and Schrag, 2002). Extremely rapid weathering in the aftermath of model snowball glaciations prompted investigation into the limiting factors for this process. It was found that given likely tectonic limitation of the maximum global weathering rate, the time taken to bury the CO_2 added to the atmosphere/ocean during glaciation is similar to the duration of the interglacial periods, providing a possible explanation for the oscillatory nature of these events. This would allow for the observed pattern of extreme glaciations under a single, long-term cooling forcing, which may be attributed to the paleogeographical changes in the Neoproterozoic (Li et al., 2008). After discussion with my supervisors and Richard Boyle (who has previously worked on mechanisms for understanding the gaps between Neoproterozoic glaciations (Boyle, 2008)), a letter documenting the work was submitted to the journal Nature Geoscience and is published as B. Mills et al., 'Timing of Neoproterozoic glaciations linked to

transport-limited global weathering' *Nature Geoscience* **4,** 861 (2011).

The Minimal Model is further simplified for this work in order to convey the idea as clearly as possible. The published letter is reproduced below, followed by supplementary information detailing the model derivation and some extension of the work. Unfortunately some restatement of the ideas and terms used previously is unavoidable, but this is kept to a minimum. A complimentary 'feature' article explaining the mechanism and some of the wider implications was written for the same issue by Joshua West (West, 2011).

4.2 Timing of Neoproterozoic glaciations linked to transport-limited global weathering

The Earth underwent several snowball glaciations between 1,000 and 541 Myr ago. The termination of these glaciations is thought to have been triggered by the accumulation of volcanic CO_2 in the atmosphere over millions of years (Hoffman et al., 1998; Pierrehumbert, 2005). Subsequent high temperatures and loss of continental ice would increase silicate weathering and in turn draw down atmospheric CO_2 (Walker et al., 1981). Estimates of the post-snowball weathering rate indicate that equilibrium between CO_2 input and removal would be restored within several million years (Le Hir et al., 2009), triggering a new glaciation. However the transition between deglaciation and the onset a new glaciation was on the order of 10^7 years.

Over long timescales, the availability of fresh rock can become a limiting factor for silicate weathering rates (West et al., 2005). Here we show that when this limitation is incorporated into the COPSE biogeochemical model (Bergman et al., 2004), the stabilization time is substantially higher, $> 10^7$ years. When we include a simple ice albedo feedback, the model produces greenhouse-icehouse oscillations on this timescale that are compatible with observations. Our simulations also indicate positive carbon isotope excursions and an increased flux of oxygen to the atmosphere during interglacials, both of which are consistent with the geological record (Halverson et al., 2005; Canfield et al., 2008). We conclude that the long gaps between snowball glaciations can be explained by limitations on silicate weathering rates.

The Neoproterozoic era (1000-541Ma) is punctuated by at least three glaciations (Hoffmann et al., 2004), the severe low-latitude Sturtian and Marinoan episodes being proposed as examples of 'Snowball Earth' events (Hoffman et al., 1998; Kirschvink, 1992). Figure 4.2.1 displays Neoproterozoic carbonate carbon isotope data (Halverson et al., 2005), which shows a quasi-periodic pattern. Negative excursions associated with glaciation appear at 50 Myr intervals between long periods of positive fractionation. The long interval between glaciations poses a puzzle given the standard model of a snowball Earth being terminated by very high CO_2 and temperature. The time taken to restore equilibrium after such a perturbation depends on the rate of CO_2 drawdown via silicate weathering, a process that would be greatly enhanced in the aftermath of snowball Earth. Highly weatherable rock flour produced by glacial grinding would likely cover a large surface area, and increased temperature and runoff should allow for an elevated weathering flux. Linked GCM and kinetic weathering models have determined the maximum weathering rate in this climate to be on the order of 10 times the modern day flux, implying a timescale of around 10^6 years to reduce atmospheric CO_2 to pre-glacial levels (Le Hir et al., 2009). Based on these results, we would expect the system to establish equilibrium in a time far shorter than the interglacial periods following the Sturtian and Marinoan glaciations.

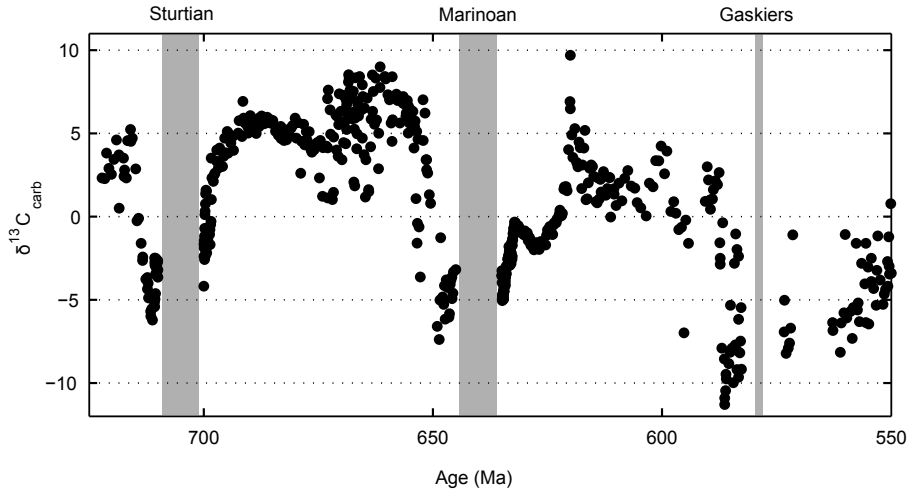

Figure 4.2.1: δ^{13}C record for the late Neoproterozoic. Isotopic composition of carbonates from Halverson et al. (2005). The vertical grey bars from left to right denote the Sturtian, Marinoan and Gaskiers glaciations.

Here we propose that the timescale for CO_2 drawdown following a snowball glaciation should be extended due to transport limitation of the silicate weathering process. In a transport limited regime, silicate cations are completely leached from fresh regolith and therefore the rate of chemical weathering depends only on the physical erosion rate (West et al., 2005). Modern continental cratons are transport limited, as seen by plotting the rate of denudation of silicate cations against total denudation rate (Millot et al., 2002). In such a regime, increasing temperature or runoff does not increase the rate of CO_2 drawdown, because all the available silicate cations are already being processed. As global temperature and humidity rises, we would expect more weathering zones to become transport-limited, implying a theoretical maximum silicate weathering rate, where every available cation is leached.

Over the Phanerozoic, the mean continental erosion rate is estimated to be $\sim$ 16m Myr^{-1} (Wilkinson and McElroy, 2007). Using the average density and area of the present day continents (area=1.5×10^{14} m^2, density = 2.5×10^3 kg m^{-3}) yields a total mass of 6×10^{12} kg yr^{-1}. Assuming a cation weight fraction of 0.08 (West et al., 2005), we estimate a global silicate weathering rate maximum for the Phanerozoic of around 4.8×10^{11} kg yr^{-1}. This maximum transport limited rate is about 2.4 times greater than the present day weathering rate (Gaillardet et al., 1999).

Determining the global erosion rate in the Neoproterozoic is difficult, because it depends on the continental area and rate of uplift. Current estimates for Neoproterozoic uplift rates are close to present day values (Rino et al., 2004), and the majority of studies agree that the total continental area was probably less than it is now. Proxies for global denudation show very low values ($<$ 10m Myr^{-1}) for the early Phanerozoic, but are likely to be affected by sampling artefacts (Willenbring and Blanckenburg, 2010). The rate of volcanic degassing in the Neoproterozoic is also important, as it is the balance between CO_2 degassing and its consumption rate via weathering and burial that dictates the system response time to large perturbations.

In carbon cycle models, degassing is usually assumed to be proportional to the seafloor spreading rate. Accounting for different continental growth models, the Neoproterozoic outgassing rate was probably between 1 and 5 times the present day rate (Rino et al., 2004; Franck and Bounama, 1997). But smaller crustal carbon content in the Neoproterozoic (Hayes and Waldbauer, 2006) may have decreased the CO_2 content of volcanic gas by up to 20%.

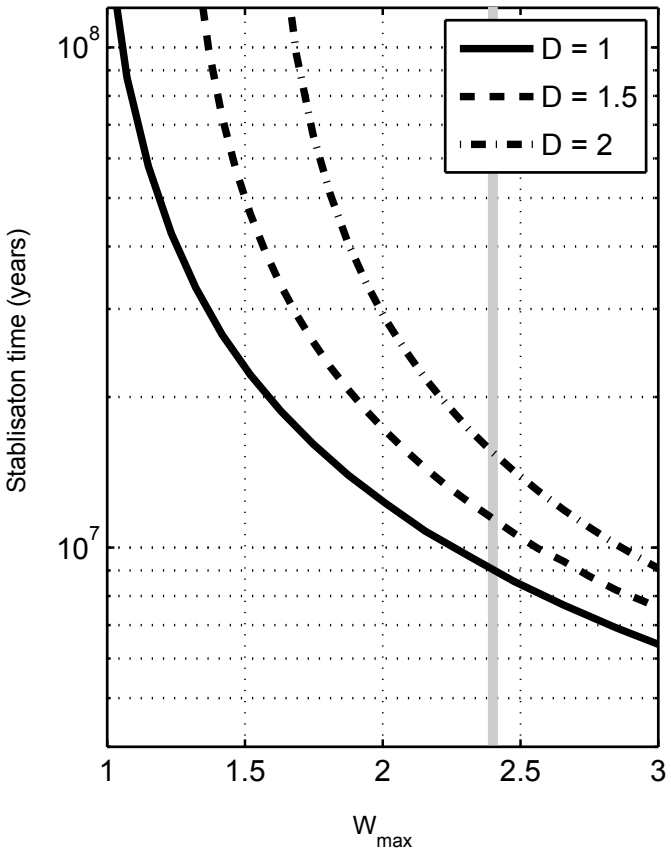

Figure 4.2.2: Phase portrait: stabilisation time versus maximum weathering rate, W_{max}. Here we assume an initial CO_2 concentration of 0.3 atmospheres, and fix the global weathering rate at W_{max}. The three lines show different choices of the relative CO_2 degassing rate, D. W_{max} is defined relative to present day silicate weathering rate, with the grey vertical line showing our estimate of W_{max}= 2.4 for the Phanerozoic. Increasing the weathering rate enhances nutrient delivery and therefore increases the organic burial fraction, allowing stability when W_{max} is somewhat smaller than D, providing $W_{max} > 1$. See supplementary information for full model description.

In figure 4.2.2, we use a modified version of the COPSE biogeochemical model (Bergman et al., 2004) (see supplementary information) to investigate the effect of a weathering rate cap on the time taken to return to steady state after the suggested snowball exit concentration of 0.3 atm CO_2 (Hoffman et al., 1998; Pierrehumbert, 2005) is imposed. The global silicate weathering rate is fixed at a prescribed maximum value, W_{max}, which is defined relative to the present day rate. We find that choice of W_{max} has a strong effect on the system: Assuming the Phanerozoic average erosion rate (W_{max}=2.4) yields a stabilisation time of $\sim 10^7$ years, even for conservative estimates of the CO_2 degassing rate D. A lower erosion rate, and/or a higher degassing rate increases the stabilisation time greatly. For further model runs we let global weathering follow a simple kinetic equation as described by Berner (1994), but asymptote to W_{max} as the kinetic weathering rate approaches the transport-limited value, placing a cap on global weathering rates. The choice of kinetic weathering function, and the nature of the transition to W_{max} has negligible effect on results as the rate remains at W_{max} until CO_2 is very close to the stable level.

An important consideration for this work is weathering of rock flour left on the surface after a snowball glaciation, which would be expected to increase weathering kinetics as in the quaternary glacial cycle (Vance et al., 2009). Global weathering fluxes would not become limited by transport of fresh rock until the flour produced during the glaciation had been completely leached. Le Hir et al. (2009) assume a thin soil profile following a snowball event, due to evidence of persistent weathering during glaciation (Donnadieu et al., 2003). Following their estimate of a 25cm reactive upper layer, we derive a weatherable equivalent of $\sim 10^{17}$ moles C (see supplementary information).

Figure 4.2.3 shows model sensitivity to the initial quantity of rock flour. Here we allow a global weathering rate of 10 times present day when rock flour is present (Le Hir et al., 2009), switching to the transport limited equation once a specified amount of carbon has been buried, analogous to the abundance of glacial flour. We find that a weatherable equivalent on the order of 10^{20} moles C is required to significantly affect stabilisation time; we use a increased reactive layer depth of 2.5m (10^{18} mol C equiv.) for future model runs, due to uncertainty in estimation.

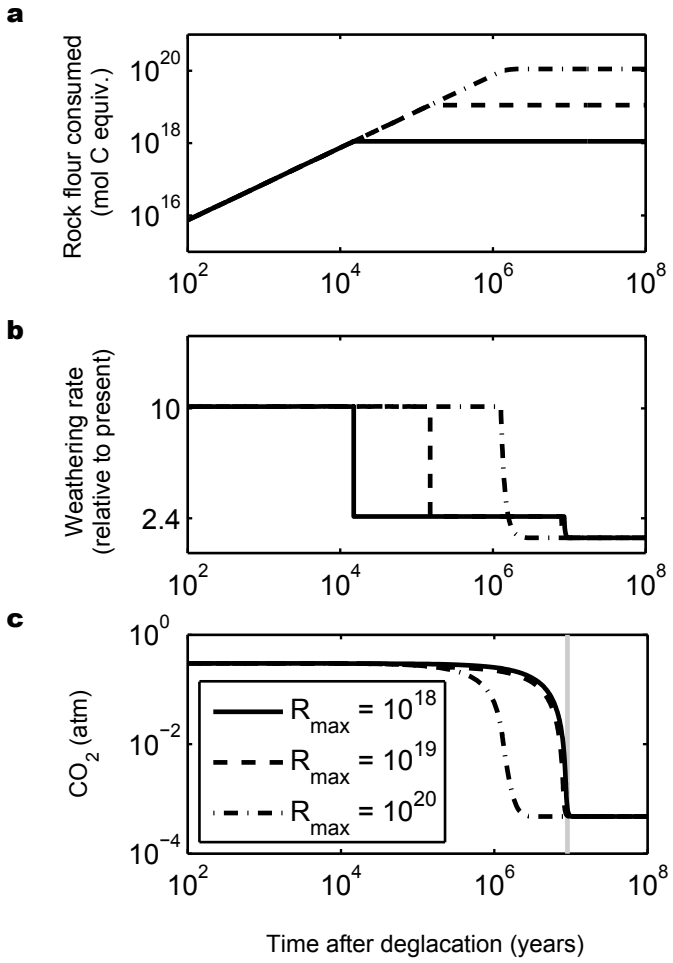

Figure 4.2.3: Stabilisation time after 0.3 atm CO_2 perturbation for different initial abundances of rock flour. a, Rock flour consumed. **b,** Silicate weathering rate. **c,** Atmospheric CO_2 concentration. Here R_{max} denotes the maximum amount of carbon (in moles) that can be drawn down via weathering of glacial rock flour before it is depleted. This figure shows the situation where D = 1, $W_{max} = 2.4$. The grey vertical line shows the stabilisation time when no flour is present (as in fig 4.2.2). The second drop in weathering rate here occurs as CO_2 returns to a stable concentration.

Our results indicate that the sequence of deep glaciations in the Neoproterozoic could be the result of a change of state in the long-term carbon-climate system to a regime which exhibits self-sustaining oscillations. If there was a long period in which global steady state temperature remained below the value required to trigger a snowball glaciation, this would be manifest as an oscillatory regime, with snowball glaciations alternating with warm

phases. Such a temperature forcing may well be attributed to the continental configuration at this time. It has been shown that the position of the continents at low latitudes at 750Ma, along with the prevalence of basaltic lithologies, could provide the necessary cooling to trigger the first snowball event (Donnadieu et al., 2004). It is thought that the continents would have remained near low latitudes until 600Ma (Li et al., 2008), after which they begin to drift to higher latitudes, relaxing the forcing. To investigate this possible mechanism we parameterise a runaway ice-albedo feedback in our model by imposing a change in albedo when temperature falls below a given value T_{crit}. Assuming the classic snowball scenario (Hoffman and Schrag, 2002), we choose $T_{crit} = 283K$ and allow deglaciation at 263K. Because deglaciation begins in the tropics, it is assumed to occur at lower temperature than is required for the ice sheets to initially advance. Throughout this work we assume a solar constant for 650Ma ($1298 Wm^{-2}$ (Caldeira and Kasting, 1992)), broadly representing the timeframe of interest. This allows glaciation at $\sim$150ppm CO_2, close to other estimates (Donnadieu et al., 2004). We impose the described cooling scenario in the model, adding a parameter ρ to represent enhancement of kinetic weathering. This follows the treatment of vascular plant colonisation in the Phanerozoic COPSE model runs (Bergman et al., 2004), acting as a multiplier on the kinetic weathering rate equation. To trigger oscillations we increase ρ by a factor of three for a period of 150Myrs. The magnitude of this enhancement is roughly analogous to the increase in basaltic surface area and mid-latitude runoff calculated in Donnadieu et al. (2004). For present day CO_2 degassing rate ($D = 1$), we require $W_{max} = 1.4$ to produce a rough analogue of the Neoproterozoic record. This parameter choice is shown in figure 4.2.4.

Assuming a higher CO_2 degassing rate shortens glacial duration and allows for larger values of W_{max} to produce the observed timing, in line with figure 4.2.2. We use output from the CO2SYS model (Lewis and Wallace, 1998) to approximate the atmospheric fraction of total ocean and atmosphere CO_2, assuming that there is gas exchange between atmosphere and ocean during glaciation Hoffman et al. (1998). The total solubility of CO_2 is higher in cold water than warm water, therefore deglaciation causes a large transfer of CO_2 from ocean to atmosphere.

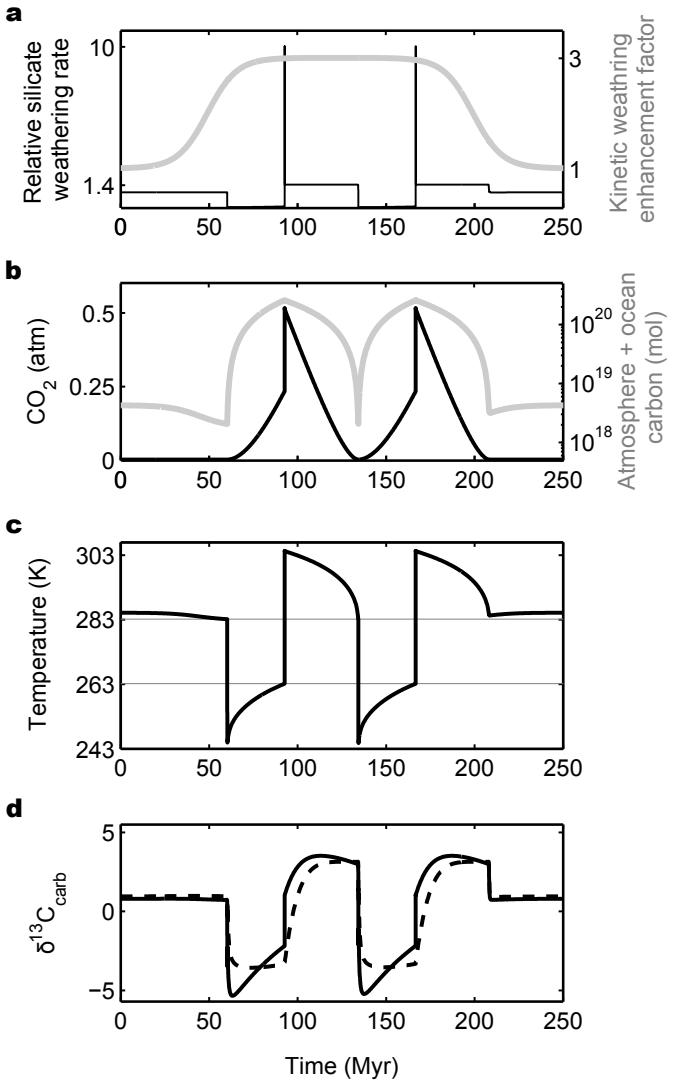

Figure 4.2.4: Cyclic solution when steady state temperature is forced below the ice-albedo runaway value for 150Myr. Here we let D = 1 and $W_{max} = 1.4$ to produce glacial timing on the order observed in the Neoproterozoic. **a,** The imposed kinetic weathering enhancement (ρ) is shown in grey; in black is the weathering rate relative to present. **b,** Total atmosphere/ocean carbon (grey), and atmospheric CO_2 (black). **c,** Temperature alongside snowball entry/exit thresholds. **d,** Model $\delta^{13}C$, solid line shows temperature/CO_2 dependent fractionation (Bergman et al., 2004), dashed line shows solution when fractionation effects are constant.

The solid line for $\delta^{13}C$ shows the isotopic fractionation of marine carbonates, assuming the fractionation effect on burial takes into account the equilibrium fractionation between oceanic and atmospheric carbon, and a de-

pendence on temperature, as in the full COPSE model (Bergman et al., 2004). The dashed line shows an alternative solution where fractionation effects are constant. Both treatments yield a continued positive fractionation during the interglacial period due to elevated burial of light organic carbon, due in turn to sustained above-steady-state nutrient fluxes from weathering. Higher assumption of W_{max} increases nutrient delivery and therefore also increases fractionation. Low productivity during glaciations causes a negative excursion. We do not expect a simple model such as this to replicate exactly the isotope record. Negative excursions preceding glaciation are not reproduced by our model, and may be due to direct temperature effects on productivity, which are not included. Our aim is to demonstrate that the extended period of system disequilibrium following a snowball glaciation should contribute to prolonged positive excursions in $\delta^{13}C$, and more complex analysis is required to fully understand the Neoproterozoic carbon cycle.

With the imposition of a suitable long term maximum weathering rate, oscillations in this simple carbon - climate model can provide a qualitative fit to the sequence of glaciations and carbon isotope variations in the Neoproterozoic. The globally transport limited scenario presents a prolonged period of elevated primary productivity, which would support suggested increases in oxygen concentration and phosphorous deposition over this time (Halverson et al., 2005; Canfield et al., 2008; Shields et al., 2007; Porter et al., 2004; Zhu et al., 2007; Scott et al., 2008). There is evidence for phosphorous deposition after the Marinoan glaciation but not after the Sturtian.

It is important to note that the mechanism we describe relies on a particular interpretation of the Neoproterozoic period, namely the Snowball Earth hypothesis (Hoffman et al., 1998; Kirschvink, 1992). It is possible that the Neoproterozoic actually contained more frequent smaller glaciations, which would not terminate via a high CO_2 'super greenhouse'. Due to our long timeframe for CO_2 drawdown, our prediction is highly testable, with for example one recent study proposing a rapid decline in CO_2 following the Marinoan glaciation (Kasemann et al., 2005). Further work to establish the duration of any post-glacial greenhouse may thus enable validation or falsification of mechanisms to explain these fascinating events.

4.3 Supplementary information 1: Estimating the amount of CO_2 consumed by rock flour weathering

Rapid weathering of post-glacial rock flour is an extremely important consideration for this work. The transport limited weathering flux will not take effect until after the depletion of this reactive surface layer. We therefore attempt to calculate the maximum moles of carbon that can be buried due to rock flour weathering. In model runs, the weathering rate is set to 10 times present day when flour is present, in accordance with Le Hir et al. (2009). This decreases via a step function to the transport limited value when no flour remains. For an initial estimate, we assume a 25cm surface layer depth (Le Hir et al., 2009) across the entire continental area (1.5×10^{14} m^2), giving a volume of 3.75×10^{13} m^3. We assume a loess density of 1.5×10^6 g m^{-3} (Bettis et al., 2003), therefore a total mass of 5.6×10^{19} g is calculated. Assuming a silicate cation fraction of 0.08 (West et al., 2005) gives a cation mass of 4.5×10^{18} g. Averaging the molar masses of Ca, Mg, Na and K gives ~ 32 g mol^{-1}, therefore we calculate $\sim 10^{17}$ moles for a global depth of 25cm, meaning that this many moles of carbon can be taken up by silicate weathering. The main uncertainty in this value is in the depth of rock flour following a snowball earth. We therefore test our model with up to three orders of magnitude more rock flour to be sure of results (see main text).

4.4 Supplementary information 2: Model derivation

The 0-D Phanerozoic earth system model, COPSE (Bergman et al., 2004), uses 10 reservoirs to couple the cycles of carbon, oxygen, sulphur and ocean nutrients nitrate and phosphate. We reduce the system to 4 reservoirs: Atmosphere and ocean CO_2 (A), buried organic carbon (G), buried carbonate carbon (C) and a single limiting nutrient (P), modelled as phosphate.

4.4.1 Model robustness

The following changes were made to COPSE to make it robust under conditions encountered when weathering rates and temperatures are very low, as in the Neoproterozoic glaciations. The silicate weathering formulation used in the GEOCARB models is used with a small modification. We follow the

derivation of Berner (1994) but do not make the simplifying assumption of temperature close to present day. The linear runoff approximation causes a singularity when temperature is low, and is amended by approximating the linear term with an exponential function. This gives an expression for the relative silicate weathering flux, assuming kinetic limitation:

$$W_K = \rho e^{\left(k_1 \frac{T-T_0}{TT_0}\right)} \left(e^{k_2(T-T_0)}\right)^{0.65} \sqrt{\mathrm{NCO_2}} \tag{S1}$$

Here $k_1 = 7537.69$ and $k_2 = 0.03$. T is average surface temperature in Kelvin, T_0 is present day average surface temperature and $\mathrm{NCO_2}$ denotes concentration of CO_2 normalised to pre-industrial concentration. To obtain an expression for the global silicate weathering flux, equation S1 is multiplied by a factor ρ to represent possible enhancement of weathering due to continental configuration and composition. It is important to note that enhancing the kinetic weathering rate in this way does not affect the maximum transport-limited value. A higher value of ρ means that the maximum transport-limited rate can be achieved with lower temperature and/or runoff.

COPSE defines the function *anox* which gives a numerical value between 0 and 1 inclusive for the degree of ocean anoxia. The formulation used in the original model allows for negative values when ocean nutrient is extremely low. We truncate these to zero. We also add a dependence on new production to the iron-sorbed phosphorus burial flux (as is already applied to the other nutrient burial fluxes) to prevent unrealistic burial rates when nutrient concentration is low.

4.4.2 Temperature approximation

We derive a temperature approximation by first scaling for a lower solar constant, then using a previously calculated climate sensitivity and radiative forcings to adjust for different carbon dioxide concentrations. To scale for a decreased solar constant, we use an energy budget model for a single layer grey atmosphere in radiative equilibrium:

$$T_{EBM} = \left(\frac{S(1-\alpha)}{4\sigma\left(1-\frac{\epsilon}{2}\right)}\right)^{\frac{1}{4}} \tag{S2}$$

Here S is the solar constant in Wm^{-2}, α is planetary albedo, σ is Stefan's constant and ϵ represents the emissivity of the atmosphere. Assuming present day temperature of 288K, solar constant of 1368 Wm^{-2} and albedo of 0.3, we derive an emissivity $\epsilon = 0.773$. The solar constant at 650Ma was 1298 Wm^{-2} (Caldeira and Kasting, 1992). With a constant emissivity (i.e. Modern day greenhouse gas concentrations), equation S2 gives an average surface temperature of $T_{\mathrm{base}} = 284.3\mathrm{K}$ for the late Neoproterozoic. To account for increased carbon dioxide concentrations, we add a term for radiative forcing from CO_2 to T_{base}

$$T = T_{\mathrm{base}} + \mu \cdot F_{CO_2} \tag{S3}$$

Where F_{CO_2} is the radiative forcing from carbon dioxide and μ is the climate sensitivity (the ratio of change in radiative forcing to change in temperature). Our climate sensitivity is taken from previous runs of a radiative convective climate model and radiative forcings from previous runs of the AER line-by-line radiative transfer code (Clough et al., 2005; Goldblatt et al., 2009b), we take $\mu = 0.1815$ and $F_{CO_2} = a\lambda^4 + b\lambda^3 + c\lambda^2 + d\lambda + e$ where $a = 0.2507, b = 3.9216, c = 23.8113, d = 83.4113, e = 131.6138$ and $\lambda = \log(\mathrm{CO_2(atm)})$.

We fit a curve for $10^{-5} < \mathrm{CO_2(atm)} < 10^{-1}$ and extrapolate this to $5{\times}10^{-1}$ atm. Correct representation of radiative forcing above 10^{-1} atm is a rather involved problem, necessitating representation of pressure broadening from higher total pressure, CO_2 self-continuum, many weaker lines and possible line mixing, and is beyond the scope of this paper, hence our approach. For the purpose of this work, it is only important that the temperature be sufficient to 'max out' the global weathering rate, which occurs at a much lower CO_2 concentration.

The COPSE model combines ocean and atmosphere carbon dioxide into a single reservoir, with a parameter ϕ to represent the fraction that exists in the atmosphere (and therefore contributes to the greenhouse effect). As more carbon dioxide accumulates in the atmosphere/ocean reservoir (A), a greater fraction will reside in the atmosphere. We combine our temperature function with the CO2SYS carbon speciation model (Lewis and Wallace, 1998) to derive a formula for ϕ in terms of A. The best fit to results is described by:

$$\phi = \frac{gA}{A+h} \tag{S4}$$

where $g = 0.78$ and $h = 1 \times 10^{20}$ mol for $\alpha = 0.3$, $h = 5.3 \times 10^{20}$ mol for $\alpha = 0.6$. This treatment contrasts to the 'hard snowball' model, where atmosphere and ocean are unable to exchange species. However, it has been shown that equilibrium between atmosphere and ocean during a snowball event could occur with only 100km^2 of open water (Le Hir et al., 2008), or cracks in sea ice (Hoffman et al., 1998) and thus our approach has been used in previous snowball earth simulations (Higgins and Schrag, 2003).

4.4.3 Weathering formulation

For this work we assume that silicate weathering is kinetically limited until the global transport limit is reached. This can be written in the form:

$$W = \begin{cases} W_K : & W_K < W_{\max} \\ W_{\max} : & W_K \geq W_{\max} \end{cases} \tag{S5}$$

where W is the overall weathering rate, W_K is the kinetically limited weathering rate and $W_{\max}$ is the transport limited rate, expressed relative to the present day. We describe the transition from the kinetically limited curve to the transport limited value using a sigmoid function.

$$W = (W_{\max} - W_K)\left(1 + e^{-k_3(W_K - W_{\max})}\right)^{-1} + W_K \tag{S6}$$

where $k_3 = 100$. Equation S6 follows equation S1 for $W_K < W_{\max}$, but asymptotes to $W_{\max}$ for $W_K > W_{\max}$.

4.4.4 Glacial flour abundance and weathering enhancement

We represent the global reservoir of glacial rock flour, R, in terms of the number of moles of carbon it can potentially draw down via weathering. If a snowball glaciation is triggered, R is set to zero. On deglaciation we set $\frac{\mathrm{d}R}{\mathrm{d}t}$ equal to the silicate weathering flux. $W_{\max}$ is dependent on the size of R, taking the maximum value of 10 for $R < R_{\max}$ and reverting to the prescribed transport limited value when $R = R_{\max}$. Here $R_{\max}$ is the assumed abundance of glacial flour defined by the amount of CO_2 it can potentially

weather. The transition between weathering rates follows a step function. We choose this formulation in order to allow the maximum CO_2 drawdown for a given quantity of rock flour, noting that the weathering flux may actually decrease with time (Vance et al., 2009).

4.4.5 Ice-albedo instability

To parameterise an ice-albedo instability we define two distinct albedos in our model and allow the value to change when a certain temperature threshold is reached. For the temperature world we let:

$$\alpha = \begin{cases} \alpha_{\text{base}} : & T > T_{\text{crit}} \\ \alpha_{\text{ice}} : & T \leq T_{\text{crit}} \end{cases} \tag{S7}$$

For the glaciated world we follow Hoffman and Schrag (2002) and assume a lower escape temperature, T_{escape}:

$$\alpha = \begin{cases} \alpha_{\text{base}} : & T > T_{\text{escape}} \\ \alpha_{\text{ice}} : & T \leq T_{\text{escape}} \end{cases} \tag{S8}$$

Here $\alpha_{\text{base}} = 0.3$. We let $\alpha_{\text{ice}} = 0.6$, $T_{\text{crit}} = 283\text{K}$, $T_{\text{escape}} = 263\text{K}$. This allows glaciation at $\sim$150ppm CO_2 and deglaciation at $\sim$0.25 atm, broadly in line with previous work on snowball Earth (Hoffman et al., 1998; Pierrehumbert, 2005; Donnadieu et al., 2004). For a simple model, α moves linearly between α_{base} and α_{ice} if temperature falls below T_{crit}, and returns to α_{base} if T_{escape} is reached whilst in a snowball glaciation.

Reduction of weathering fluxes due to glaciation is modelled using a multiplier, W_{glacial}, for global silicate and carbonate weathering fluxes. W_{glacial} depends on only the albedo, α and is modelled using a step function so that:

$$W_{\text{glacial}} = \begin{cases} 1 : & \alpha = \alpha_{\text{base}} \\ 10^{k_{\text{ice}}} : & \alpha = \alpha_{\text{ice}} \end{cases} \tag{S9}$$

k_{ice} is chosen to allow temperature during the snowball glaciation to stabilise above T_{escape} in order that deglaciation can occur. This requires $k_{\text{ice}} = -2$.

4.4.6 Carbon isotopes

To produce results that may be compared to the geological record, we calculate the isotopic composition of carbon throughout model runs. To do this we run a duplicate carbon system that tracks the movement of the lighter isotope carbon-12. The δ^{13}C value of a sample is a measure of the ratio of carbon-13 atoms to carbon-12 atoms, and is expressed relative to a standard:

$$\delta^{13}\mathrm{C}_{\mathrm{sample}} = \left(\frac{\mathrm{R}^{13}_{12\mathrm{sample}}}{\mathrm{R}^{13}_{12\mathrm{PDB}}} - 1 \right) \cdot 1000 \tag{S10}$$

where R^{13}_{12} is the ratio of carbon-13 atoms to carbon-12 atoms and $\mathrm{R}^{13}_{12\mathrm{PDB}} = 0.0112372$. If F_{C} is a model flux of carbon, we define the corresponding flux of carbon-12 ($F_{^{12}\mathrm{C}}$) as:

$$F_{^{12}\mathrm{C}} = F_{\mathrm{C}} \cdot \mathrm{R}^{12}_{12+13} \tag{S11}$$

where R^{12}_{12+13} is the ratio of carbon-12 to total carbon in the parent reservoir.

If a flux undergoes a fractionation effect of ι parts per thousand, the modified ratio of carbon-12 to total carbon in the flux is calculated:

$$\mathrm{R}^{12}_{12+13} = \frac{1}{1 + \mathrm{R}^{13}_{12}} = \frac{1}{1 + \mathrm{R}^{13}_{12\mathrm{PDB}} \left(\frac{\delta^{13}\mathrm{C} + \iota}{1000} + 1 \right)} \tag{S12}$$

where δ^{13}C is the fractionation relative to PDB of the parent reservoir. We assume a photosynthetic fractionation effect of -30‰. For fractionation due to carbonate burial we consider both a constant effect (+1‰) and a temperature-dependent function as used in COPSE:

$$\delta_{mccb} = \phi \left(\frac{9483}{T} - 23.89 \right) - \frac{4232}{T} + 15.1 \tag{S13}$$

Here δ_{mccb} represents the difference in composition between atmosphere/ocean CO_2 and buried carbonate in units of per mille (‰) relative to PDB. T is temperature in degrees Kelvin and ϕ is the fraction of total CO_2 that is in the atmosphere.

4.4.7 Full model equations

Reservoirs and fluxes are taken directly from the COPSE model with the following exceptions: Land organic carbon burial ($locb$) is removed to reflect the absence of plants in the Neoproterozoic. Iron-sorbed phosphate burial ($fepb$) is amended as described above. The weathering fluxes $silw$ and $oxidw$ are redefined to include the glacial limitation, W_{glacial}, and transport limitation in the case of $silw$. We hold oxygen concentration (denoted O) constant at an assumed Neoproterozoic value of 1% of the atmosphere, and therefore assume no dependence of $oxidw$ on oxygen concentration. Carbonate weathering is assumed to follow the silicate weathering equation for this analysis, as it has no net effect on CO_2. The crustal reservoirs of organic and carbonate carbon (G and C) are held constant. Table 5 displays model fluxes, table 6 shows the reservoir calculations, table 7 defines the forcing parameters and table 8 shows model constants.

Name	Shorthand	Equation
Marine organic carbon burial	$mocb$	$k_1 \left(\frac{P}{P_0}\right)^2$
Nutrient weathering	$phosw$	$k_8 \left(\frac{2}{12}\frac{silw}{silw_0} + \frac{5}{12}\frac{carbw}{carbw_0} + \frac{5}{12}\frac{oxidw}{oxidw_0}\right)$
Marine organic phosphate burial	mopb	$\frac{mocb}{CPsea}$
Calcium-bound phosphate burial	$capb$	$k_2 \frac{mocb}{mocb_0}$
Iron-sorbed phosphate burial*	$fepb$	$\frac{k_3}{k_4}\left(1 - anox\left(O, P\right)\right)\frac{mocb}{mocb_0}$ where $anox = 1 - k_4\left(\frac{O}{O_0}\frac{P_0}{P}\right)$
Silicate weathering*	$silw$	$k_5\left\{\left(W_{\max} - W_K\right)\left(1 + e^{-k_3(W_K - W_{\max})}\right)^{-1} + W_K\right\}$ where $W_K = W_{\text{glacial}}\rho e^{\left(k_1\frac{T-T_0}{TT_0}\right)}\left(e^{k_2(T-T_0)}\right)^{0.65}\sqrt{\text{NCO}_2}$
Oxidative weathering*	$oxidw$	$k_7 W_{\text{glacial}}$
Organic carbon degassing	$ocdeg$	$k_9 D$
Carbonate carbon degassing	$ccdeg$	$k_{10} D$

Table 5: List of fluxes: (* indicates a flux that has been modified for this work)

Name	Equation
Phosphate	$\frac{\mathrm{d}P}{\mathrm{d}t} = phosw - mopb - capb - fepb$
Atmosphere/ocean CO_2	$\frac{\mathrm{d}A}{\mathrm{d}t} = -mocb - silw + oxidw - carbw + ocdeg + ccdeg + carbw$
Buried organic carbon	$\frac{\mathrm{d}G}{\mathrm{d}t} = 0$
Buried carbonate carbon	$\frac{\mathrm{d}C}{\mathrm{d}t} = 0$

Table 6: Reservoir calculations

Name	Meaning
D	Relative CO_2 degassing rate
ρ	Rock weatherability

Table 7: Model forcings

Name	Meaning	Size	Source
k_1	Present day total organic carbon burial	9×10^{12} mol C yr^{-1}	COPSE
k_2	Present day Ca associated phosphorus burial	1.5×10^{10} mol P yr^{-1}	COPSE
k_3	Present day Fe associated phosphorus burial	6×10^{9} mol P yr^{-1}	COPSE
k_4	Initial oxic fraction	0.86	COPSE
k_5	Present day silicate weathering	6.65×10^{12} mol C yr^{-1}	for steady state
k_6	Present day carbonate weathering	1.335×10^{13} mol C yr^{-1}	COPSE
k_7	Present day oxidative weathering	7.75×10^{12} mol C yr^{-1}	for steady state
k_8	Present day reactive phosphorus weathering	5.7×10^{10} mol P yr^{-1}	for steady state
k_9	Present day organic carbon degassing	1.25×10^{12} mol C yr^{-1}	COPSE
k_{10}	Present day carbonate carbon degassing	6.65×10^{12} mol C yr^{-1}	COPSE
$CPsea$	C:P burial ratio	250 mol:mol	COPSE
A_0	Present day atmosphere/ocean CO_2	3.193×10^{18} mol	COPSE
P_0	Present day ocean phosphate	3.1×10^{15} mol	COPSE
O_0	Present day atmosphere/ocean O_2	3.7×10^{19} mol	COPSE

Table 8: List of constants

4.5 Application of transport limitation and revised temperature calculation to Phanerozoic modelling

The work in this chapter has produced two ideas worthy of investigation in respect to Phanerozoic climate. Firstly, attempting to model the conditions following a snowball Earth event has required the development of a new temperature approximation, based on a previous radiative-convective climate model and the AER line-by-line radiative transfer code (Clough et al., 2005; Goldblatt et al., 2009b). Secondly, geological limitation of the terrestrial weathering process could also have operated over the Phanerozoic. As discussed in the published letter, if the global degassing rate for CO_2 is greater than the maximum possible burial rate via weathering, there would be no mechanism to stop the build up of CO_2 in the atmosphere. Current methods of estimating the global degassing rate from the seafloor spreading rate return a maximum degassing rate of around 1.75 times present day for the late Mesozoic (Gaffin, 1987; Berner, 1990). Following the rough estimate for a Phanerozoic weathering rate limit of around 2.4 times present day (Mills et al., 2011), the global erosion rate would only have to fall below 75% of the present day value in order for CO_2 degassing to overwhelm the rate of burial, and the system to be unable to stabilise CO_2 concentration in the atmosphere. Estimates of uplift rates for the late Mesozoic happen to be around this value (Berner, 1994).

4.5.1 Comparison of temperature functions for Phanerozoic carbon cycle modelling

Figure 4.5.5 plots the CO_2-temperature functions used in the GEOCARB and COPSE models with the function derived for the work on transport limitation (Mills et al., 2011; Clough et al., 2005; Goldblatt et al., 2009b). The temperature approximation of Caldeira and Kasting (1992) allows for changes in planetary albedo and is plotted with both fixed and variable albedo. For the other functions albedo is fixed at 0.3. As noted previously, the temperature approximation used in COPSE (Caldeira and Kasting (1992) variable albedo) and in the more recent GEOCARB models (Berner and Kothavala, 2001) show fair agreement over the expected Phanerozoic CO_2 range ($\sim 1 - 20$PAL). The RCM-LBL approximation used in Mills et

al. (2011) was designed for application to extremely high CO_2 environments, and displays a far more conservative relationship between CO_2 and temperature than the previous approximations. The spread of results here highlights the uncertainty in estimating global temperature based on a small number of parameters and over a massive range of CO_2 concentrations. None of these approximations should be considered 'the correct one', however the effect of the uncertainty in global temperature estimation on Phanerozoic model predictions should be assessed.

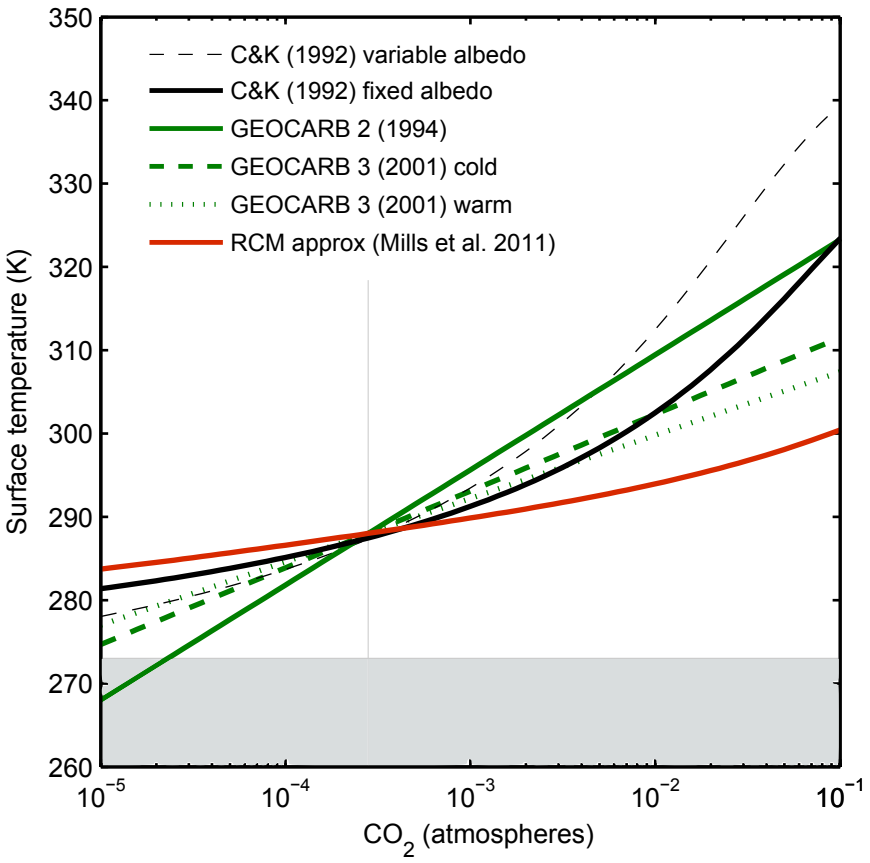

Figure 4.5.5: Temperature approximations used in carbon cycle box models. The black lines show the approximation of Caldeira and Kasting (Caldeira and Kasting, 1992), which is used in the COPSE model. Solid line shows fixed albedo, dashed line shows variable albedo solution. Green lines show the approximations derived for the GEOCARB models (Berner, 1994; Berner and Kothavala, 2001) and the red line shows the approximation developed for the work in this chapter (Goldblatt et al., 2009b; Clough et al., 2005). Albedo is fixed in these approximations. The grey shaded area indicates a temperature below 0°C and the grey vertical line shows pre-industrial CO_2 concentration for reference.

Figure 4.5.6 shows the results of Phanerozoic runs in the Minimal Model from chapter 3. The black lines show runs with the temperature approximation from Mills et al. (2011), the grey lines show runs using the temperature approximation from Caldeira and Kasting (1992) with variable albedo. These examples are taken as the sensitivity end-members (see figure 4.5.5) and the model uses the nutrient system from COPSE to estimate organic burial rates.

With the more conservative Mills et al. function, around twice the concentration of ocean/atmosphere CO_2 is required to stabilise the carbon cycle before the evolution of vascular plants at 400Ma. However the temperature prediction is lower due to the assumption that CO_2 has a direct effect on weathering (through plant CO_2- fertilization (Berner, 1994)).

The model is run with the assumption of a large (7-fold) increase in weathering efficiency due to the evolution of vascular plants, a smaller (and probably more reasonable (Drever, 1994)) change in weathering efficiency would bring temperature predictions closer to present day for both models, as described in the previous chapter.

The results here show that the climate sensitivity to carbon dioxide is also an important uncertainty in estimating early Phanerozoic temperature, with a lower sensitivity bringing all estimates closer to present day temperature. The prediction of high global temperature by GEOCARB and COPSE for the supposedly glacial periods in the Cambrian and Ordovician may be partly explained by the use in those models of temperature functions that are towards the extreme of plausible relationships. It is important to note that the use of a more conservative CO_2-temperature relationship does not significantly change the climatic forcing required to reach extremely low global temperature in the Neoproterozoic. A factor 3 enhancement is required to reach the ice-albedo run-away threshold, as in section 4.2.

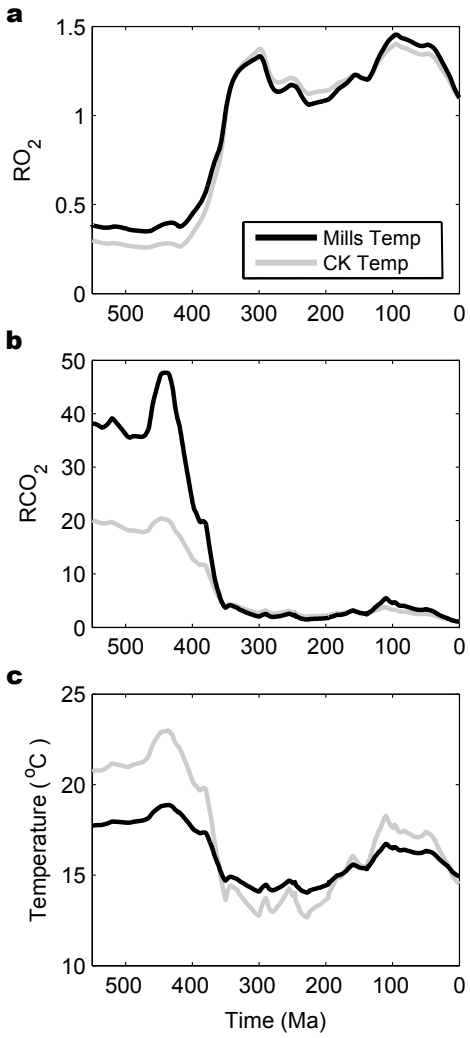

Figure 4.5.6: Phanerozoic COPSE model run for different temperature functions. **a** Relative atmospheric oxygen. **b** Relative atmospheric CO_2. **c**, Global average surface temperature. For all panels grey lines show temperature function from Caldeira and Kasting (1992) and black lines show temperature function from Mills et al. (2011)

4.5.2 Atmospheric fraction of carbon dioxide

To complement the assessment of temperature functions, this section briefly reviews the function used to express the fraction of total (ocean plus atmosphere) CO_2 which resides in the atmosphere, and thus contributes to the greenhouse effect, denoted ϕ. It has been shown during the COPSE model derivation (Bergman, 2003) that changing this calculation does not alter the

predictions for atmospheric CO_2 over the Phanerozoic, this is because the atmospheric reservoir is regulated by the temperature dependence of continental weathering, with the oceanic reservoir changing accordingly as a 'slave' variable. Changes to the calculation do however alter the total amount of ocean and atmosphere carbon dioxide for a given atmospheric concentration, which is very important in calculating the timescales for CO_2 removal (Mills et al., 2011) as well as the power of processes that are controlled by oceanic CO_2 concentration rather than atmospheric (e.g. weathering of deep ocean crust (Sleep and Zahnle, 2001)). Here the approximation derived from the CO2SYS program (see section 4.4) is tested against a physically based treatment used in an extension of the COPSE model (Bergman, 2003).

Kump and Arthur derived a simple expression for the atmospheric fraction of total CO_2 by assuming that the ocean is saturated with respect to $CaCO_3$ and equilibrated with atmospheric carbon dioxide (calcium concentration is assumed constant). They calculate atmospheric CO_2 as:

$$\mathrm{CO_2} = \left(\frac{\mathbf{A}}{\mathbf{A}_0}\right)^2 \cdot \mathrm{CO_2}\,(0) \tag{4.5.1}$$

where $\mathrm{CO_2}\,(0)$ is the present day concentration and $\mathbf{A}$ is the size of the combined ocean and atmosphere CO_2 reservoir. $\mathbf{A}_0$ is the size of this reservoir at present day. In COPSE, dependence on temperature and explicit treatment of the oceanic carbon reservoir is added to this analysis, yielding the expression:

$$\mathrm{RCO_2} = \frac{\mathrm{CO_2}}{\mathrm{CO_2}\,(0)} = \mathrm{e}^{\mathrm{kc2(T_0-T)}} \cdot \left(\frac{\Sigma\mathrm{CO_2}}{\Sigma\mathrm{CO_2}\,(0)}\right)^2 \tag{4.5.2}$$

here kc2 is a constant with value -0.0448 K^{-1} (Bergman, 2003), $\Sigma\mathrm{CO_2}$ is the number of moles of CO_2 in the ocean and $\Sigma\mathrm{CO_2}\,(0)$ is the present day value of this. T is average surface temperature and $\mathrm{T_0}$ is the present day value, 288K. In order to compare this treatment to the approximation derived in chapter 4, the above equation must be solved by iteration. Equation 4.5.2 is rearranged so that it may be solved to give the atmospheric fraction ϕ as a function of $\mathbf{A}$ alone.

$$\frac{\phi\mathbf{A}}{\phi_0\mathbf{A}_0} = \mathrm{e}^{\mathrm{kc2(T_0-T)}} \cdot \left(\frac{(1-\phi)\,\mathbf{A}}{(1-\phi_0)\,\mathbf{A}_0}\right)^2 \tag{4.5.3}$$

$$\phi = \mathrm{e}^{\mathrm{kc2(T_0-T)}} \cdot \left(\frac{(1-\phi)\,\mathbf{A}}{(1-\phi_0)\,\mathbf{A}_0} \right)^2 \cdot \frac{\phi_0 \mathbf{A}_0}{\mathbf{A}} \tag{4.5.4}$$

here $\phi_0 = 0.01614$ as in COPSE.

In order to iterate this equation, the value of A is fixed, allowing computation of the stable value of ϕ. Temperature must be calculated at each stage from the atmospheric CO_2 concentration, which itself is calculated from **A** and the current value of ϕ. For this comparison we assume an albedo fraction of 0.3 and use the temperature approximation from Mills et al. (2011). Figure 4.5.7 plots the relationship between the size of **A** and the atmospheric fraction of CO_2 for the above formulation. It is compared to the approximation used in Mills et al., which is computed using the 'CO2SYS' program of Lewis and Wallace (1998).

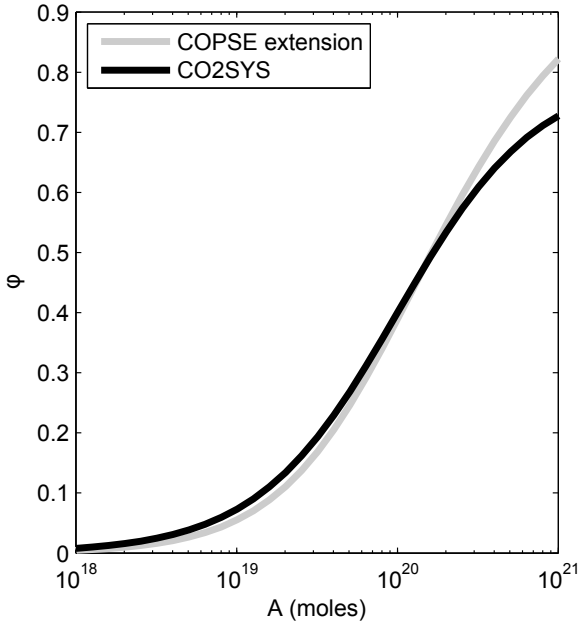

Figure 4.5.7: Atmospheric fraction of carbon dioxide The atmospheric fraction (ϕ) is plotted against total atmosphere and ocean CO_2 (**A**). Black line shows approximation derived from CO2SYS program (Lewis and Wallace, 1998), grey line shows approximation from extended COPSE model (Bergman, 2003)

As the figure shows, both approximations give very similar results. Divergence does occur when **A** is above 3×10^{20} moles, but this is above the maximum value reached in any model runs, including the snowball scenar-

ios. Interchanging these functions therefore has very little effect on model behaviour, the approximation used in Mills et al. is adopted for further work because it is more computationally efficient.

4.5.3 Transport limitation of weathering in the Phanerozoic

Earlier in the chapter it was shown that transport limitation of terrestrial weathering would place an upper limit on the drawdown flux of CO_2, thus extending the timeframe for stabilisation of the system after a large CO_2 perturbation. However there is another potential effect of this limitation: if the global degassing rate rises above the maximum possible weathering rate the system would be unable to stabilise and CO_2 could accumulate over millions of years, greatly increasing surface temperature. Geochemical proxies suggest that CO_2 concentration peaked at around 15 times present atmospheric level (PAL) in the Mesozoic (Royer et al., 2004), however model predictions with kinetically based weathering fluxes do not reach this level, typically staying below 5 times PAL (Bergman et al., 2004; Berner, 1994; Arvidson et al., 2006). The maximum transport-limited weathering rate is dependent on material supply via erosion (West et al., 2005). Estimates for Mesozoic continental uplift rates using both strontium isotope models (Berner, 1994) and sediment abundance data (Ronov, 1993) give low values, perhaps as low as 0.5 times present day, whilst estimates of the degassing rate are between 1 and 1.5 times present day. With a higher degassing rate and a lower erosion rate, it may have been possible that CO_2 outgassing exceeded the maximum burial rate via silicate weathering in the Mesozoic, which could perhaps explain the unexpectedly high CO_2 concentration recorded by proxies.

For a simple test of this idea, the Minimal Model is run through the Phanerozoic with an imposed maximum weathering rate limit. Again the COPSE nutrient system is used to infer organic burial rates to retain maximum predictive power, and the results are compared to a run in which no transport limit is assumed, roughly equivalent to the original COPSE predictions (Bergman et al., 2004). Figure 4.5.8 shows results when the maximum weathering rate (W_{max}) is fixed at 1.33 times present day. For this run there is no dependence of W_{max} on the erosion rate. It can be seen in panel **d** that the global silicate weathering rate for the unmodified model rises above

the imposed limit at two points in the Phanerozoic, which correspond to periods of high degassing. When the weathering limitation is imposed, these periods see rapidly rising CO_2 concentration, halted only when the degassing rate falls sufficiently so that the maximum carbon sink from weathering can overwhelm the volcanic CO_2 source.

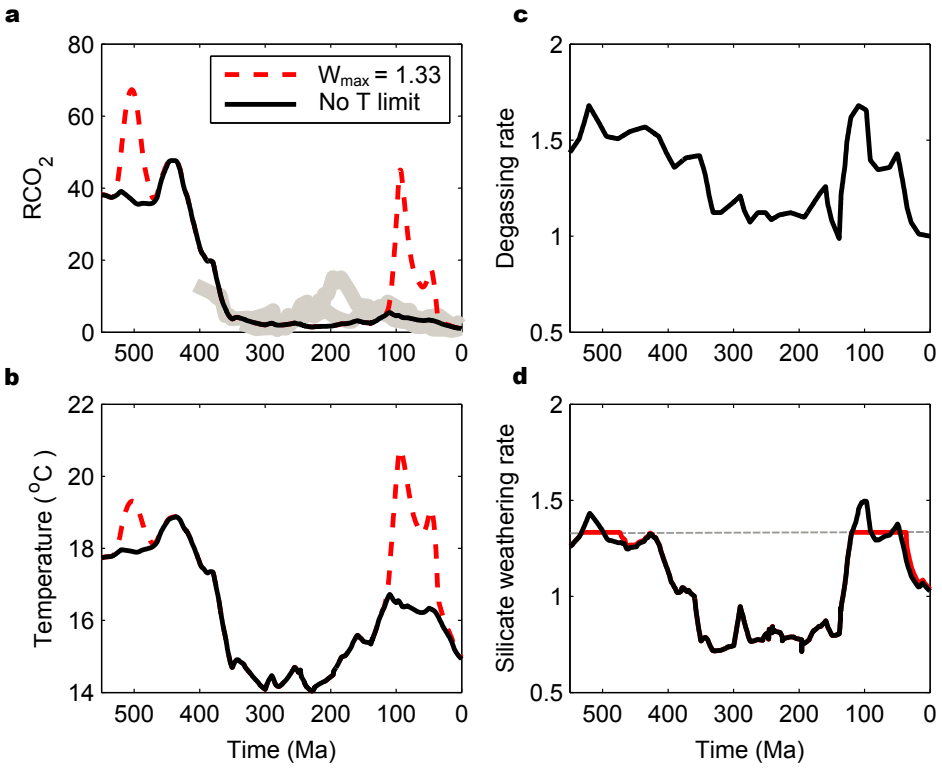

Figure 4.5.8: COPSE model run through Phanerozoic with a fixed weathering rate limit Black line shows model run with no transport limitation of weathering, red line shows model predictions when the maximum terrestrial weathering rate (W_{max}) is fixed at 1.33 times present day. Grey lines in panel **a** show CO_2 proxy data from Royer et al. (2004). The dashed grey line in panel **d** shows the assumed transport limited weathering rate.

This treatment is certainly an oversimplification and the predictions do not line up well with the proxy data, but it serves well to demonstrate the mechanism in question. Allowing $W_{max} \geq 1.5$ removes the possibility of transport limitation occurring and it is likely that $W_{max} = 1.33$ is an unrealistically low assumption - the simple calculation in Mills et al. (2011) gave a value of $W_{max} \approx 2.4$ for the Phanerozoic.

In figure 4.5.9 it is assumed that the transport limited maximum weathering rate is influenced by the rate of erosion due to cation supply (West et al., 2005), i.e. $W_{max} = k_{transport} \cdot \epsilon$ where ϵ is the relative erosion rate. It is assumed that erosion rate scales with the uplift rate forcing in the model.

Because of the assumed lower erosion rate in the Mesozoic, a higher, and more plausible value for the present day transport limited rate ($k_{transport}$) now results in a CO_2 spike similar to the previous model runs. The magnitude of this is very sensitive to the value of $k_{transport}$, as carbon dioxide quickly builds up once the weathering process becomes transport limited. Notice also that the CO_2 spike observed at around 500Ma in the previous model run has not occurred, this is because although the degassing rate at this time was high, the uplift rate is also assumed to be high which compensates for the increase.

The timing of the event in this model still does not fit well with the timing suggested by proxies. The CO_2 spike shown by proxy records at $\sim$ 200Ma does appear to coincide with a low global uplift rate, but the possibility of a transport limited global weathering regime can possibly be ruled out based on evidence for comparatively low degassing rates at this time. The combination of predicted low uplift rate and high degassing rate at 100Ma can produce a runaway CO_2 event in the model under reasonable assumptions for the transport limited rate, however an event of this kind is not recorded in the available proxies for this time (Royer et al., 2004). In addition, the peak in degassing rate at 100Ma has been questioned by recent estimates of the spreading rate which utilize the age distribution of the oceanic lithosphere (Rowley, 2002), these estimates suggest a constant degassing rate for the last 180Ma.

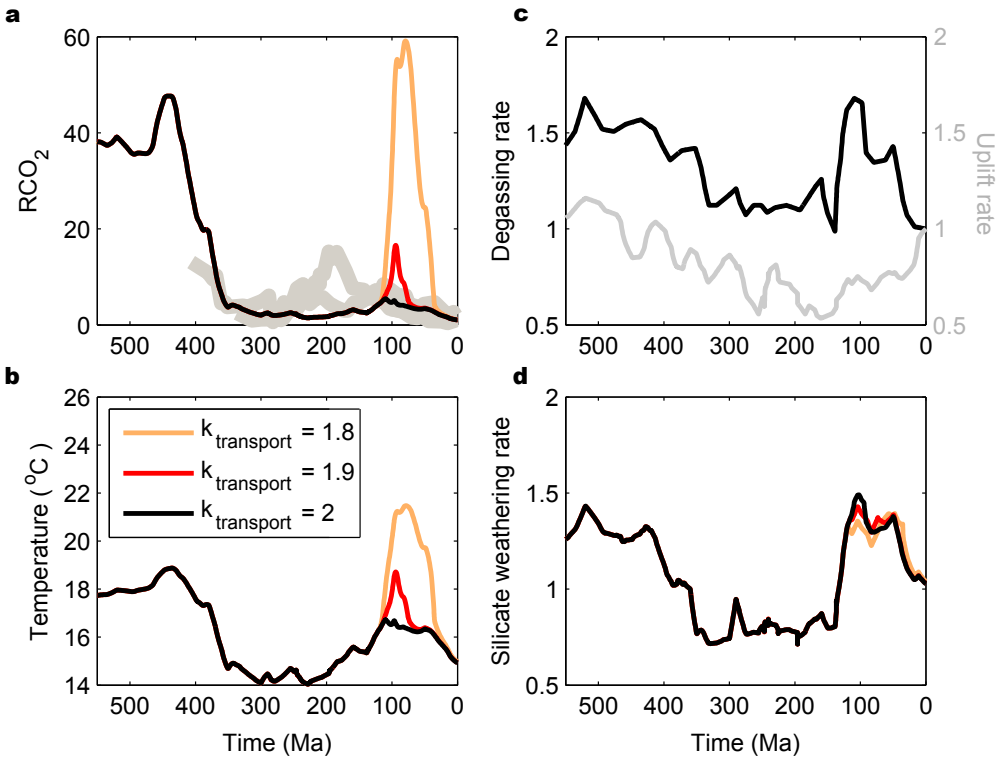

Figure 4.5.9: COPSE model run through Phanerozoic with a weathering rate limit dependent on the uplift rate. $k_{transport}$ is the present day maximum achievable weathering rate, relative to the actual weathering rate. Grey lines in panel **a** show CO_2 proxy data from ref (Royer et al., 2004)

This work suggests that a global transport limitation event did not occur in the Phanerozoic. Such an event would necessarily coincide with a high degassing rate and low uplift rate. Taking $\frac{\text{Degassing}}{\text{Uplift}}$ for the Phanerozoic proxies returns a substantial maximum at only $\sim$ 100Ma, which corresponds to the CO_2 spike in the model runs. The proxy data for low CO_2 at this time (Royer et al., 2004) implies that the CO_2-weathering feedback was operating, in which case it would be expected to be operating in the earlier Phanerozoic, where the quantity $\frac{\text{Degassing}}{\text{Uplift}}$ is lower. Assuming a constant degassing rate for the period 180-0Ma (Rowley, 2002) removes all significant peaks from the $\frac{\text{Degassing}}{\text{Uplift}}$ curve, leaving no implication of a period of global transport limitation.

4.6 Chapter summary and discussion

4.6.1 Summary of main findings

1) Transport limitation of the terrestrial weathering process places a cap on the global rate of carbon burial via silicate weathering. A rough estimate for the Phanerozoic places this limit at ~ 2.4 times the present day rate.

2) The transport limit affects the time taken for climate to stabilize following a large CO_2 perturbation. Assuming that snowball Earth glaciations terminate via a high-CO_2 meltback, the timescale for stabilization is on the order of 10^7 years, similar to the gap between the Neoproterozoic low latitude glaciations.

3) It is proposed here that a $\sim$ 150Myr climatic cooling event operated over the Neoproterozoic, triggered by the dispersion of the supercontinent Rodinia and associated paleogeographical weathering effects, and was responsible for the sequence of deep glaciations via the transport limitation mechanism.

4) In this situation the periods between glaciations would be characterised by an unbalanced carbon cycle, excess nutrient delivery and high rates of organic burial, but it is unclear exactly how this would have contributed to ocean oxygenation over the Neoproterozoic.

5) It is theoretically possible for the global CO_2 degassing rate to exceed the maximum transport-limited burial rate, triggering run-away CO_2 buildup. But it is unlikely to have happened during the Phanerozoic.

4.6.2 Discussion

The snowball Earth scenario represents a 10^7 year perturbation to global biogeochemistry, and it seems natural to assume that system recovery would be on the same timescale. The work in this chapter highlights for the first time that the warm climate would be expected to persist for tens of millions

of years following the glacial melt.

The climate and ice sheet dynamics of snowball glaciations have been the subject of intense scrutiny over the last 20 years (Hoffman et al., 1998; Leather et al., 2002; Pierrehumbert, 2005; Lewis et al., 2007; Font et al., 2010; Heron et al., 2011), particularly with the view to establishing the likelihood of the global biota surviving such an event (McKay, 2000; Vincent and Howard-Williams, 2000; Knoll, 2003; Pollard and Kasting, 2005). It has also been proposed that the occurrence of the Neoproterozoic snowball events may have had a dramatic effect on the evolution of early animals (Knoll and Carroll, 1999). Large scale environmental perturbation would be expected to provide an ecological opportunity for the survivors (Bartley et al., 1998), and the environmental selection effects of surviving in refugia during glaciation may have promoted multicellularity (Boyle et al., 2007).

More critical to the evolution of animals is the global abundance of oxygen (Catling et al., 2005; Runnegar, 1991), and the oxygenation event over the Neoproterozoic is proposed to have removed a low-O_2 evolutionary barrier (Canfield et al., 2007; Knoll, 2003). A biota-driven oxygenation has previously been inferred directly from the large positive excursions in $\delta^{13}C$ (Derry et al., 1992) and apparent high levels of ocean phosphate (Planavsky et al., 2010; Cook and Shergold, 1984), both of which point to high rates of organic carbon burial following deglaciation.

The work in this chapter provides a direct link between the termination of snowball glaciations and long term high-productivity periods. It is suggested that the persistence of rapid (i.e. above steady state) weathering rates over a $\sim 10^7$ year timescale in the snowball aftermath led to the high global nutrient concentration and organic burial rates recorded by proxies. Global abundance of nutrient may have assisted the diversification of biota surviving the snowball event, and oxygen concentration would be expected to rise during these periods, however the model used does not include dynamic representation of oxygen: the Phanerozoic-based equations break down at the low O_2 concentrations predicted during extreme glaciation. Assuming the snowball Earth - transport limitation scenario, the expected oxygen concentration throughout the Neoproterozoic would be oscillatory, rather than the step change inferred from proxies (Scott et al., 2008). A further mechanism is required to explain the apparent system shift from the low-O_2 Proterozoic

to the high-O_2 Phanerozoic (e.g. Lenton and Watson (2004)).

Broadly speaking, the results from this chapter support the existence of a link between deep glaciation and long-term oxidation. A period of $\sim 10^7$ years of increased oxygen concentration is predicted to follow a snowball Earth event. A sequence of glaciations with a similar timing to those in the Neoproterozoic appears in the geological record between 2.4-2.1Ga, and appears to contain at least one low-latitude event (Papineau, 2010; Evans et al., 1997; Bekker et al., 2001). These glaciations are synchronous with Paleoproterozoic oxygenation and have been linked to oxygen rise through increased delivery of nutrients during regional postglacial thawing (Papineau et al., 2007) or during a possible snowball aftermath (Harada et al., 2012). A long 200Myr positive carbon isotope excursion is seen following the glacial period (Karhu and Holland, 1996), and a shorter 50Myr excursion appears to follow the final glaciation (Bekker et al., 2006). The findings in this chapter would imply a long period of oxygenation following the proposed snowball event, and would suggest a carbon isotope signal similar to the 50Myr peak described by Bekker et al. (2006). However, timing of the Paleoproterozoic low latitude glaciation is disputed (Kopp et al., 2005; Hilburn et al., 2005) and more detail is required for full analysis of the implications of the transport limitation mechanism. A further limitation is the likely differences between the early and late Proterozoic carbon cycles (Hayes and Waldbauer, 2006), making application of the current Phanerozoic-based model difficult.

Here it is shown that the existence of a global weathering rate limit may explain how the Earth operates under extreme conditions. However, a detailed understanding of the mechanics of the silicate weathering process is still missing from the models considered in this thesis, the weathering process can be limited by a combination of local kinetic and tectonic factors (Riebe et al., 2004; West et al., 2005; Millot et al., 2002; West, 2008), which makes extrapolation to the global scale difficult.

5 A model for CO_2 and O_2 over the Proterozoic

5.1 Introduction

The simple biogeochemical models explored in this thesis have proved useful for examining Phanerozoic climate, and whilst they function tolerably well to investigate mechanisms controlling carbon dioxide and temperature in the Neoproterozoic, atmospheric oxygen predictions for this time are not consistent with data. Oxygen concentration over the Proterozoic is presumed to have been between 10^{-1} and 10^{-2} PAL (see section 3.2), but there are is no consensus as to whether this was a generally stable concentration or if there was a continuous rise or decline during this period (Kump, 2008; Canfield, 2005). Changes in carbon and sulphur cycling on the timescale of 10^9 years may have exerted various controls on oxygen concentration during this time that are not represented in current Phanerozoic models (Hayes and Waldbauer, 2006).

The rise in oxygen during the Neoproterozoic is becoming well constrained but is still poorly understood (Shields-Zhou and Och, 2011), there have been many suggested causes (e.g. Lenton and Watson (2004); Kennedy et al. (2006)) but no firm agreement on the dominating processes or specific characteristics. In this chapter the Minimal Model is expanded to include long term processes between the crust and mantle, with the intention of investigating both climate and atmospheric oxygen concentration over the last 2Ga.

5.2 Modelling interactions of the mantle with the surface system

In addition to the cycling of carbon and sulphur through the crust, oceans and atmosphere, longer term 'deep' cycles exists between the entire surface system and the mantle (Walter et al., 2011; Schidlowski, 1989). Oceanic crust is continually exported deep into the mantle at subduction zones (van der Hilst et al., 1997), and carbon is transferred from the mantle to the surface at mid ocean ridges and spreading centres (Saal et al., 2002; Resing et al., 2004),

accompanied by significant fluxes of iron and sulphur species (Elderfield and Schultz, 1996; Des Marais, 1997).

5.2.1 Ocean crust carbonatization and long term CO_2 stability

The model of Sleep and Zahnle (2001) adds the mantle cycle for carbon to a simple geochemical system similar to the GEOCARB and COPSE models. The paper discusses what is potentially a very important stabilising mechanism in the long term cycle - seafloor basalt carbonatization (Francois and Walker, 1992; Caldeira, 1995). In the terrestrial carbon cycle, the silicate weathering mechanism acts to stabilise atmospheric CO_2 concentration by transferring carbon from the hydrosphere to the crust (Walker et al., 1981) and the assumed changes to the weathering process over time drive current predictions for Phanerozoic CO_2 concentration (see chapter 2). Hydrothermal carbonatization of basalts (hereafter ocean crust carbonatization (OCC)) occurs when warm seawater flows through the oceanic crust , allowing transfer of carbon from the ocean into the crust, and may be responsible for production of carbonate veins and disseminated carbonate found in drilling exercises (Alt and Teagle, 1999).

Sleep and Zahnle argue for a dependence of this process on ocean CO_2 concentration that could perhaps be as strong as linear (i.e. $F_{OCC} \propto RCO_2$) if reactions were fast and allowed a superabundance of cations (Francois and Walker, 1992). However experimental evidence places a much weaker dependence on this, the laboratory data of Brady and Gislason (1997) suggests that $F_{OCC} \propto (RCO_2)^{0.23}$. Assuming some dependence on CO_2 concentration allows the OCC sink to have negative feedback on hydrospheric concentration in a very similar way to the silicate weathering flux, providing an additional stabilising mechanism for the carbon cycle. Note that the high temperature reaction with fresh mid ocean ridge basalts (MORBs) results in CO_2 input to the ocean rather than a sink (Su and Langmuir, 2003; Saal et al., 2002; Hayes and Waldbauer, 2006).

Figure 5.2.1 shows the CO_2 predictions for Sleep and Zahnle's model with respect to parameters α and β, here α is the assumed dependence of OCC on CO_2 concentration and β is the dependence of terrestrial silicate weathering on CO_2 (again following a power-law dependence). Higher values of α result

in lower predictions for atmospheric CO_2 in the Precambrian, as would be expected due to a stronger negative feedback.

The OCC rate is assumed to scale with the rate of creation of warm crust (see equation 12 in Sleep and Zahnle (2001)), which has declined over time (Franck et al., 1999), therefore the feedback on CO_2 via this mechanism would be expected to be stronger in the Precambrian than the Phanerozoic. It can been seen in figure 5.2.1 that different choices for α produce model predictions that correlate well for the Phanerozoic, but diverge further back in time. The results here give a CO_2 range of 20-40 PAL at 900Ma when vascular plant enhancement is considered, very similar to the predictions of the Minimal Model in this thesis ($\sim$ 30PAL at 900Ma). It is found that maintaining a warm climate further back in Earth history is possible in this model, but requires low choices for both α and β.

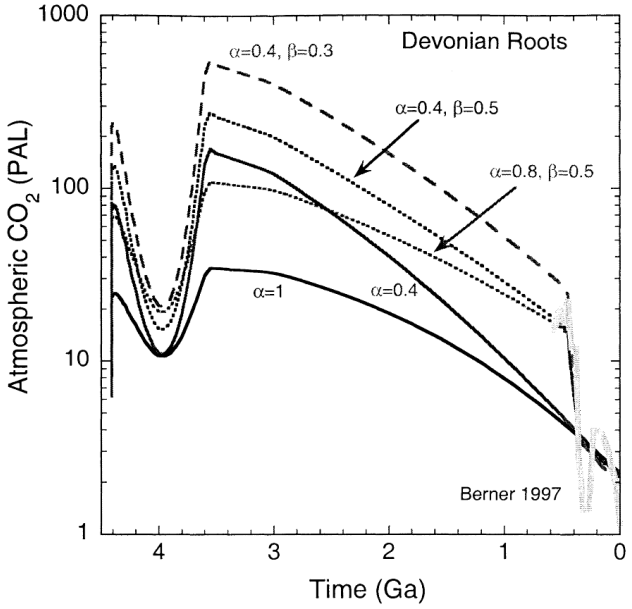

Figure 5.2.1: Atmospheric CO_2 histories from the model of Sleep and Zahnle (2001). Here α shows the dependence of OCC on CO_2 concentration and β shows the dependence of silicate weathering on CO_2. Solid lines show solution when enhancement of terrestrial weathering by vascular plants is not considered, dashed and dotted lines show solutions where enhancement by vascular plants is permitted. Grey line for the Phanerozoic shows results of the GEOCARB model. Copied directly from Sleep and Zahnle (2001) (fig 12a).

5.2.2 Carbon dioxide input at mid ocean ridges, the mantle CO_2 cycle, and the growth of the crustal carbon reservoir

Clarification of the input flux of CO_2 at mid ocean ridges (Saal et al., 2002; Resing et al., 2004) has recently allowed for a detailed model of the surface-mantle carbon cycle over the last 4Ga, which allows for a reconstruction of crustal carbon accumulation (Hayes and Waldbauer, 2006). The authors scale mantle CO_2 input to the high temperature heat flow at spreading centres (Lowell and Keller, 2003; Sleep and Zahnle, 2001) and fluxes into the mantle are calculated from the difference between subduction trench input (Holser et al., 1988; Bach and Edwards, 2003) and volatile emissions (Hilton et al., 2002). Figure 5.2.2a shows the estimated time-dependant flux of CO_2 from mid-ocean ridges alongside the crustal carbon content.

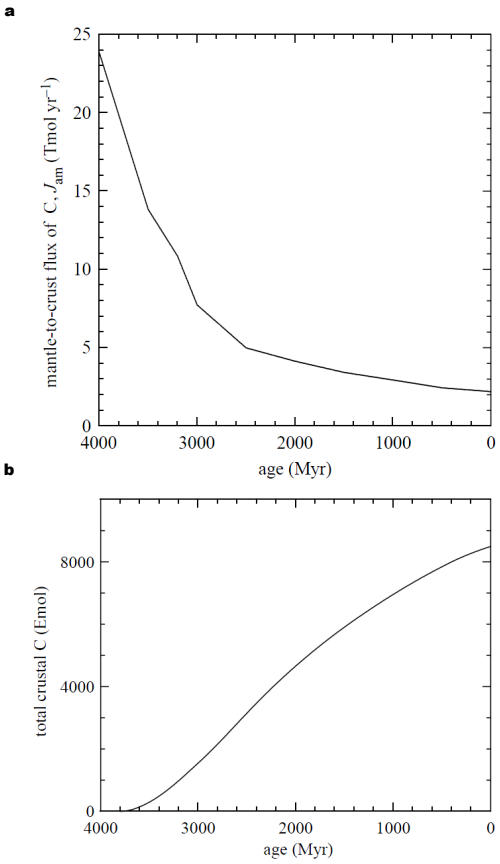

Figure 5.2.2: Model results from Hayes and Waldbauer (2006). **a**. Mantle-to-crust flux of carbon. **b**. Total crustal carbon. Both figures copied from Hayes and Waldbauer (2006)

Growth of the crustal reservoir occurs because the CO_2 input flux exceeds the export flux of crustal carbon to the mantle. Growth is fastest in early Earth history and declines as mantle heat flow decreases. The overall redox balance of the system requires that the build-up of reduced crustal carbon is coupled with oxygenation of some other species, and the authors suggest this may have been represented by ferric iron being subducted to the mantle (based on a maximum increase in mantle oxygen fugacity of 0.3 log units over the last 3.5Ga (Li and Lee, 2004)). By combining this model carbon cycle with an organic burial fraction derived from the carbon isotope record (Hayes et al., 1999; Melezhik et al., 1999) it is possible to estimate the history of the crustal organic carbon reservoir (see figure 9 in Hayes and Waldbauer (2006)), but the model does not feature a dynamic oxygen reservoir and so does not provide predictions for atmospheric O_2.

5.3 Model development

The Minimal Model is now expanded following the treatments described above. Figure 5.3.3 shows a cartoon of the processes involved, figure 5.3.4 shows a more practical (though thoroughly less inspiring) flux diagram.

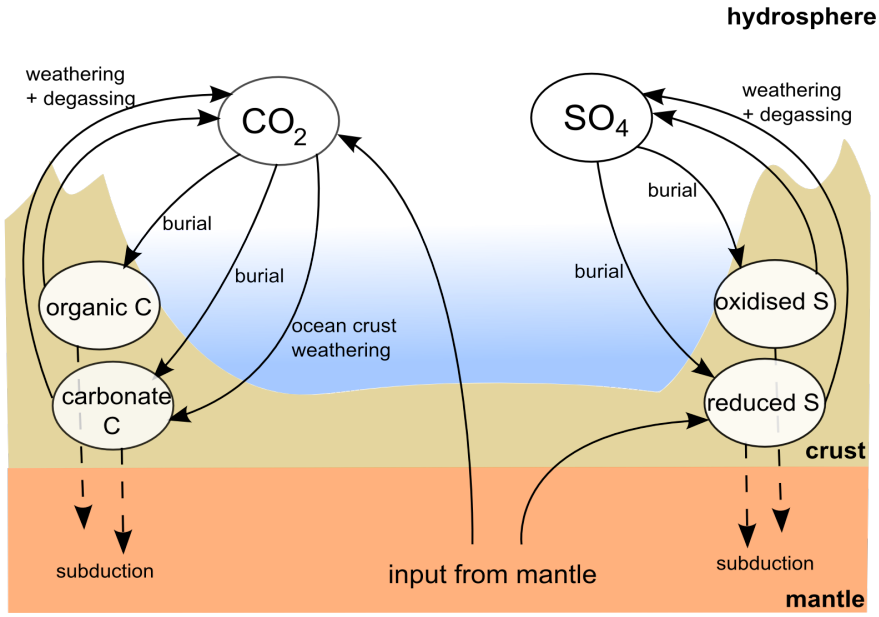

Figure 5.3.3: Cartoon of Mantle Model. Bubbles show model reservoirs, arrows represent fluxes, dashed arrows show subduction fluxes.

The nutrient system from COPSE is used to estimate productivity to allow prediction of isotope fractionation and organic burial rates based on the other model variables. The global temperature function follows the RCM approximation described in the previous chapter (Mills et al., 2011).

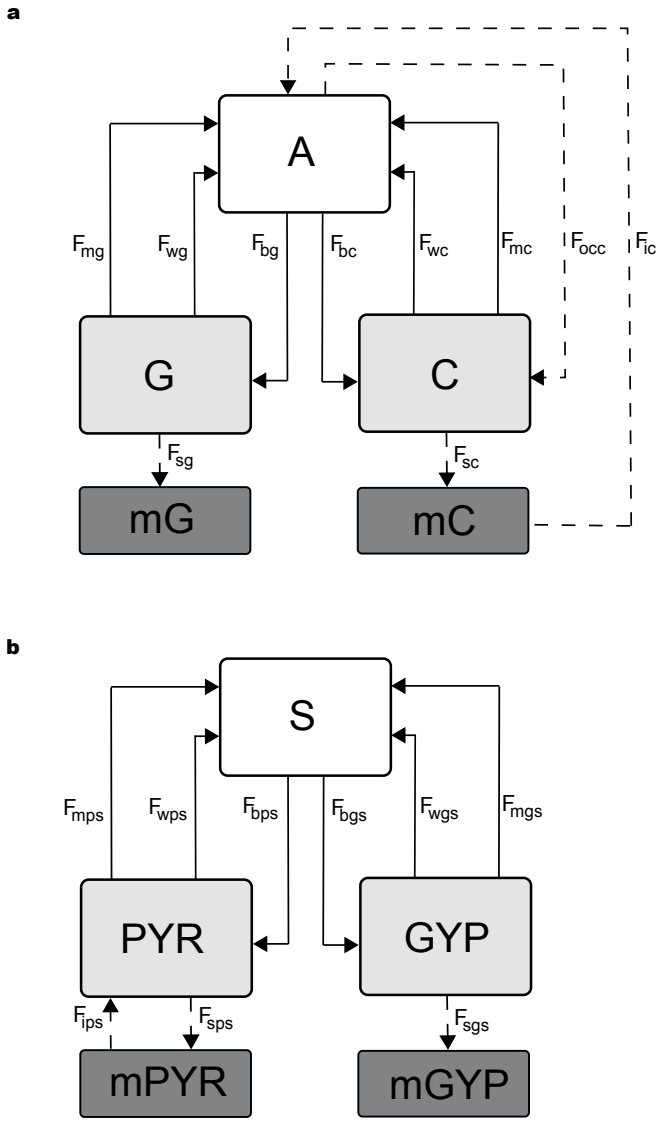

Figure 5.3.4: Schematic diagram of Mantle Model fluxes.F_w represents a weathering flux, F_m represents a metamorphic/degassing flux, F_b shows a burial flux, F_s shows a subduction flux, F_i is a mantle input flux and F_{occ} is the ocean crust carbonatization flux.

In addition to the Minimal Model fluxes each crustal reservoir is assumed to undergo subduction to mantle, the ocean crust carbonatization sink is assumed to transfer CO_2 from the ocean/atmosphere box to the crust and the mantle is assumed to input both CO_2 and reduced sulphur. Sulphur input is modelled as pyrite in order to represent both the sulphur and iron fluxes observed at ridges (Elderfield and Schultz, 1996) and to fit with the previous model scheme. Throughout the remainder of this work I will refer to this as the 'Mantle Model', in order to compare to the previously developed 'Minimal Model'.

5.3.1 Model forcings

The intention is to run this model for the last 2Ga, therefore all the forcings described in the simple model must be defined for this period, along with any additional forcings required. The extended forcings for the Mantle Model are shown in figure 5.3.5, panels **a** and **b** show forcings inherited from the Minimal Model, panel **c** shows new forcings.

The uplift (U), degassing (D) and solar (S) forcings are extended to 2Ga following their derivation in chapter 4. The uplift rate scales with the normalised seawater strontium curve of Shields (2005) and degassing rate scales with the spreading rate approximated by the square of the heat flow. Note the heat flow used to calculate the spreading rate follows the method used to approximate CO_2 input (Lowell and Keller, 2003; Sleep and Zahnle, 2001). Phanerozoic biological forcings for weathering enhancement (W), the C-P burial ratio on land (CPland), burial depth of carbonates (B) and evolution of plant-environment feedbacks (E) require no extension beyond the Phanerozoic and are copied directly from COPSE (Bergman et al., 2004).

The weathering enhancement related to the evolution of vascular plants is taken here as four-fold, following recent GEOCARB models (Berner, 2006a). Three new forcings are added: Q shows the mantle heat flow, and PW1, PW2 represent possible Precambrian weathering forcings that will be trialled in the model. For simplicity, and because of the Precambrian focus of the model, the Q forcing is not altered in the Phanerozoic using sea level inversion data (Gaffin, 1987) as might be attempted (i.e. $Q \approx \sqrt{D}$).

PW1 shows an assumed enhancement to terrestrial weathering kinetics

during the late Neoproterozoic due to continental dispersal, prevalence of masses land at low latitudes, and increased area of basaltic provinces (Goddéris et al., 2003; Donnadieu et al., 2004; Li et al., 2008), the magnitude of this forcing follows Mills et al. (2011) and the work in chapter 3.

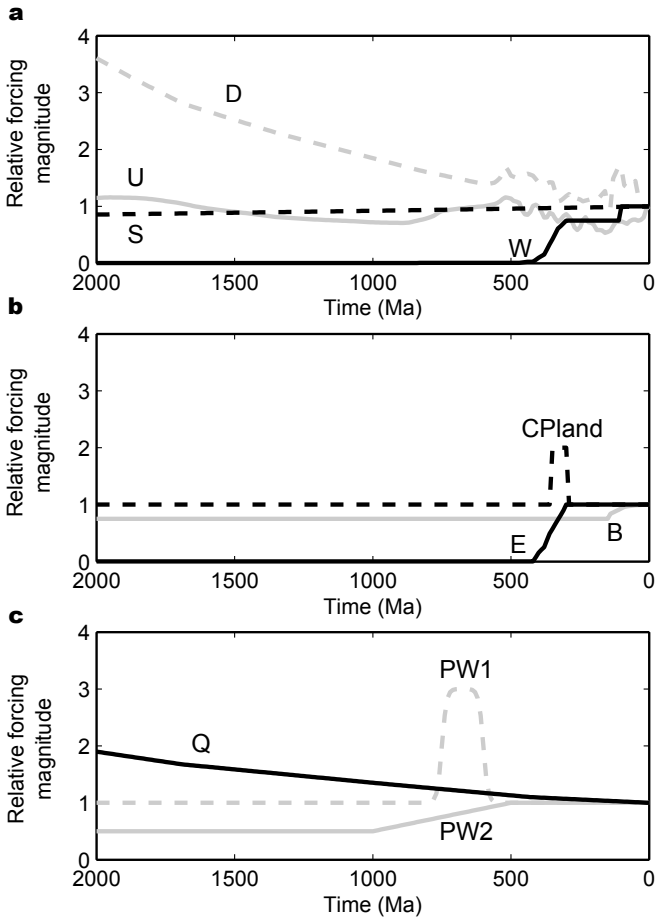

Figure 5.3.5: Mantle Model forcings. a,b. Forcings from the simple model extended to 2Ga, W = weathering enhancement due to plant evolution, U = uplift, D = degassing, S = relative solar constant, CPland = C-P burial ratio on land, E = evolution of land plant climate feedbacks, B = burial depth of carbonates. **c**. Additional forcings for Mantle Model. PW1 = possible Neoproterozoic weathering efficiency increase, PW2 = possible change in biological weathering enhancement from early land colonisation, Q = relative mantle heat flux.

The PW2 forcing is based on the likely enhancement of weathering due to the radiation of simple organisms on the land surface during the Neoproterozoic (Heckman et al., 2001; Kennedy et al., 2006). Evidence for microbial

structures in dry regions is found as early as 1200-1000Ma (Prave, 2002; Horodyski and Knauth, 1994), fossilised plant spores appear at $\sim$ 470Ma (Rubinstein et al., 2010; Wellman and Gray, 2000) and the earliest recorded land plant fragments are seen in the 460-450Ma Caradoc period (Wellman et al., 2003). These findings all predate the biotic weathering enhancements used in the COPSE and GEOCARB models and clearly require some representation in a long term model, especially given the power of biotic forcings in current models (Berner, 1997). Land biota mechanically stabilizes soil profiles and increases fluid residence time (Retallack, 2001) and recent microcosm experiments using mosses have shown that non-vascular plants can considerably enhance silicate weathering over background abiotic levels (Lenton et al., 2012). These experiments produce enhancement factors for Ca and Mg removal of $\sim$ 1.5 times on a granite substrate, and 3.6 (Ca) and 5.4 (Mg) times on andesite. For this model the PW2 biotic forcing is taken to increase linearly over the period 1000-500Ma, representing a two-fold weathering enhancement between the completely abiotic state and the pre-vascular stage.

5.3.2 Additional flux calculations

The following additional fluxes are defined for the Mantle Model. The naming of fluxes corresponds to the schematic diagram in figure 5.3.4.

Ocean crust carbonatization (OCC)

Following Sleep and Zahnle (2001), the flux of ocean crust carbonatization (F_{occ}) is allowed a dependence on CO_2 concentration with a power law relationship denoted by α, and a dependence on the spreading rate, which is taken as the square of the heat flux Q (see equation 3.5.3).

$$F_{occ} = k_{occ} \cdot Q^2 \cdot \left(\frac{RCO_2}{RCO_2(0)} \right)^{\alpha} \tag{5.3.1}$$

where $k_{occ} = 1.65 \times 10^{12}$ mol/yr is the present day rate (Sleep and Zahnle, 2001; Elderfield and Schultz, 1996).

Mantle inputs

The expression for the mantle input of CO_2 follows Hayes and Waldbauer (2006), assuming a present day input rate of $k_{ic} = 2.2 \times 10^{12}$ mol/yr and

scaling with the mantle heat flux.

$$F_{ic} = k_{ic} \cdot Q \tag{5.3.2}$$

Input of iron and reduced sulphur at mid ocean ridges is modelled as pyrite and added to the crustal pyrite reservoir. This treatment is intended to represent sulphide delivered to the surface as magmatic-hydrothermal ores (Seo et al., 2009; Gustafson and Hunt, 1975), and the input rate is assumed to scale with the rate of generation of new crust, Q^2.

$$F_{ips} = k_{ips} \cdot Q^2 \tag{5.3.3}$$

here k_{ips} is the present day rate. Estimated values for Fe input are $0.23 - 1.9 \times 10^{11}$ mol/yr and reduced S input of $0.95 - 9.6 \times 10^{11}$ mol/yr (Elderfield and Schultz, 1996). The value of k_{ips} is calculated for system stability and based on these limits.

Subduction fluxes

Rates of subduction to the mantle are assumed to be proportional to the size of the crustal reservoir and to the global spreading rate:

$$F_{sg} = k_{sg} \cdot Q^2 \cdot \left(\frac{\mathbf{G}}{\mathbf{G_0}}\right), F_{sc} = k_{sc} \cdot Q^2 \cdot \left(\frac{\mathbf{C}}{\mathbf{C_0}}\right), \tag{5.3.4}$$

$$F_{sps} = k_{sps} \cdot Q^2 \cdot \left(\frac{\mathbf{PYR}}{\mathbf{PYR_0}}\right), F_{sgs} = k_{sgs} \cdot Q^2 \cdot \left(\frac{\mathbf{GYP}}{\mathbf{GYP_0}}\right) \tag{5.3.5}$$

assuming a present day rate of loss of C to the mantle of 1.2×10^{12} mol/yr (Hayes and Waldbauer, 2006), dividing according to the mass of the crustal reservoirs gives $k_{sc} = 1.02 \times 10^{12}$ mol/yr, $k_{sg} = 1.8 \times 10^{11}$ mol/yr. Annual loss of pyrite sulphur to the mantle is $k_{sps} = 3.6 \times 10^{11}$ mol/yr (Canfield, 2004), assuming the same fraction of total oxidised sulphur is lost gives $k_{sgs} = 4 \times 10^{11}$.

5.3.3 Peresnt day steady state calculation

In the COPSE and GEOCARB models, unknown fluxes are calculated such that the ocean/atmosphere and crustal reservoirs preserve steady state at present day. A less powerful constraint is applied in this work. It is assumed

that the atmosphere/ocean reservoirs of oxygen, carbon dioxide and sulphate are at steady state at present day, but the crustal reservoirs are not forced to be steady. The size of the mantle reservoirs is not calculated in this model, as none of the mantle fluxes depend on these values.

Using the constants from the previous model and the newly defined fluxes, assuming steady state at present day with respect to oxygen yields:

$$k_{wg} = k_{bg} - k_{mg} + (15/8) * (k_{bps} - k_{wps} - k_{mps}) = 7 \times 10^{12} \text{mol/yr} \quad (5.3.6)$$

Assuming steady state for present day ocean/atmosphere CO_2 results in:

$$k_{bc} = k_{wg} + k_{mg} + k_{wc} + k_{mc} + k_{ic} - k_{bg} - k_{occ} = 1.98 \times 10^{13} \text{mol/yr} \quad (5.3.7)$$

For the sulphur cycle, the present day burial rates of oxidised and reduced sulphur are defined and the rates of weathering are calculated for stability. For simplicity, it is assumed that total rate of sulphur loss to the mantle is equal to the sulphur input rate, i.e:

$$k_{ips} = k_{sps} + k_{sgs} = 7.6 \times 10^{11} \text{mol/yr} \quad (5.3.8)$$

This value for S input is close to the maximum value of 9.6×10^{11} mol/yr proposed in Elderfield and Schultz (1996), whilst the assumed Fe input of 3.8×10^{11}mol/yr is double the value suggested in the same paper. However, similar global iron input has been estimated by other authors (e.g. 3×10^{11} mol/yr (Holland, 2006)). Estimates for the present day rate of pyrite burial range from $0.53 - 1.87 \times 10^{12}$ mol/yr (Kump and Garrels, 1986; Bottrell and Newton, 2006; Arvidson et al., 2006), an average estimate of $k_{bps} = 1 \times 10^{12}$mol/yr is taken. Following COPSE and GEOCARB gypsum burial is assumed to be double this, i.e. $k_{bgs} = 2 \times 10^{12}$mol/yr. This gives a total S burial rate of 3×10^{12}mol/yr which is roughly equivalent to the total continental S weathering flux calculated in Bottrell and Newton (2006). Degassing fluxes are taken from GEOCARB, giving $k_{mps} = 0.25 \times 10^{12}$mol/yr and $k_{mgs} = 0.5 \times 10^{12}$mol/yr. The equation for stability of ocean sulphate then gives:

$$k_{wgs} = k_{sgs} - k_{mgs} + k_{bgs} = 1.1 \times 10^{11} \text{mol/yr} \tag{5.3.9}$$

$$k_{wps} = k_{bps} - k_{mgs} + k_{sgs} = 1.15 \times 10^{12} \text{mol/yr} \tag{5.3.10}$$

These derived wetahering rates fall between previous estimates (k_{wps}: $0.53 - 1.79 \times 10^{12}$ mol/yr (Arvidson et al., 2006; Kump and Garrels, 1986), k_{wgs}: $1 - 2 \times 10^{12}$ mol/yr (Berner, 1994)) and follow previous models by assuming steady state of the present day sulphur cycle.

5.3.4 Carbon and sulphur isotope fractionation

As in the simplified Neoproterozoic model, the isotopic fractionation of the carbon and sulphur reservoirs is calculated at each timestep. Here a different method is used to improve computational efficiency, instead of explicitly calculating the number of moles of each isotope, the model calculates the size of the reservoir multiplied by its δ^{13}C (for carbon) or δ^{34}S (for sulphur) value (i.e. for the ocean and atmosphere carbon reservoir, $\mathbf{A}$, we require $\mathbf{A} \times \delta^{13}\text{C}(\mathbf{A})$). This new quantity is then divided by the reservoir size to obtain results for isotope fractionation. The treatment here follows from the GEOCARB models (Berner, 2006a, 2009) with the difference that δ^{13}C and δ^{34}S are predicted rather than used as input.

Hypothesised fractionation effects will be tested in this model using an ensemble of runs: a constant fractionation effect upon organic burial of carbon and sulphur, a variable fractionation during marine carbonate burial (Bergman et al., 2004; Mills et al., 2011), a constant fractionation effect during ocean crust carbonatization (Bjerrum and Canfield, 2004) and a oxygen-dependent fractionation effect associated with pyrite burial (Berner, 2001).

5.3.5 Starting values for 2Ga

This system has many negative feedback mechanisms that regulate the size of the ocean and atmosphere reservoirs on a timescale of the order 10^6 years. If the starting concentrations for the atmosphere/ocean species are altered, the model stabilizes within a (typically < 100Myr) spin-up period. To ensure the system is started from a stable state the model is run twice. The 'spun

up' reservoir sizes for the current parameter configuration are obtained on the first run, which begins at present day reservoir concentrations, the final run is then initiated with these as the starting values. The first 100Ma of model runs are not shown in the figures (model is initiated at 2.1Ga to return predictions for 0-2Ga). The size of the crustal carbon reservoirs is expected to rise over time, it is found that recovery of present day values requires G $= 0.65G_0$ and C $= 0.65C_0$ at 2.1Ga. In the model of Hayes and Waldbauer the total crustal carbon at 2.1Ga is ~ 0.6 times present day.

5.3.6 Full model equations

The Mantle Model system is laid out mathematically in the following tables:

Name	Equation
Phosphate	$\frac{\mathrm{d}P}{\mathrm{d}t} = psea - mopb - capb - fepb$
Oxygen	$\frac{\mathrm{d}O}{\mathrm{d}t} = \mathrm{F_{bg}} - \mathrm{F_{wg}} - \mathrm{F_{mg}} + \frac{15}{8}\left(\mathrm{F_{bps}} - \mathrm{F_{wps}} - \mathrm{F_{mps}}\right)$
Atmosphere/ocean CO_2	$\frac{\mathrm{d}A}{\mathrm{d}t} = -\mathrm{F_{bg}} + \mathrm{F_{wg}} + \mathrm{F_{wc}} + \mathrm{F_{mg}} + \mathrm{F_{mc}} - \mathrm{F_{bc}} - \mathrm{F_{occ}} + \mathrm{F_{ic}}$
Ocean sulphate	$\frac{\mathrm{d}S}{\mathrm{d}t} = \mathrm{F_{wgs}} + \mathrm{F_{wps}} - \mathrm{F_{bgs}} - \mathrm{F_{bps}} + \mathrm{F_{mgs}} + \mathrm{F_{mps}}$
Buried organic carbon	$\frac{\mathrm{d}G}{\mathrm{d}t} = \mathrm{F_{bg}} - \mathrm{F_{wg}} - \mathrm{F_{mg}} - \mathrm{F_{sg}}$
Buried carbonate carbon	$\frac{\mathrm{d}C}{\mathrm{d}t} = \mathrm{F_{bc}} + \mathrm{F_{occ}} - \mathrm{F_{wc}} - \mathrm{F_{mc}} - \mathrm{F_{sc}}$
Buried pyrite sulphur	$\frac{\mathrm{d}PYR}{\mathrm{d}t} = \mathrm{F_{bps}} + \mathrm{F_{ips}} - \mathrm{F_{wps}} - \mathrm{F_{mps}} - \mathrm{F_{sps}}$
Buried gypsum sulphur	$\frac{\mathrm{d}GYP}{\mathrm{d}t} = \mathrm{F_{bgs}} - \mathrm{F_{wgs}} - \mathrm{F_{mgs}} - \mathrm{F_{sgs}}$

Table 9: Reservoir calculations for Mantle Model

Name	Meaning
U	Relative global uplift rate
D	Relative global degassing rate
S	Solar forcing
W	Weathering enhancement in the Phanerzoic due to vascular plant evolution
$PW1$	Weathering enhancement in the late Neoproterozoic due to continental configuration
$PW2$	Weathering enhancement across the Neoproterozoic due to land colonisation
Q	Relative mantle heat flux
CP_{land}	Carbon-to-phosphorus burial ratio increase during the Permo-Carboniferous
B	Increased carbonate degassing in the Mesozoic due to burial of calcareous plankton

Table 10: Model forcings

Name	**Shorthand**	**Equation**
Nutrient weathering	$phosw$	$k_{\text{phosw}}\left(\frac{2}{12}\frac{silw}{silw_0}+\frac{5}{12}\frac{carbw}{carbw_0}+\frac{5}{12}\frac{oxidw}{oxidw_0}\right)$
Silicate weathering	$silw$	$k_{\text{silw}}U\cdot W\cdot PW1\cdot PW2$ $\times e^{\left(k_{sil1}\frac{T-T_0}{TT_0}\right)}\left(e^{k_2(T-T_0)}\right)^{0.65}\sqrt{\text{RCO}_2}$
Carbonate weathering	F_{wc}	$k_{\text{wc}}U\cdot W\cdot PW1\cdot PW2\cdot e^{k_{carb1}(T-T_0)}\sqrt{\text{RCO}_2}$
Oxidative weathering	F_{wg}	$k_{\text{wg}}U\sqrt{\text{RO}_2}\left(\frac{\mathbf{G}}{\mathbf{G}_0}\right)$
Pyrite weathering	F_{wps}	$k_{\text{wps}}U\sqrt{\text{RO}_2}\left(\frac{\mathbf{PYR}}{\mathbf{PYR}_0}\right)$
Gypsum weathering	F_{wgs}	$k_{\text{wgs}}U\left(\frac{\mathbf{GYP}}{\mathbf{GYP}_0}\right)$
Ocean crust carbonatization	F_{occ}	$\text{k}_{\text{occ}}\cdot Q^2\cdot\left(\frac{\text{RCO}_2}{\text{RCO}_2(0)}\right)^{\alpha}$
Organic carbon degassing	F_{mg}	$k_{\text{mg}}D\left(\frac{\mathbf{G}}{\mathbf{G}_0}\right)$
Carbonate carbon degassing	F_{mc}	$k_{\text{mc}}D\cdot B\cdot\left(\frac{\mathbf{C}}{\mathbf{C}_0}\right)$
Pyrite sulphur degassing	F_{mps}	$k_{\text{mps}}D\left(\frac{\mathbf{PYR}}{\mathbf{PYR}_0}\right)$
Gypsum sulphur degassing	F_{mps}	$k_{\text{mps}}D\left(\frac{\mathbf{PYR}}{\mathbf{PYR}_0}\right)$
Carbonate carbon mantle input	F_{ic}	$k_{\text{ic}}Q$
Pyrite sulphur mantle input	F_{ips}	$k_{\text{ips}}Q^2$
Organic carbon subduction	F_{sg}	$k_{\text{sg}}Q^2\left(\frac{\mathbf{G}}{\mathbf{G}_0}\right)$
Carbonate carbon subduction	F_{sc}	$k_{\text{sc}}Q^2\left(\frac{\mathbf{C}}{\mathbf{C}_0}\right)$
Pyrite sulphur subduction	F_{sps}	$k_{\text{sps}}Q^2\left(\frac{\mathbf{PYR}}{\mathbf{PYR}_0}\right)$
Gypsum sulphur subduction	F_{sgs}	$k_{\text{sgs}}Q^2\left(\frac{\mathbf{GYP}}{\mathbf{GYP}_0}\right)$

Table 11: List of fluxes in Mantle Model

Name	**Shorthand**	**Equation**
Pyrite sulphur burial	$\mathrm{F_{bps}}$	$k_{\mathrm{bps}} \left(\frac{\mathbf{S}}{\mathbf{S}_0}\right) \frac{mocb}{mocb_0}$
Gypsum sulphur burial	$\mathrm{F_{bgs}}$	$k_{\mathrm{bgs}} \left(\frac{\mathbf{S}}{\mathbf{S}_0}\right)$
Marine carbonate carbon burial	$\mathrm{F_{bc}}$	$\mathrm{F_{wc}} + silw$
Marine organic carbon burial	$mocb$	$k_{\mathrm{mocb}} \left(\frac{P}{P_0}\right)^2$
Land organic carbon burial	$locb$	$k_{\mathrm{locb}} \frac{pland}{pland_0} \cdot CP_{land}$
Total organic carbon burial	$\mathrm{F_{bg}}$	$mocb + locb$
Marine organic phosphate burial	$mopb$	$\frac{mocb}{CPsea}$
Calcium-bound phosphate burial	$capb$	$k_2 \frac{mocb}{mocb_0}$
Iron-sorbed phosphate burial	$fepb$	$\frac{k_3}{k_4} \left(1 - anox\left(O, P\right)\right)$ where $anox = 1 - k_{oxfrac} \left(\frac{O}{O_0} \frac{P_0}{P}\right)$
P delivered to ocean	$psea$	$phosw - locb$

Table 12: List of fluxes in Mantle Model (continued)

Name	Meaning	Size	Source
k_{mocb}	Marine organic carbon burial	4.5×10^{12} mol C yr^{-1}	COPSE
k_{locb}	Land organic carbon burial	4.5×10^{12} mol C yr^{-1}	COPSE
k_{capb}	Ca associated phosphorus burial	1.5×10^{10} mol P yr^{-1}	COPSE
k_{fepb}	Fe associated phosphorus burial	6×10^{9} mol P yr^{-1}	COPSE
k_{bps}	Pyrite burial	1×10^{12} mol S yr^{-1}	average from Kump and Garrels (1986); Bottrell and Newton (2006); Arvidson et al. (2006)
k_{bgs}	Gypsum burial	2×10^{12} mol S yr^{-1}	relationship to k_{bps} (Berner, 2006a)
k_{bc}	Carbonate carbon burial	1.98×10^{13} mol S yr^{-1}	for steady state
k_{occ}	Ocean crust carbonatization	1.65×10^{12} mol C yr^{-1}	Sleep and Zahnle (2001)
k_{silw}	Silicate weathering	6.45×10^{12} mol C yr^{-1}	for steady state
k_{wc}	Carbonate weathering	1.335×10^{13} mol C yr^{-1}	COPSE
k_{wg}	Oxidative weathering	7×10^{12} mol C yr^{-1}	for steady state
k_{phosw}	Reactive phosphorus weathering	4.35×10^{10} mol P yr^{-1}	for steady state
k_{wps}	Pyrite weathering	1.15×10^{12} mol S yr^{-1}	for steady state
k_{wgs}	Gypsum weathering	1.1×10^{12} mol S yr^{-1}	for steady state
k_{mg}	Organic carbon degassing	1.25×10^{12} mol C yr^{-1}	COPSE
k_{mc}	Carbonate carbon degassing	6.65×10^{12} mol C yr^{-1}	COPSE
k_{mps}	Pyrite sulphur degassing	2.5×10^{11} mol S yr^{-1}	Berner (2006)
k_{mgs}	Gypsum sulphur degassing	5×10^{11} mol S yr^{-1}	Berner (2006)

Table 13: List of constants for Mantle Model.

Name	Meaning	Size	Source
k_{ic}	Mantle carbonate input	2.2×10^{12} mol C yr^{-1}	Hayes and Waldbauer (2006)
k_{ips}	Mantle pyrite input	7.6×10^{11} mol S yr^{-1}	for steady state
k_{sg}	Organic carbon subduction	1.8×10^{11} mol C yr^{-1}	analogy to Hayes and Waldbauer (2006)
k_{sc}	Carbonate carbon subduction	1.02×10^{12} mol C yr^{-1}	analogy to Hayes and Waldbauer (2006)
k_{sps}	Pyrite sulphur subduction	3.6×10^{11} mol S yr^{-1}	Canfield (2004)
k_{sgs}	Gypsum sulphur subduction	4×10^{11} mol S yr^{-1}	derived from Canfield (2004)
k_{oxfrac}	Initial oxic fraction	0.86	COPSE
$CPsea$	C:P burial ratio	250 mol:mol	COPSE
$pland$	fraction of phosphorus buried on land	0.10345	COPSE
k_{O2}	Constant for calculating O_2(atm) from oxygen reservoir	3.762	COPSE
P_0	Present day ocean phosphate	3.1×10^{15}mol	COPSE
O_0	Present day atmosphere/ocean O_2	3.7×10^{19} mol	COPSE
A_0	Present day atmosphere/ocean CO_2	3.193×10^{18} mol	COPSE
S_0	Present day ocean sulphate	4×10^{19} mol	COPSE
G_0	Present day crustal organic carbon	1.275×10^{21} mol	Hayes and Waldbauer (2006)
C_0	Present day crustal carbonate carbon	7.225×10^{21} mol	Hayes and Waldbauer (2006)
PYR_0	Present day crustal pyrite	1.8×10^{20} mol	COPSE
GYP_0	Present day crustal gypsum	2×10^{20} mol	COPSE

Table 14: List of constants for Mantle Model (continued).

5.4 Model results and comparison to previous study

The Mantle Model is now run from 2.1Ga to present. The model baseline is subject to the forcings U (Uplift rate), D (degassing rate), S (solar constant), W (weathering enhancement due to vascular plants), B (carbonate burial depth), CPsea (C-P burial ratio) and Q (mantle heat flow). The dependence on OCC rate on CO_2 for the baseline model is $\alpha = 0.23$ (Brady and Gislason, 1997), and additional weathering forcings PW1 and PW2 are not included. Figure 5.4.6 shows the Mantle Model predictions plotted against the predictions from the previous Minimal Model run for the same timeframe. Here the Minimal Model is subject to the same forcing set as the Mantle Model, aside from the heat flow forcing, which does not apply to any of the calculations in the Minimal Model.

Oxygen concentration is plotted against a range of proxy constraints from Goldblatt et al. (2006) (supplementary figure 1). This includes paleosol data (Rye and Holland, 1998), the assumed oxygen demands for fossil fauna (Runnegar, 1991; Canfield and Teske, 1996) and a lower limit for oxygen concentration when fossilised charcoal is found (Rowe and Jones, 2000). Phanerozoic proxy constraints for CO_2 are taken from Royer et al. (2004), with Precambrian constraints from the compilation of Kah and Riding (2007). The Precambrian proxies are derived from various methods which are denoted by upper case letters in the figures in which they appear.

The predictions from the Minimal Model (green) show a decreasing trend in oxygen and carbon dioxide concentration over the last 2Ga, following the trend shown when this model was run for 900-0Ma in chapter 3. Further back in time, the solar constant is reduced, which lowers surface temperature and therefore weathering efficiency. This requires higher CO_2 to stabilize the system via the silicate weathering feedback (Walker et al., 1981). The degassing rate continuously rises further back in time, requiring more CO_2 to be buried via weathering to stabilize the system, which requires a higher global weathering rate and therefore more CO_2 residing in the ocean/atmosphere box. Due to higher weathering rates, ocean nutrient concentration is predicted to exceed the present day concentration in the Paleoproterozoic, resulting in atmospheric oxygen concentration around present day levels at 2Ga.

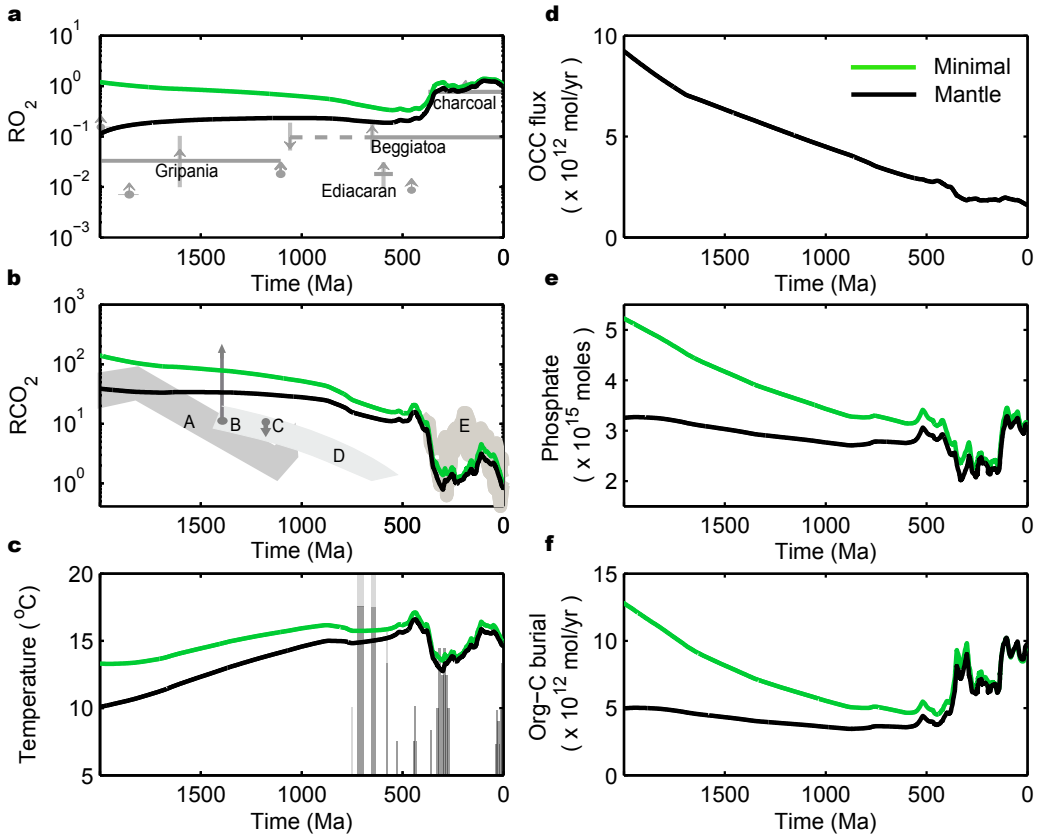

Figure 5.4.6: Mantle Model baseline compared to Minimal Model Mantle Model shown in black, simple model in green. **a**, relative atmospheric oxygen concentration. Paleosol data (Rye and Holland, 1998) are shown as grey circles with arrows to distinguish between a minimum or maximum estimate. Grey horizontal lines show assumed fanual requirements (Runnegar, 1991; Canfield and Teske, 1996), with the species name in black, 'charcoal' refers to the lower limit for oxygen required by the existence of fossil charcoal. Proxy figure from Goldblatt et al. (2006) **b**, relative ocean/atmosphere CO_2 concentration. Grey shaded areas represent estimates for CO_2 concentration from paleosol data (A) (Sheldon, 2006), carbon isotope modelling (D) (Kah and Bartley, 2004) and the Phanerozoic compilation of proxies (Royer et al., 2004). Grey circles with arrows show upper and lower bound estimates from composition of fossil acritarchs (B) (Kaufman and Xiao, 2003) and cyanobacteria (C) (Kah and Riding, 2007). **c**, average global surface temperature plotted against the glacial record from this work (where the positive y axis indicates more severe glaciation). **d**, ocean crust carbonatization flux. **e**, ocean phosphate reservoir. **f** rate of burial of organic carbon. Original in colour.

Results for the Mantle Model (black) show a notable response to the additional processes included, differing considerably from the Minimal Model. The ocean crust carbonatization flux provides an additional sink for CO_2, and because the rate of carbon removal is linked to the spreading rate, the sink becomes more powerful further back in time. A larger carbon sink in the ocean acts to counter the higher CO_2 degassing rate, requiring less removal of carbon by terrestrial silicate weathering. Predictions for CO_2 from the Mantle Model fit well with proxies for the Paleoproterozoic but do not replicate the expected low CO_2 and temperature in the Neoproterozoic.

In the Minimal Model, high global weathering rates in the Precambrian result in ocean nutrient concentration markedly higher than present day and result in prediction of high oxygen concentration (0.25-1 PAL) over the Proterozoic. In the Mantle Model, CO_2 removal via OCC results in lower rates of terrestrial weathering and less nutrient is delivered to the surface ocean. The Mantle Model predicts a fairly stable nutrient concentration through the Proterozoic, at levels close to the present day. The resulting oxygen prediction is 0.1-0.2PAL for the period 2000-400Ma. Stability of Proterozoic O_2 and CO_2 is a result of the dependence of both the degassing rate and OCC rate on the global spreading rate. A higher degassing rate requires that more carbon be buried to stabilise the system, resulting in the high-O_2 solution in the Minimal Model. In the Mantle Model, an equally enhanced OCC rate provides a sink for the additional carbon which does not require elevated productivity.

The oxygen prediction from the Minimal Model does not violate the majority of the proxy data shown in figure 5.4.6**a**, but there is no evidence for oxic deep oceans until the Neoproterozoic (Canfield et al., 2008), and this would be expected under present day oxygen concentration. Furthermore, carrying on the trend of increasing heat flow further back in time would indicate higher than present day oxygen concentrations for the Archean. It is agreed from multiple lines of evidence that before the great oxidation event at around 2.4Ga the concentration of atmospheric oxygen must have been several orders of magnitude lower than at present day (Holland, 2006; Farquhar et al., 2000). Oxygen predictions from the Mantle Model baseline fall within the 0.01-0.2 PAL window that is considered compatible with the majority of proxies (Canfield, 2005; Kump, 2008).

Resolving temperature predictions from the current model is difficult. In the early Proterozoic the CO_2 predictions line up well with proxy data (Kah and Riding, 2007), however the predicted global temperature would imply global glaciation, for which there is no evidence after 2.1Ga (Kirschvink et al., 2000). Previous modelling has also shown these low CO_2 estimates to be difficult to reconcile with temperate climate (Kasting, 1987). It has been suggested that an increased atmospheric methane inventory may account for the additional required warming in the Proterozoic, a mechanism that is plausible considering the assumed low oxygen concentration and likely enhanced anaerobic productivity (Kah and Riding, 2007; Pavlov et al., 2003). In the model runs shown there is no consideration of the Neoproterozoic continental breakup episode and resulting temperature and CO_2 predictions for the Neoproterozoic are higher than suggested by both CO_2 and glacial proxies

5.5 Effect of the strength of the OCC-CO_2 feedback

The additional ocean crust carbonatization (OCC) sink for CO_2 has a dramatic effect on how we might interpret the Proterozoic Earth system relative to the Phanerozoic. In the Mantle Model, the strength of the OCC flux is related to CO_2 concentration using the α parameter: $F_{OCC} \propto (RCO_2)^{\alpha}$ (in the baseline results above, $\alpha = 0.23$ (Brady and Gislason, 1997), but this value is extremely difficult to measure, and in reality the process is much more complex than a simple power law relationship (Sleep and Zahnle, 2001) and requires further study). It is likely that the OCC flux may constitute perhaps a much weaker, or stronger feedback on CO_2 than current estimates. Figure 5.5.7 shows the results of allowing different values of α in the Mantle Model.

Allowing $\alpha = 0.4$ (blue lines) strengthens the relationship between CO_2 concentration and OCC rate. Because Proterozoic CO_2 concentrations are predicted to be significantly higher than present day, a larger value for α results in a generally more powerful OCC flux, as in the model of Sleep and Zahnle (2001). With OCC removing a larger fraction of ocean/atmosphere carbon, colder temperatures are predicted than the baseline model, and less of the total carbon burial occurs via terrestrial weathering. In the Mantle

Model this results in predictions for lower nutrient and oxygen concentrations throughout the Proterozoic. The ocean phosphate reservoir is predicted by the model to be around 80% of the present day size at 2Ga, somewhat higher than the 10-25% suggested by an analysis of the phosphorus and iron content of banded iron formations from this time (Bjerrum and Canfield, 2002). Oxygen concentration for this run is predicted to rise from 0.03PAL to 0.2PAL over the proterozoic as terrestrial weathering begins to take over from OCC as the dominant carbon removal pathway, coupled with a decrease in the input rate of reduced sulphur and iron, which scales with Q^2. Choosing $\alpha > 0.4$ would imply lower rates of terrestrial weathering, nutrient delievery and oxygen production, especially in the Paleoproterozoic where the OCC flux is stronger. However, oxygen concentration below 10^{-3} causes the model to break down under these circumstances.

When α is set to zero (red line), the OCC flux is no longer dependent on carbon dioxide concentration and is therefore a much weaker sink for CO_2 throughout the model run. The results become closer to the predictions of the Minimal Model (fig 5.4.6), as the silicate weathering flux is responsible for the majority of carbon burial. However, oxygen is relatively stable throughout the Proterozoic and < 0.4PAL, offering a better fit to proxy data than the Minimal Model. Higher CO_2 and temperature in the $\alpha = 0$ case show a more plausible link to the lack of glaciation between 2-1Ga, however predicted global temperature is still lower than would be expected for a ice-free world.

As in the model of Sleep and Zahnle (2001) the sensitivity analysis with respect to α gives CO_2 predictions that noticeably diverge around 500Ma, and are dramatically different by 2Ga. Paleoproterozoic CO_2 predictions from the Mantle Model are somewhat lower than in the model of Sleep and Zahnle for the same value of α, one reason for this is that the authors of the study assume a more conservative weathering enhancement due to vascular plants, which leads to stronger terrestrial weathering fluxes before their evolution than in the Mantle Model. Additionally, the Mantle Model includes a more complex treatment of runoff and uplift rates, which both act to increase the predicted weathering rates, meaning that less CO_2 is required for steady state.

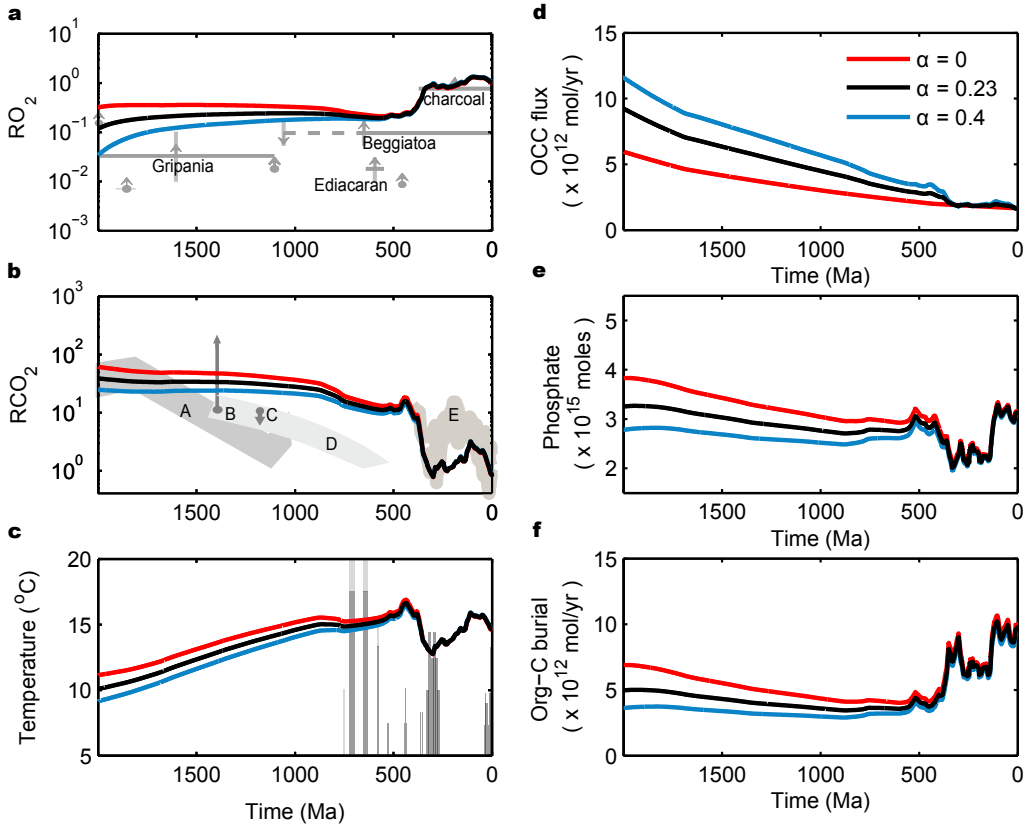

Figure 5.5.7: Mantle Model baseline for different values of α Coloured lines show different choices of the weathering parameter α. **a**, relative atmospheric oxygen concentration. Paleosol data (Rye and Holland, 1998) are shown as grey circles with arrows to distinguish between a minimum or maximum estimate. Grey horizontal lines show assumed faunal requirements (Runnegar, 1991; Canfield and Teske, 1996), with the species name in black, 'charcoal' refers to the lower limit for oxygen required by the existence of fossil charcoal. Proxy figure from Goldblatt et al. (2006). **b**, relative ocean/atmosphere CO_2 concentration. Grey shaded areas represent estimates for CO_2 concentration from paleosol data (A) (Sheldon, 2006), carbon isotope modelling (D) (Kah and Bartley, 2004) and the Phanerozoic compilation of proxies (Royer et al., 2004). Grey circles with arrows show upper and lower bound estimates from composition of fossil acritarchs (B) (Kaufman and Xiao, 2003) and cyanobacteria (C) (Kah and Riding, 2007). **c**, average global surface temperature plotted against the glacial record from this work (where the positive y axis indicates more severe glaciation). **d**, ocean crust carbonatization flux. **e**, ocean phosphate reservoir. **f** rate of burial of organic carbon. Original in colour.

5.6 Inclusion of additional weathering forcings

The Mantle Model baseline is still very simple, but provides reasonable predictions for long term climate over the Proterozoic given the uncertainty in the key parameter, α. However there are disagreements between model temperature and proxies for both the early and late Proterozoic, these may be addressed with Precambrian weathering forcings PW1 and PW2.

The forcing PW1 represents enhancement of terrestrial weathering between 750-600Ma due to continental configuration and dispersion (Li et al., 2008; Donnadieu et al., 2004), as has been added to previous models in this thesis (Mills et al., 2011). PW2 represents an assumed two-fold rise in continental weathering efficiency over the Neoproterozoic as the land is colonised by a photosynthetic biosphere. The assumed weathering rate enhancement here is based somewhat on the laboratory results of Lenton et al. (Lenton et al., 2012) and chosen as a benchmark for model testing. Details of the exact timing and nature of land colonisation as well as the effect on weathering rates and the carbon cycle are hotly debated (Kennedy et al., 2006; Knauth and Kennedy, 2009; Lenton and Watson, 2004; Lenton et al., 2012; Prave, 2002). Both weathering forcings are shown in figure 5.3.5. Model predictions when both new forcings are present are shown in figure 5.6.8. The blue line now shows $\alpha = 0.3$ rather than $\alpha = 0.4$ to avoid model break-down under low O_2.

The effect of the continental position weathering enhancement PW1 on the Mantle Model, as in the previous models where it is applied, is to reduce CO_2 and temperature over the time it is applied. Enhanced weathering between 750 and 600Ma increases CO_2 drawdown via silicate weathering until a lower temperature is reached under which the carbon cycle is balanced. Unlike the previous models, a weathering enhancement of this magnitude does not cause sufficiently low temperature (Hoffman and Schrag, 2002) to directly imply low-latitude glaciation (Donnadieu et al., 2004). This is due to the addition of the PW2 forcing, which invokes the assumption that terrestrial weathering at 750-650Ma was weaker than the early Phanerozoic.

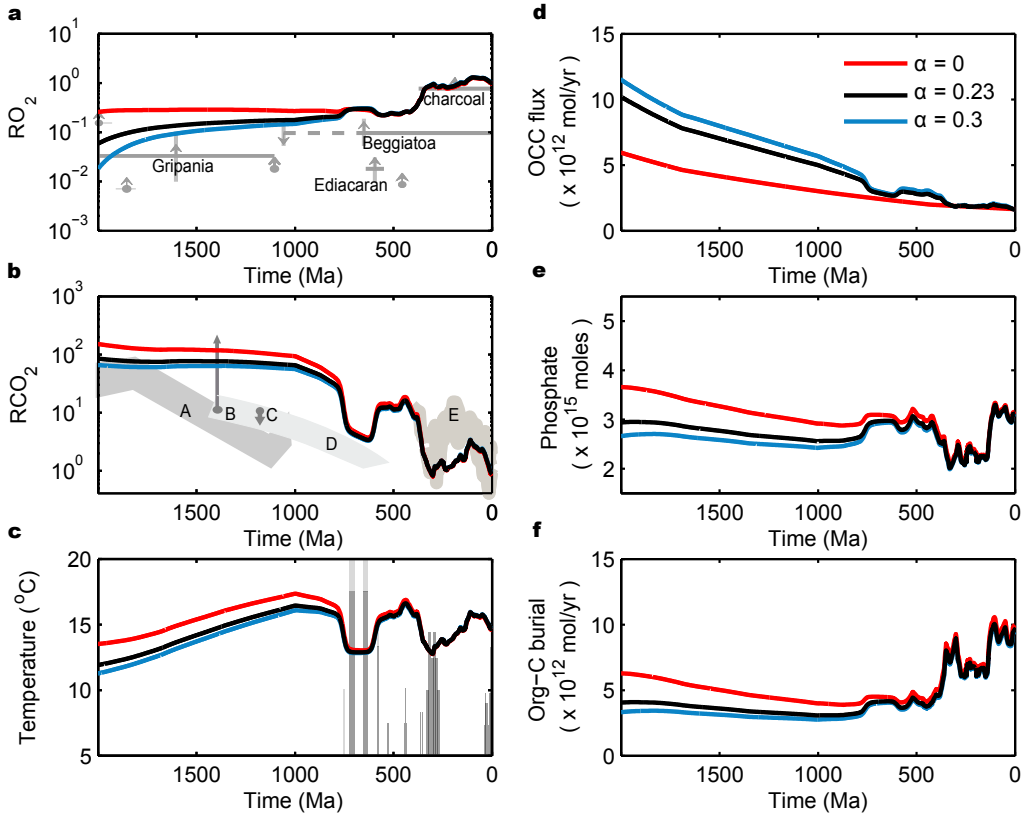

Figure 5.6.8: Mantle Model with additional weathering parameters PW1 and PW2. Coloured lines show different choices of α. **a**, relative atmospheric oxygen concentration. Paleosol data (Rye and Holland, 1998) are shown as grey circles with arrows to distinguish between a minimum or maximum estimate. Grey horizontal lines show assumed fanual requirements (Runnegar, 1991; Canfield and Teske, 1996), with the species name in black, 'charcoal' shows the lower limit for oxygen required by the existence of fossil charcoal. Proxy figure from Goldblatt et al. (2006). **b**, relative ocean/atmosphere CO_2. Grey shaded areas represent estimates for CO_2 concentration from paleosols (A) (Sheldon, 2006), carbon isotope modelling (D) (Kah and Bartley, 2004) and the Phanerozoic compilation of proxies (Royer et al., 2004). Grey circles with arrows show upper and lower bound estimates from composition of fossil acritarchs (B) (Kaufman and Xiao, 2003) and cyanobacteria (C) (Kah and Riding, 2007). **c**, average global surface temperature plotted against the glacial record from this work (where the positive y axis indicates more severe glaciation). **d**, ocean crust carbonatization flux. **e**, ocean phosphate reservoir. **f** rate of burial of organic carbon. Original in colour.

The formulation of the model allows for an increase in nutrient concentration over the PW1 period. This is because the assumed climate dependence for carbonate and silicate weathering is different (Berner, 1994), meaning that the ratio of the two types of continental weathering is different under different temperatures, altering nutrient delivery (Bergman et al., 2004; Van-Cappellen and Ingall, 1996). If instead it is assumed that nutrient delivery scales with the bulk terrestrial weathering flux, nutrient concentration (and therefore oxygen) would rise when the forcing was applied, but fall back to the initial state once the climate had stabilized. When the forcing is removed at 600Ma the system recovers to match the unforced system shown in the previous figure.

The land colonisation forcing PW2 describes a gradual enhancement of terrestrial weathering from 1000-500Ma as the land surface becomes dominated by photosynthetic organisms. The effect in the model is to increase predicted CO_2 concentration and temperature for all time before the colonisation event is complete, as is seen in the Phanerozoic models for the evolution of vascular plants (Berner, 1991). Assuming a forcing such as this increases predicted Paleoproterozoic temperature to better fit the glacial record. However, Mesoproterozoic CO_2 is now considerably higher than proxy data would suggest. Assuming an earlier establishment of land-based ecosystems (e.g. 1.1Ga (Sheldon and Hren, 2012)) would shift the associated temperature drop further back in time. For $\alpha > 0$ the model now predicts a gradual rise in nutrient and oxygen concentration over the land colonisation period (1000-500Ma) in addition to the peak between 750-600Ma. This is because further reduction in the efficiency of continental weathering (before PW2 is applied) pushes the weathering balance more in favour of ocean crust carbonatization, resulting in less nutrient delivery. For all choices of α, the Proterozoic oxygen window is predicted as $O_2 < 0.3$PAL.

Climate forcings due to continental position, dispersion and the supercontinent cycle (Hawkesworth et al., 2010) have existed throughout Earth history, but are difficult to quantify. The current representation simply expresses an expected peak in this forcing in the Neoproterozoic, but it is likely that climate, specifically atmospheric CO_2 and temperature, has been tightly coupled to tectonic events over the last 3Gyr. Atmospheric methane concentration has also likely contributed to global temperature (Pavlov et al., 2003)

and affected oxygen concentration (via methane oxidation and hydrogen escape to space (Watson et al., 1978; Catling et al., 2001; Claire et al., 2006)) over Earth history.

5.7 Summary of the effects of weathering pathways on CO_2 and O_2 predictions

Despite uncertainties in the tectonic and biological forcings, and the omission of methane from this model, some conclusions can be drawn regarding Proterozoic climate:

Addition of the ocean crust carbonatization (OCC) flux to the model results in a new pathway for CO_2 removal that is unlike the silicate weathering-carbonate deposition process - OCC does not deliver phosphorus to the oceans (Wheat et al., 2003; Paytan and McLaughlin, 2007). The effect of the addition of the OCC flux is to decouple the CO_2 removal rate from the nutrient delivery rate, so that assuming a strong OCC flux leads to significantly lower predictions for ocean nutrient and oxygen concentration. The previous Minimal Model predicted roughly present day levels of oxygen in the Paleoproterozoic because the only CO_2 sink was terrestrial weathering. The higher degassing rate requires that more carbon be buried globally, and to do this by increasing only terrestrial weathering rates resulted in nutrient delivery rates higher than the present day. The dependence of OCC on the global spreading rate acts to counteract the higher degassing rate in the Mantle Model.

The assumed dependence of ocean crust carbonatization on CO_2 concentration (α) is a very important model parameter, effectively controlling the relative strength in the model of the OCC flux. The stronger the OCC flux, the more carbon is buried this way, shifting the balance of carbon removal to include less terrestrial weathering. Therefore a stronger OCC flux results in lower ocean nutrient, productivity and oxygen. CO_2 concentration is also reduced because the enhanced OCC flux requires less CO_2 in the oceans to balance the carbon cycle (Sleep and Zahnle, 2001).

Additional reductions in the efficiency of continental weathering due to the absence of even simple land biota before the Mesoproterozoic leads to very low oxygen predictions for this time, as the removal of CO_2 is domi-

nated by the OCC flux. Assuming a dependence of the OCC flux on CO_2 concentration (Brady and Gislason, 1997), a gradual increase in the oxygen content of the atmosphere is predicted over the Proterozoic. Looking further back to the Archean, the increase in mantle heat flux and further decrease in continental area would lead to even lower oxygen predictions in this model, suggesting that the 2.4Ga great oxidation event (Sessions et al., 2009) may have been caused by increasing ocean primary productivity due to the emerging terrestrial weathering sink (Hawkesworth et al., 2010) for carbon and the associated increase in nutrient supply. A gradual increase in primary productivity (Goldblatt et al., 2006) has been shown as sufficient to cause the observed step change in oxygen concentration, which is expected to occur due to positive feedback between O_2 and CH_4 concentration during the formation of an ozone layer (Claire et al., 2006).

5.8 Long term carbon and sulphur cycling between the crust and mantle

The weathering forcings PW1 and PW2 are included in the model for the remaining figures in this chapter. As seen in Hayes and Waldbauer (2006), on which this model is based, carbon steadily accumilates in the crust over time due to the imbalance between carbon input from the mantle and carbon subduction. The total size of the crustal carbon reservoir in the Mantle Model is shown in figure 5.8.9b, closely following the results of Hayes and Waldbauer (which are shown in figure 5.2.2).

The simple sulphur cycle used in the model closely links ocean sulphate levels to oxygen concentration by assuming that sulphate input to the ocean through oxidative weathering of rocks containing reduced S is controlled by atmospheric O_2 (Bergman et al., 2004). Removal of ocean sulphate via anaerobic microbial reduction and eventual burial as pyrite is also assumed to depend on oxygen concentration, in this case via an inverse relation to the sulphate sink rather than a direct relationship to the sulphate source, thus strengthening the link. The result in the model is a prediction for relative ocean sulphate that very closely follows the predictions for relative O_2. The relative abundance of crustal oxidised sulphur (modelled as gypsum) also follows closely the predictions for relative oxygen concentration, as burial of

gypsum is a strong function of sulphate concentration.

Predicted sulphate concentration is shown alongside previous results from sulphur isotope modelling (Kah et al., 2004) (A) and Phanerozoic proxy data (Horita et al., 2002; Hardie, 1996) (B,C). The best match to the Precambrian sulphur isotope model (A) is achieved for high values of α, i.e. a strong ocean crust carbonatization flux.

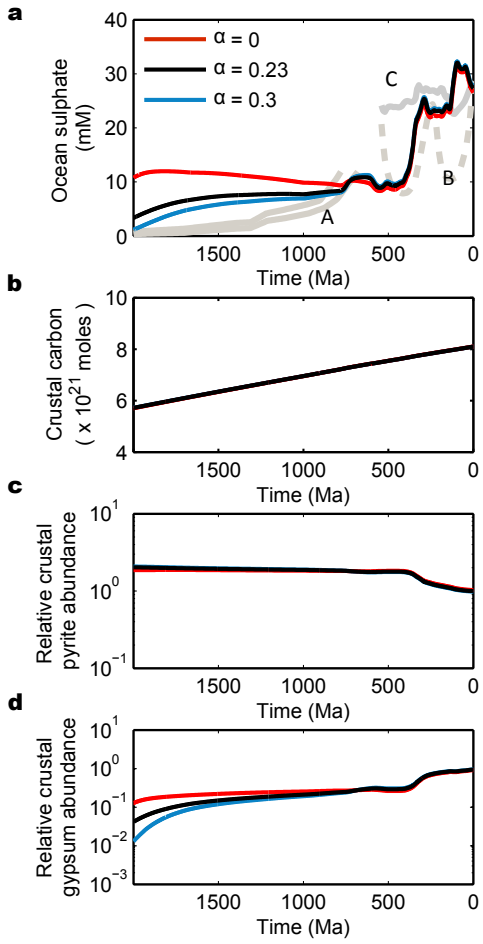

Figure 5.8.9: Sulphur reservoirs and crustal carbon accumulation in the Mantle Model. For all panels, coloured lines represent different choices of α. **a**, ocean sulphate concentration. Grey lines show predictions for Precambrian sulphate concentration from a model for sulpuhr isotope change (denoted A) (Kah et al., 2004), Phanerozoic sulphate estimated via analysis of fluid inclusions in marine halite (B) (Horita et al., 2002) and by the assumed mixing between river water and hydrothermal brines (C) (Hardie, 1996; Spencer and Hardie, 1990). **b**, total crustal carbon. **c**, relative crustal pyrite content. **d**, relative crustal gypsum content.

Further sulphur isotope modelling by Canfield and Farquhar (2008) gives a 'best guess' ocean sulphate concentration of $\sim$ 1mM for the Proterozoic (Canfield and Farquhar, 2008), similar to the model results for 2Ga but considerably lower thereafter. Agreement with Phanerozoic proxies is reasonable, although there is a large discrepancy between the model and proxies in the Mesozoic, as with the previous COPSE model (Bergman et al., 2004).

The model predicts that crustal abundance of reduced sulphur (modelled as pyrite) would be stable at around double the present day value for the Proterozoic, due to enhanced burial and reduced oxidative weathering. There is little available data to suggest how crustal sulphur abundances have changed during the last 2Ga, however the predicted trend of an increasing oxidised sulphur reservoir, and decreasing reduced sulphur reservoir seems reasonable given the proposed oxygenation scenario. The model of Canfield (2004) for the mantle sulphur cycle predicts a surface sulphur reservoir between 0.5-2 times the present day size at 2Ga, similar to the model here which predicts a surface sulphur reservoir 1-2 times the present day size at 2Ga.

5.9 Predicted stable isotope fractionation

5.9.1 Carbon isotopes

The top row of figure 5.9.10 shows model predictions for the ratio of organic carbon burial to total carbon burial (termed the 'f' ratio) for different choices of α. As expected, higher values of α cause the f-ratio to become lower further back in time: reduced ocean nutrient and therefore productivity results in a smaller fraction of total carbon burial occurring organically. The lower panels show the corresponding $\delta^{13}C$ of new carbonate, plotted against data from Veizer et al. (1999) and Shields and Veizer (2002). In figure 5.9.10, four model runs are shown for each choice of α, allowing for a range of assumed fractionation effects to be considered, these are listed in the following table.

Run	Fluxes with fractionation effects	$\delta^{13}C\,(\mathbf{C})$ at model start
1	ocb	-2 ‰
2	ocb, ccb	-2 ‰
3	ocb, ccb, occ	-2 ‰
4	ocb, ccb, occ	0 ‰

Table 15: Assumed fractionating processes for carbon in the Mantle Model. ocb = organic carbon burial, ccb = marine carbonate carbon burial, occ = ocean crust carbonatization.

In run 1 the fractionation of carbon is assumed to occur only via organic carbon burial, which is assumed to impart a fractionation of -27‰ relative to the atmosphere/ocean reservoir. Added to this in run 2 is the temperature and CO_2 dependent fractionation on carbonate burial assessed in COPSE (Bergman et al., 2004) and in Mills et al. (2011). In run 3, a fractionation effect is also added to the ocean crust carbonatization flux, following Bjerrum and Canfield (2004) and taking a maximum estimate, we allow carbon buried via OCC to be 7‰ lighter than the ocean/atmosphere. The crustal carbonate carbon reservoir, $\mathbf{C}$, holds around 80% of global carbon and therefore the assumed isotopic composition of $\mathbf{C}$ at model start will buffer atmospheric $\delta^{13}C$ considerably.

In runs 1-3, the model is initiated with $\delta^{13}C\,(\mathbf{C}) = -2$, which is the steady state value for run 1 and $\alpha = 0$. However, data show a large positive $\delta^{13}C$ excursion in the period 2.3-2Ga (Bekker et al., 2006), directly preceeding model startup. It is therefore likely that the crustal carbonate reservoir may have been buffered by this burial of isotopically heavy carbon. To test this we allow $\delta^{13}C\,(\mathbf{C}) = 0$ at model startup in run 4, which also includes the isotopic modifiers from run 3. The runs produce a range of possible $\delta^{13}C$ predictions from the same biogeochemical system, illustrating the difficulties (Bjerrum and Canfield, 2004) in determining system characteristics, such as organic carbon burial (Berner, 2001), from isotopic proxies alone.

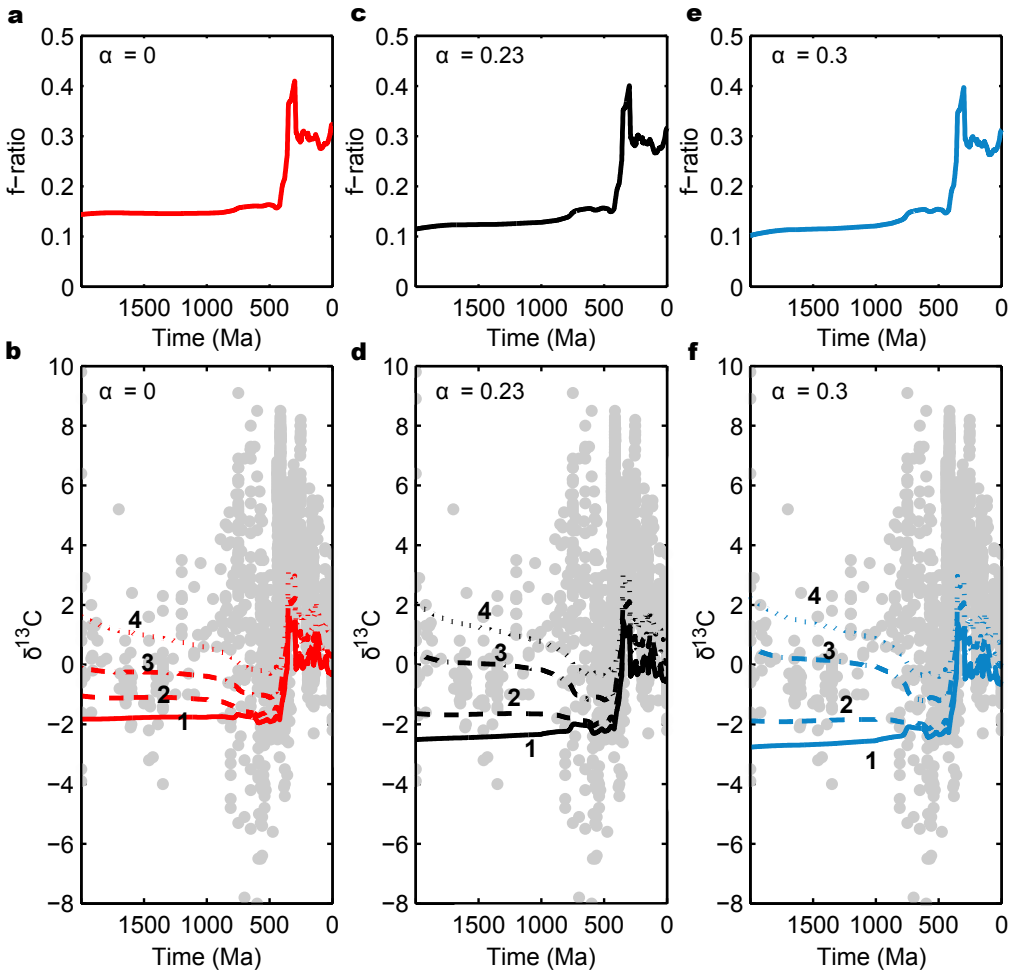

Figure 5.9.10: Mantle Model predictions for carbon isotope fractionation. As before red lines indicate the $\alpha = 0$ model run (**a,b**), black for the $\alpha = 0.23$ run (**c,d**) and blue for $\alpha = 0.3$ (**e,f**). Organic fraction of carbon burial (termed the 'f' ratio) is shown in the upper panels. The lower panels show the resulting range of $\delta^{13}C$ predictions, dependent on various fractionation parameters: solid line shows results with a constant fractionation effect for organic carbon burial and no other fractionation, the dashed line adds to this a fractionation effect for marine carbonate burial (Bergman et al., 2004), dash-dot line adds a further fractionation effect to the OCC flux (Bjerrum and Canfield, 2004) and dotted line adds also a fractionation effect due to previous isotope reservoir dilution. See text for full description of fractionation effects. Grey dots show the data of Veizer et al. (1999) and of Shields and Veizer (2002).

For run 1, δ^{13}C predictions are negative for the period 2-0.5Ga for all values of α, largely inconsistent with the data. This highlights the apparent paradox that significantly lower biological productivity on the Early earth

is not permitted by the apparent stability of the δ^{13}C record (Schidlowski, 1988; Catling et al., 2001; Kump et al., 2001). When the additional fractionation processes are considered, each has the effect to increase model δ^{13}C predictions. In run 2 the increase is caused by increased fractionation of buried carbonates under high CO_2, as in Mills et al. (2011).

If ocean crust carbonatization is assumed to impart a fractionation effect (Beukes et al., 1990; Kaufman et al., 1990) (run 3 and 4), choosing a high value of alpha leads to $\delta^{13}C \geq 0$ throughout the Proterozoic. The $\delta^{13}C$ 'envelope' produced for each choice of α is broadly consistent with the proxy records, showing that the impact of various fractionating processes is a key uncertainty, and indeed may allow for very low organic carbon burial rates in the Proterozoic, as discussed by Bjerrum and Canfield (2004). Whilst the uncertainty in these mechanisms means that accurately modelling δ^{13}C variation is difficult, the figure shows that the current model is not necessarily falsified by the predictions for isotopic fractionation.

This model does not reproduce high positive carbon isotope fractionation in the Neoproterozoic era, as there is no inclusion of snowball Earth events, which would likely cause long-term positive isotopic excursions in their aftermath (Mills et al., 2011). The inclusion of oxygen in this model means that a snowball Earth environment cannot be maintained, O_2 concentration quickly falls below the model lower limit on the glaciated Earth. Maintaining a model biosphere during a 'hard' snowball glaciation is a future challenge both for biogeochemical models and for the snowball Earth hypothesis.

5.9.2 Sulphur isotopes

Figure 5.9.11 shows model predictions for seawater sulphate δ^{34}S, alongside the fraction of sulphur that is buried as pyrite, denoted the 'fs - ratio'. Burial of pyrite is assumed to decrease with decreasing nutrient availability, but is also assumed to increase in low oxygen conditions, therefore choice of α has only a small impact on the sulphur burial ratio for most of the model timeframe.

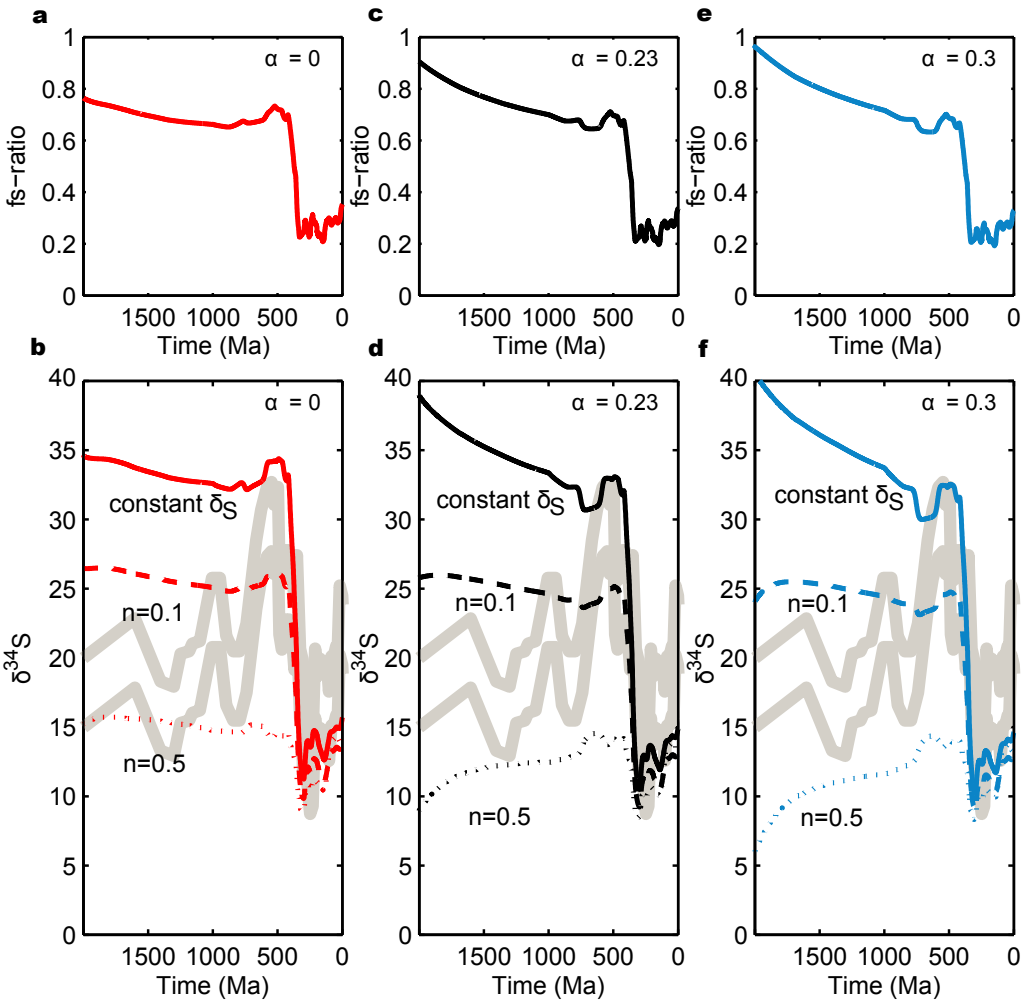

Figure 5.9.11: Mantle Model predictions for sulphur isotope fractionation. Red lines indicate the $\alpha = 0$ model run (**a,b**), black lines show the $\alpha = 0.23$ run (**c,d**) and blue lines show $\alpha = 0.3$ (**e,f**). Fraction of sulphur that is buried as pyrite (here called the 'fs' ratio) is shown in the upper panels. Lower panels show the resulting range of δ^{34}S predictions under either a constant fractionation effect for sulphide burial, or under an oxygen-dependent fractionation with parameter n (see text). Grey lines show proxy constraints reproduced from Canfield (1998); Canfield and Teske (1996), with the two lines representing a 5‰ uncertainty.

Canfield (2004) calculates the expected fractional pyrite burial from the isotopic records of both seawater sulphate and sedimentary pyrite, concluding that the fraction of sulphur buried as pyrite must have been between 0.5 and 1 during the Proterozoic. This rough estimate is reproduced by the model. The lower panels in figure 5.9.11 show the corresponding predictions

for $\delta^{34}S$ with respect to the assumed fractionation parameter, n, against results when the fraction effect is held constant (here $\delta_S = 40‰$). Here, as in the GEOCARB models, n represents the effect of changing oxygen concentration on the observed fractionation between seawater sulphate and buried pyrites: $\delta_S = 35\,(RO_2)^n$ (Berner, 2001, 2006a). This is based on observed high fractionation with increased oxygen, which has been related to further fractionation of reduced material during the oxidative sulphur cycle (Canfield and Teske, 1996; Jorgensen, 1990; Canfield and Thamdrup, 1994).

Sulphur isotope fractionation is very sensitive to the n parameter, leading to extremely low $\delta^{34}S$ predictions for high values of n. A vague fit to the proxy data can be achieved by assuming n=0.1, but this is very far from the n=1.5 used in the work of Berner (2001), which produces incompatible results in this model due to the predicted low oxygen concentration for the Proterozoic. Admittedly the sulphur system used in this model clearly requires improvement to correctly represent Proterozoic climate, but the massive uncertainty is sulphur fractionation effects over time makes falsification via predicted $\delta^{34}S$ difficult.

5.10 Chapter summary and conclusions

5.10.1 Summary of important findings

1. Extrapolating the simple carbon, sulphur and nutrient 'Minimal Model' used in the previous chapters further back through the Proterozoic gives predictions for high O_2 throughout the eon, increasing more the further we go back, violating multiple proxy evidence for low O_2. This is because the assumed higher degassing rates require that burial must rise to stabilise the system, resulting in increased organic burial and oxygen production.

2. Addition of the Ocean crust carbonatization (OCC) carbon removal pathway in the Mantle Model provides a sink for CO_2 that does not transfer nutrients to the surface ocean, therefore allowing total carbon burial to be high enough to stabilise the system with a much lower organic carbon burial rate and therefore lower O_2 production flux. The result is a predicted Proterozoic oxygen concentration window of 10^{-3}-

3×10^{-1}PAL, consistent with the majority of proxies.

3. Specific predictions for O_2 and CO_2 depend greatly on the assumed relationship between OCC and oceanic CO_2 concentration (α), which is poorly constrained. The predicted O_2 trend for all values is between stability and a gradually increasing concentration over the Proterozoic. Allowing some dependence of OCC rate on CO_2 concentration, as well as additional terrestrial weathering forcings, results in a clear O_2 rise over the Eon. CO_2 predictions for the Mesozoic are consistently higher than some proxies suggest, however the low concentration inferred from these proxies would imply glaciation (Kasting, 1987), for which there is no evidence.

4. The model predictions for ocean sulphate, crustal sulphur species and the fractionation of carbon and sulphur stable isotopes are reasonable when compared to the limited proxy information available and therefore do not falsify the model. However, explicit representation of anoxygenic photosynthesis and microbial sulphate reduction is required for a more complete view of the Proterozoic sulphur cycle.

5.10.2 Conclusions

The key finding of this chapter is that the change in dominant carbon removal pathways over Earth history, which has been well described and modelled (Sleep and Zahnle, 2001; Hayes and Waldbauer, 2006), would be expected to restrict nutrient delivery by terrestrial weathering over the Proterozoic. Despite higher carbon degassing rates, model predictions for total organic carbon burial are $25 - 75\%$ of the present day rate. The fraction of carbon buried organically (the f-ratio) is 0.1-0.15, resulting in predictions for atmospheric O_2 concentration that agree well with current proxy estimates.

Low carbon burial rates in earlier Earth history have previously been inferred directly from the isotope record. Bjerrum and Canfield (2004) assumed that a fraction, λ, of carbon removal from the surface system occurs in the deep ocean. Taking into account the isotope fractionation effect likely to be imparted by this burial pathway (Beukes et al., 1990), the f-ratio is calculated

from the geological record of carbon $\delta^{13}C$ and is found to have increased significantly over time. The work here compliments this approach by showing that a simple process-based biogeochemical model predicts a low and very similar average f-ratio over the Proterozoic. The isotope fractionation effect associated with ocean crust carbonatization here allows for the model to output to agree well with the geological $\delta^{13}C$ record, however agreement is still fair in its absence providing other fractionation effects are considered.

6 Thesis conclusions

In this chapter I first list the key findings of the thesis, then briefly investigate some ideas linking the two main themes of weathering pathways and material limits. Limitations of the current modelling approach are then discussed, followed by details of model improvements and extensions, and some discussion of the wider context of the work.

6.1 Main findings

• The current generation of Phanerozoic biogeochemical box models: GEOCARB (Berner, 2006a), COPSE (Bergman et al., 2004) and MAGic (Arvidson et al., 2006) are reduced to a single robust, modular system that allows application to Neoproterozoic climate (the 'Minimal Model'). The methods for calculating atmospheric oxygen concentration in the Phanerozoic are found to give unreasonable results when applied to the Precambrian.

• The time taken for global temperature to stabilize after a snowball glaciation should be on the order of 10^7 years, roughly matching the interval between deep glaciations in the Neoproterozoic. Therefore it is proposed that the geological record for the late Neoproterozoic shows a system that is oscillating around a global steady state temperature which is below the threshold for low-latitude glaciation.

• Snowball Earth events, as traditionally described (Hoffman et al., 1998), should be followed by prolonged ($> 10^7$ yr) periods of carbon cycle disequilibrium, in which enhanced nutrient delivery and carbon burial would be expected to maintain elevated oxygen concentrations. This may have important applications to the apparent oxygen rises at 2.4Ga and 0.58Ga, both of which are loosely associated with low-latitude glaciation, however the mechanisms here suggests a lengthy perturbation rather than a stepwise system change.

• Carbon removal via the seafloor weathering pathway, and its link to the mantle heat flux, provides a mechanism for increasing oxygen concentration over Earth history: The fraction of global carbon burial that occurs on the seafloor is expected to have decreased over time (Bjerrum and Canfield, 2004; Sleep and Zahnle, 2001), and it is shown that this would be expected to cause a compensatory rise in terrestrial weathering, hence nutrient delivery and productivity. Coupled model predictions for Proterozoic O_2, CO_2, temperature and sulphate levels fall within or close to the limits imposed by various geological proxies.

6.2 Linking weathering pathways and transport limitation

Long term global weathering fluxes have been the key focus of this thesis. It has been shown that both changes in dominant weathering pathways, and consideration of material-transport limitations on terrestrial weathering may be able to explain important features of the geological record. In this section, some synthesis of these two key findings is attempted.

6.2.1 Effect of OCC pathway on post-snowball CO_2 removal

The model used to demonstrate the effect of transport limitation of terrestrial weathering on snowball Earth recovery times (Chapter 4) did not include the ocean crust carbonatization (OCC) flux, and it has been suggested (West, 2011) that this additional sink for CO_2 may make significant differences to the stabilization times shown in figure 4.2.2. The important question here is that of the maximum possible global OCC rate, hereafter W_{max}(OCC), which alongside the calculated maximum terrestrial rate W_{max}(terrestrial), may constrain the total abundance of material for weathering. This is extremely difficult to quantify, as it is currently uncertain whether present day OCC rates are limited by material transport or reaction kinetics (Sleep and Zahnle, 2001). A representation of the OCC flux is added to the model used in Chapter 4, and follows the form used for this flux in the Mantle Model:

$$F_{occ} = k_{occ} \cdot Q^2 \cdot \left(\frac{RCO_2}{RCO_2(0)} \right)^{\alpha} \quad (6.2.1)$$

where $k_{occ} = 1.65 \times 10^{12}$ mol/yr is the present day rate (Sleep and Zahnle, 2001; Elderfield and Schultz, 1996). As with the model solar flux, the heat flux, Q, is held at the value for 650Ma. The rate of present day silicate weathering in the model is reduced to maintain present day carbon cycle balance under the assumed OCC flux.

Figure 6.2.1 shows the time taken for the model system to stabilize following a 0.3atm CO_2 perturbation against the terrestrial weathering rate limit W_{max}(terrestrial). The two panels show different choices of α, red lines show solution under different maximum OCC rates, the black line in each panel shows the original model results from Chapter 4, where OCC was not considered. For the $\alpha = 0.23$ case (panel **a**), little variation is shown under the addition of the OCC flux, despite consideration of a large upper limit. In this panel, the results for W_{max}(OCC)=5 and W_{max}(OCC)=10 plot over each other, indicating that the OCC rate in the model does not reach 5 times the present day rate, even under 0.3atm CO_2. Panel **b** allows a more powerful dependence of the OCC rate on atmosphere/ocean CO_2 concentration, $\alpha = 0.5$. Here it can be seen that the OCC flux reaches a maximum rate of 5-10 times the present day, and assuming this rate can be maintained for millions of years (i.e. W_{max}(OCC)>5), acts to reduce the stabilization times as suggested. However, even at this rate, stability times for $D = 1$ are $\geq 7 \times 10^6$ years, and are increased under a higher estimate of the degassing flux, as would be expected in the Neoproterozoic.

Because the OCC flux buries several times less carbon than terrestrial weathering, a powerful dependency on CO_2 concentration is required for this pathway to significantly alter the timeframe for CO_2 drawdown following a snowball Earth glaciation. In addition to this, it must be assumed that material limitation of this process allows for a ≥ 5 fold increase in this flux to be maintained over a $> 10^6$ year timescale. Both of these requirements are currently very uncertain, and available laboratory data constraining the CO_2-OCC relationship (Brady and Gislason, 1997)(panel **a**) suggests that it is insufficiently strong to significantly change the results of the original study, even when no upper limit is assumed. The conclusions from the original work

therefore remain unaltered, as timescales for system recovery above 10^7 years are still observed under a wide range of assumptions for the degassing rate and W_{max}(terrestrial), even with the addition of an extremely strong OCC flux.

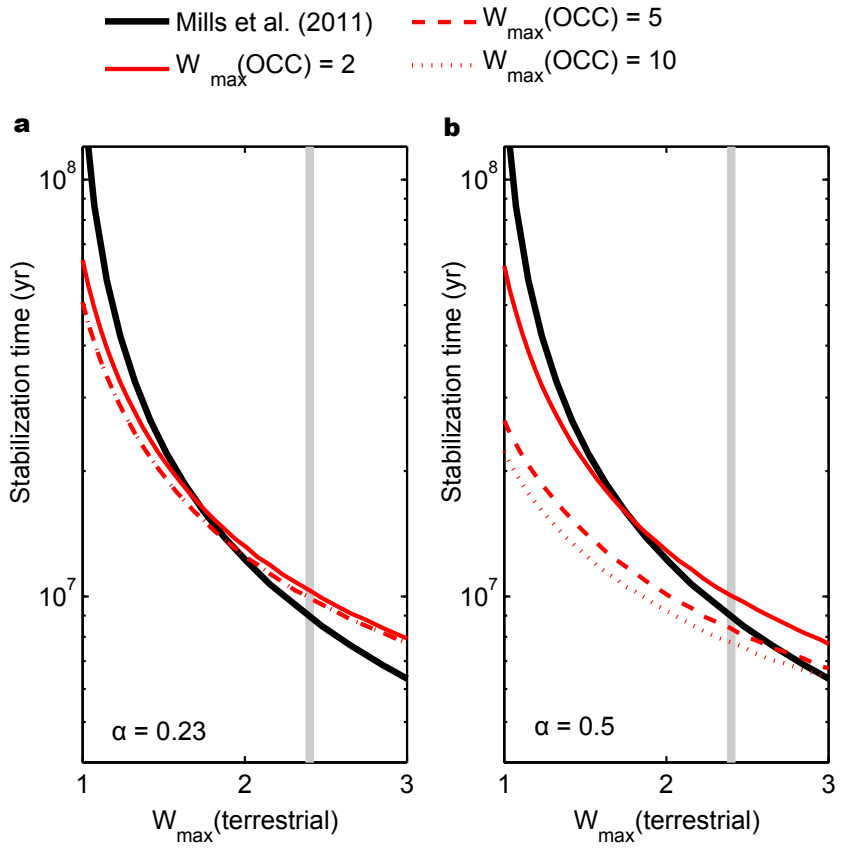

Figure 6.2.1: Post-snowball stabilization time versus maximum terrestrial weathering rate, W_{max}(terrestrial). An initial CO_2 concentration of 0.3 atmospheres is assumed, and the global terrestrial weathering rate is fixed at W_{max}(terrestrial). The three red lines show different choices of the OCC rate limit W_{max}(OCC). W_{max}(terrestrial) and W_{max}(OCC) are defined relative to present day rates, with the grey vertical line showing the estimate of W_{max}(terrestrial) = 2.4 for the Phanerozoic. For all runs, the degassing rate is assumed to be equal to the present day. Black line shows results of Mills et al. (2011) for D=1.

6.2.2 Transport limitation of weathering over Earth history

In the Mantle Model presented in Chapter 5, there is no consideration of a global weathering rate limitation. However, due to higher degassing rates earlier in Earth history, it is perhaps possible that the terrestrial weathering sink for CO_2 may have been insufficient to balance the system. The model is amended here to allow transport-limitation of terrestrial weathering by using the silicate and carbonate weathering fluxes derived for the work in chapter 4. Following the method used here for the Phanerozoic, the maximum rate-limited flux is assumed to depend on the global erosion rate forcing. It is assumed that the OCC rate does not reach a material limitation here. Figure 6.2.2 shows an example model run where $\alpha = 0$ and the maximum terrestrial weathering rate is set to $W_{max}(\text{terrestrial}) = 1.5$ under present day erosion rates.

Under these conditions, the model predicts a CO_2 spike similar to that which may have been possible during the Phanerozoic (see section 4.5.3). This occurs during the period 1300-800Ma, where global erosion rates are expected to be low (panel **c**). Interestingly, earlier periods for which $\frac{\text{degassing}}{\text{erosion}}$ is higher, are not characterised by transport limitation of global weathering. The higher heat flux at this time increases the CO_2 sink via ocean crust weathering, requiring lower rates of terrestrial weathering to balance the system, and therefore allowing carbon cycle balance despite severe limitation of the terrestrial flux. Assuming $\alpha > 0$ allows for the OCC rate to increase in response to elevated CO_2 concentration and therefore system stability is retained even for very low values of $W_{max}(\text{terrestrial})$, such as the scenario in figure 6.2.2.

The apparent paradox of a stable carbon cycle on the early Earth under very high CO_2 degassing rates can therefore be addressed: The high mantle heat flux on the early Earth, which is the cause of the rapid degassing, also increases the magnitude of the ocean crust carbonatization CO_2 sink, and therefore a high terrestrial weathering rate is not required for stability.

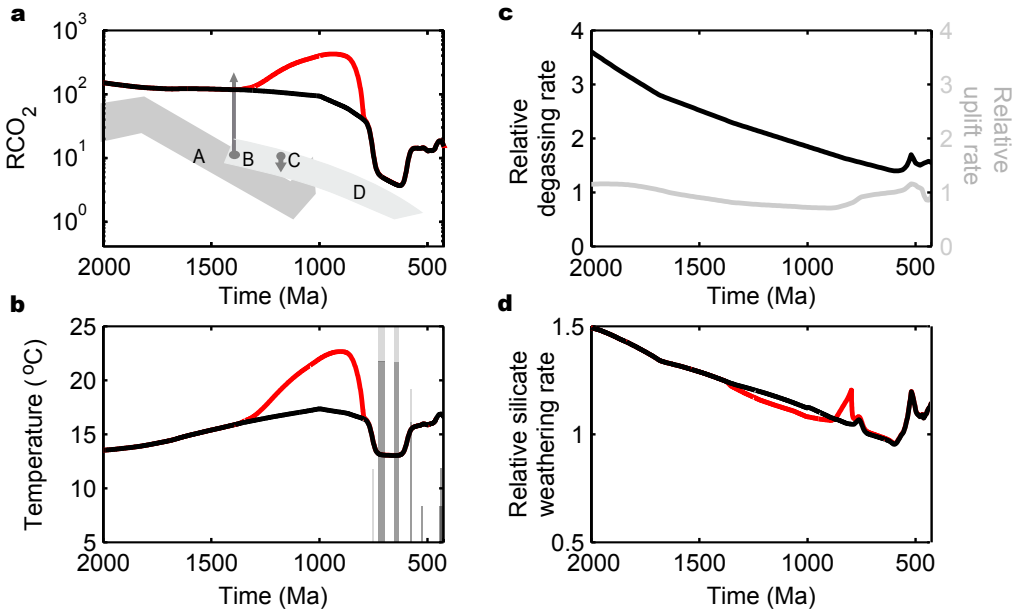

Figure 6.2.2: Terrestrial weathering limitation in the Mantle Model. Red lines show results for W_{max}(terrestrial)=1.5 and assumes no maximum rate for OCC, black lines show system without consideration of a terrestrial weathering limit for comparison. For both runs $\alpha = 0$. **a**, relative CO_2 concentration against proxy data from previous chapter (paleosols (A) (Sheldon, 2006), carbon isotope modelling (D) (Kah and Bartley, 2004), estimates from composition of fossil acritarchs (B) (Kaufman and Xiao, 2003) and cyanobacteria (C) (Kah and Riding, 2007)). **b**, average global surface temperature, **c**, model forcings for uplift and degassing rates, **d**, global rate of silicate weathering.

6.3 Model limitations

The models explored and constructed in this thesis are semi-quantitative. They are best utilised for the demonstration of specific Earth system mechanisms, and for attaining broad, but falsifiable predictions based on operation of these mechanisms. A persistent problem with these models is the simple formulation of the flux functions - global biogeochemical processes are often limited by a multitude of factors but are traditionally modelled using very few, and often under a single linear or power-law relationship. This can lead to overly-strong negative feedback, and to very powerful but poorly-constrained parameters (e.g. α in this work). As shown in Chapter 4, consideration of multiple limiting factors for the terrestrial weathering flux can lead to dramatically different model predictions in some scenarios.

The predictions for Proterozoic climate presented in Chapter 5 (the Mantle Model) should be taken as a broad envelope, as is displayed on the figures therein, but even so, this envelope only represents the uncertainty in a single key parameter. The simplified ocean nutrient model used has been criticised for its combined global approximation of shelf and open-water burial rates, and the lack of burial limitation by erosion (Berner, 2006a), but criticisms of this nature may just as easily be levelled at any of the fluxes in any of these models. I believe that the Mantle Model is very useful, as it demonstrates an intriguing mechanism for planetary oxidation and makes numerous falsifiable predictions. To my knowledge there are currently no published works that attempt to reconstruct Proterozoic oxygen concentration using an a priori model. Falsification of the proposed oxygenation mechanism is hampered by the wide range of model uncertainty, but also by availability of geochemical evidence. Fuller understanding of the Earth system and of paleoclimate requires advances in modelling techniques, but also requires additional geological fieldwork and laboratory studies to constrain both the strength of biogeochemical feedbacks and the knowledge of paleoclimatic conditions.

6.4 Future modelling work

The long-term goal of the work in this thesis is to arrive at a process-based biogeochemical model for the whole of Earth history. A model such as this would be a useful tool for testing a huge list of hypotheses linking the global biota, tectonic regime and hydrospheric composition. Examples include the effects of Paleoproterozoic glaciation, possible triggers for the Great Oxidation event, and application to oxidation of hypothetical exoplanets. Constructing an Earth history model requires many improvements over the current model system, some interesting avenues for model expansion are listed below.

6.4.1 Low-oxygen solutions

Currently the Mantle Model timeframe is limited to 2Ga-present because of the low oxygen concentrations that are predicted before this time. The Phanerozoic-based functions for burial of pyrite sulphur and for ocean nutrient balance are strongly dependent on oxygen concentration, and a sim-

plistic representation of ocean anoxia. The system becomes unstable under low nutrient and low ($< 10^{-3}$PAL) oxygen concentrations, in this situation a reduction in O_2 causes an ocean sulphate crisis which limits sulphide burial and further decreases O_2, this positive feedback loop results in zero oxygen and model breakdown.

Addressing this problem requires reconstruction of the model to include a functioning anaerobic biosphere, of which currently there is only a rough parameterisation. Some preliminary work was undertaken to incorporate the simple biota and methane system from the early Earth model of Goldblatt et al. (2006) into the model framework in this thesis. Powerful negative feedbacks on respiration rates in this system allow oxygen concentration to be stable at $< 10^{-5}$PAL and for the bistability in atmospheric oxygen highlighted in the original work to be reproduced. However, the combination of model approaches did not represent a sufficiently consistent view of the biosphere to obtain useful predictions. It does however demonstrate that consideration of negative feedbacks operating around low oxygen concentrations may be a vital addition for future modelling.

6.4.2 Representation of limiting factors for key processes

As has been suggested in this work and others (West et al., 2005; Millot et al., 2002), extrapolation of simple kinetic rate equations to global scale weathering fluxes does not represent the process sufficiently well. In a broad sense, all of the fluxes in the model suffer from a similar over-simplification and are generally limited by a number of factors that do not, as models often assume, act as simple multipliers to the overall rate. For example, oxidative weathering is reasoned to have some dependence on atmospheric O_2 (Lasaga and Ohmoto, 2002) but this is not apparent in some field studies, which instead link weathering rates to erosion (Wildman et al., 2004; Bolton et al., 2006). Most likely a combination of these factors controls the overall rate. Recently, attempts have been made to construct a flux equation based on mechanistic understanding of the terrestrial weathering process (West et al., 2012; Dixon et al., 2012). Future models will aim to incorporate these approaches, and an attempt will be made to apply a similar analysis to the degassing, burial and nutrient fluxes.

6.4.3 Full representation of mantle cycling

The current Mantle Model does not track changes in the size or isotopic composition of the mantle reservoirs, composition is assumed to be constant and the size of the mantle inventories of carbon and sulphur are assumed not to have any effect on the model fluxes. A simple extension would allow the mantle inventories and composition to change over time, perhaps allowing an additional route to falsification of predictions. Another intriguing question is that of the consistent oxygen fugacity of the mantle (Li and Lee, 2004), which may perhaps be adequately approximated via knowledge of the oxidized and reduced fluxes into and out of the mantle.

6.4.4 On Phanerozoic modelling

Current Phanerozoic models assume for simplicity that the large crustal reservoirs of carbon and sulphur are at present day size at the beginning of the Phanerozoic. Extending the model timeframe to the Proterozoic allows instead for prediction of these values based on likely Precambrian climate. In the Mantle Model, predicted low Precambrian O_2 causes an increase in the crustal abundance of reduced sulphur due to enhanced pyrite burial. The Permo-carboniferous oxygen peak is therefore reduced from $\sim$ 1.4PAL in COPSE to $\sim$ 1 PAL in the Mantle Model because of the more powerful oxygen sink from pyrite weathering.

The work in the Chapter 2 highlights the importance of negative feedback in prediction of Phanerozoic oxygen concentration. One of the most powerful, and most difficult to model, is the feedback provided by wildfires. As with the weathering fluxes, the occurrence and spread of fire may be best understood using a physically based model of the competing limiting factors. Fairly complex fire modules are currently applied in dynamic global vegetation models (DGVMs) (Bachelet et al., 2001; Sitch et al., 2003; Thonicke et al., 2010) and have been applied to paleoclimate (Scheiter et al., 2012). The DGVMs allow characterisation of the global fuel load based on distribution of various biomes, but do not currently include effects of changing oxygen concentration. Simplification of the DGVM systems and addition of sensitivity to oxygen (e.g. Belcher et al. (2010),Watson and Lovelock (in press)) should allow for assessment of the negative feedback strength and

how this may have changed with the evolution of new types of land biota.

This extension should also allow for new Phanerozoic oxygen predictions, testing of hypothesised links between atmospheric O_2 and observed paleofire regimes (Scott and Glasspool, 2006) and a new falsification method based on model predictions for the abundance of fossilized charcoal.

6.5 Concluding remarks

The overriding question that has driven the work in this thesis, which was also the initial project title is:

Why does the Earth's atmosphere contain so much oxygen?
and could there be planets elsewhere with breathable atmospheres?

The title of this project was later changed to better reflect the work undertaken and the specific important results, but some thoughts on this question are considered below.

6.5.1 On Earth's oxygention

The view presented here, demonstrated by the results of the Mantle Model, is one in which the long term change between dominant weathering pathways has resulted in a gradual oxidation of the surface environment. Currently the model system cannot be extended into the Archean, but the Proterozoic results hint at an overall mechanism: On the Early Earth the heat flux from the mantle was significantly higher, and the area of the continents much less than the present day. This suggests an Earth system in which a large proportion of carbon burial occurred on the sea floor during the carbonatization of fresh mid ocean ridge basalts, rather than via the weathering of silicate rocks on land, which would likely experience extreme limitation by transport of cations due to greatly diminished continental area. Because nutrient is only transferred to the surface ocean during terrestrial weathering, this world would have much less abundant ocean nutrients, lower rates of organic carbon burial and therefore lower atmospheric O_2 concentration. Over time, the combination of a decreasing mantle heat flux and the increase in continental area (as well as improved continental weathering efficiency due to the

colonising biota) should have led to the terrestrial weathering sink becoming gradually more important, slowly increasing nutrient levels and increasing production of O_2 via carbon burial. It is argued here (and by Bjerrum and Canfield (2004)) that this interpretation can be consistent with the stability noted in carbon isotope records due to changing isotope fractionation effects over Earth history (see section 5.9).

6.5.2 On exoplanets

The research here allows for some thoughts on exoplanet evolution, but necessarily assumes Earth-like elemental composition and biogeochemical cycling regimes. On a hypothetical 'twin-Earth', oxygenation to contemporary levels should depend on the emergence and colonisation of terrestrial land masses, the resulting weathering pathway balance, and the associated supply of nutrients to the oceans. The size of the planet likely plays a very important role, as this would be expected to affect both the mantle heat flux and the mechanism of plate tectonics and resulting continental growth.

7 Electronic appendix

7.1 Simplified biogeochemical models for MATLAB

The CD-ROM on the inside cover of the hardbound thesis contains MATLAB scripts which solve the three models developed in this project. A readme file is included, which describes how to run and alter the model systems.

The code bundle can also be obtained from the UEA E-Theses Repository or by writing to either b.mills@uea.ac.uk or benjaminmills@live.com.

References

P.A. Allen and J.L. Etienne. Sedimentary challenge to snowball Earth. *Nature Geoscience*, 1(12):817–825, 2008.

J.C. Alt and D.A.H. Teagle. The uptake of carbon during alteration of oceanic crust. *Geochimica et Cosmochimica Acta*, 63:1527–1535, 1999.

M. Archer, T.F. Flannery, A. Ritchie, and R.E. Molnar. First Mesozoic mammal from Australia- an early Cretaceous monotreme. *Nature*, 318: 363–366, 1985.

E. Arnaud, G.P. Halverson, and G.A. Shields-Zhou. The geological record of Neoproterozoic glaciations. *Geological Society of London Memoir*, 36, 2011.

R.S. Arvidson, F.T. Mackenzie, and M. Guidry. MAGic: A Phanerozoic model for the geochemical cycling of major rock-forming components. *American Journal of Science*, 306:135–190, 2006.

W. Bach and K.J. Edwards. Iron and sulfide oxidation within the basaltic ocean crust: Implications for chemolithoautotrophic microbial biomass production. *Geochimica et Cosmochimica Acta*, 67(20):3871–3887, 2003.

D. Bachelet, J.M. Lenihan, C. Daly, R.P. Neilson, D.S. Ojima, and W.J. Parton. Mc1: A dynamic vegetation model for estmating the distribution of vegetation and associated ecosystem fluxes of carbon, nutrients, and water. *USDA Pac. Northwest Stn. Gen. Tech. Rep.*, PNW-GTR-508:95, 2001.

J.L. Bada, C. Bigham, and S.L. Miller. Impact melting of frozen oceans on the early Earth: implications for the origin of life. *PNAS*, 91:12481250., 1994.

E.J. Barron, J.L. Sloan, and G.G.A. Harrison. Potential significance of land-sea distribution and surface albedo variations as a climatic forcing factor: 180 my to the present. *Palaeogeography Palaeoclimatology Palaeoecology*, 30:17–40, 1980.

J.K. Bartley, M. Pope, A.H. Knoll, M.A. Semikhatov, and P.Y. Petrov. A Vendian-Cambrian boundary succession from the northwestern margin of the Siberian Platform; stratigraphy, palaeontology, chemostratigraphy and correlation. *Geological Magazine*, 135:473–494., 1998.

A. Bekker, A.J. Kaufman, J.A. Karhu, N.J. Beukes, Q.D. Swart, L.L. Coetzee, and K.A. Eriksson. Chemostratigraphy of the Paleoproterozoic Duitschland Formation, South Africa implications for coupled climate

change and carbon cycling. *American Journal of Science*, 301:261–285., 2001.

A. Bekker, J.A. Karhu, and A.J. Kaufman. Carbon isotope record for the onset of the Lomagundi carbon isotope excursion in the Great Lakes area, North America. *Earth and Planetary Science Letters*, 148:145–180, 2006.

C.M. Belcher and J.C. McElwain. Limits for combustion in low O_2 redefine paleoatmospheric predictions for the Mesozoic. *Science*, 321:1197–1200, 2008.

C.M. Belcher, J.M. Yearsley, R.M. Hadden, J.C. McElwain, and G. Rein. Baseline intrinsic flammability of Earths ecosystems estimated from paleoatmospheric oxygen over the past 350 million years. *PNAS*, 107(52): 22448–22453, 2010.

W. Benz, W.L. Slattery, and A.G.W. Cameron. The origin of the Moon and the single-impact hypothesis I. *Icarus*, 66:515–535, 1986.

N.M. Bergman. *COPSE: A New Biogeochemical Earth System Model for The Phanerozoic*. PhD thesis, University of East Anglia, 2003.

N.M. Bergman, T.M. Lenton, and A.J. Watson. COPSE: A new model of biogeochemical cycling over Phanerozoic time. *American Journal of Science*, 304(May):397–437, 2004.

R.A. Berner. Models for carbon and sulfur cycles and atmospheric oxygen: application to Paleozoic geologic history. *American Journal of Science*, 287:177–196, 1987.

R.A. Berner. Atmospheric carbon dixoide over Phanerozoic time. *Science*, 249:1382–1386, 1990.

R.A. Berner. A model for atmospheric CO_2 over Phanerozoic time. *American Journal of Science*, 291:339–376, 1991.

R.A. Berner. Geocarb II: A revised model of atmospheric CO_2 over phanerozoic time. *American Journal of Science*, 294:56–91, 1994.

R.A. Berner. The rise of plants and their effect on weathering and atmospheric CO_2. *Science*, 276:544–546, 1997.

R.A. Berner. The carbon cycle and CO_2 over Phanerozoic time: the role of land plants. *Phil. Trans. R. Soc. Lond. B*, 353:75–82, 1998.

R.A. Berner. Modeling atmospheric O_2 over Phanerozoic time. *Geochimica et Cosmochimica Acta*, 65(5):685–694, 2001.

R.A. Berner. GEOCARBSULF: A combined model for phanerozoic atmospheric O_2 and CO_2. *Geochimica et Cosmochimica Acta*, 70:5653–5664, 2006a.

R.A. Berner. Inclusion of the weathering of volcanic rocks in the GEOCARBSULF model. *American Journal of Science*, 306:295–302, 2006b.

R.A. Berner. Phanerozoic atmospheric oxygen: new results using the GEOCARBSULF model. *American Journal of Science*, 309:603–606, 2009.

R.A. Berner and E.J. Barron. Comments on the BLAG model: Factors affecting atmospheric CO_2 and temperature over the past 100 million years. *American Journal of Science*, 284:1183–1192, 1984.

R.A. Berner and D.E. Canfield. A new model for atmospheric oxygen over Phanerozoic time. *American Journal of Science*, 289:333–361, 1989.

R.A. Berner and Z. Kothavala. Geocarb III: A revised model of atmospheric CO_2 over Phanerozoic time. *American Journal of Science*, 301:182–204, 2001.

R.A. Berner, A.C. Lasaga, and R.M. Garrels. The carbonate-silicate geochemical cycle and its effect on atmospheric carbon dioxide over the past 100 million years. *American Journal of Science*, 283:641–683, 1983.

R.A. Berner, S.T. Petsch, J.A. Lake, D.J. Beerling, B.N. Popp, R.S. Lane, E.A. Laws, M.B. Westley, N. Cassar, F.I. Woodward, and W.P. Quick. Isotope fractionation and atmospheric oxygen: implications for Phanerozoic O_2 evolution. *Science*, 287:1630–1633, 2000.

E.A. Bettis, D.R. Muhs, H.M. Roberts, and A.G. Wintle. Last glacial loess in the conterminous USA. *Quarterly Science Reviews*, 22:1907–1946, 2003.

N.J. Beukes, C. Klein, A.J. Kaufman, and J.M. Hayes. Carbonate petrography, kerogen distribution, and carbon and oxygen isotope variations in an early Proterozoic transition from limestone to iron-formation deposition: Transvaal Supergroup, South Africa. *Economic Geology*, 85:663–690, 1990.

C.J. Bjerrum and D.E. Canfield. Ocean productivity before about 1.9 Gyr ago limited by phosphorus adsorption onto iron oxides. *Nature*, 417:159–162, 2002.

C.J. Bjerrum and D.E. Canfield. New insights into the burial history of organic carbon on the early Earth. *G3*, 5(8):9, 2004.

G.J.S. Bluth and L.R. Kump. Phanerozoic paleogeology. *American Journal of Science*, 291:284–308, 1991.

E.W. Bolton, R.A. Berner, and S.T. Petsch. The weathering of sedimentary organic matter as a control on atmospheric O_2. ii. theoretical modeling. *American Journal of Science*, 306(8):575–615, 2006.

F.H. Bormann, W.B. Bowden, R.S. Pierce, S.P. Hamburg, G.K. Voigt, R.C. Ingersoll, and G.E. Likens. The Hubbard Brook sandbox experiment. In W. R. Jordan, M. E. Gilpin, and J. D. Aber, editors, *Restoration ecology*, pages 251–256. Cambridge University Press., New York, 1987.

S.H. Bottrell and R.J. Newton. Reconstruction of changes in global sulfur cycling from marine sulfate isotopes. *Earth Science Reviews*, 75(1-4):59–83, 2006.

S.A. Bowring and I.S. Williams. Priscoan (4.00-4.03 ga) orthogneisses from northwestern Canada. *Contrib. Mineral Petrol*, 134:3–16, 1999.

C.K. Boyce, R.M. Hazen, and A.H. Knoll. Nondestructive, in situ, cellular-scale mapping of elemental abundances including organic carbon of permineralized fossils. *PNAS*, 98:59705974, 2001.

R.A. Boyle. *Theoretical feedbacks between Neoproterozoic glaciations and eukaryotic evolution*. PhD thesis, University of East Anglia, 2008.

R.A. Boyle, T.M. Lenton, and H.T.P. Williams. Neoproterozoic snowball Earth glaciations and the evolution of altruism. *Geobiology*, 5(4):337–349, 2007.

P.V. Brady and S.R. Gislason. Seafloow weathering controls on atmospheric CO_2 and global cimate. *Geochimica et Cosmochimica Acta*, 61:965–973, 1997.

C.K.B. Brain, A.R. Prave, K.-H. Hoffmann, A.E. Fallick, A. Botha, D.A. Herd, C. Sturrock, I. Young, D.J. Condon, and S.G. Allison. The first animals: ca. 760-million-year-old sponge-like fossils from Namibia. *South African Journal of Science*, 108:658, 2012.

J.J. Brocks, G.A. Logan, and R. Buick. Archean molecular fossils and the early rise of eukaryotes. *Science*, 285:1033–1036, 1999.

W.S. Broecker and T.-H. Peng. *Tracers in the sea.* Eldigio, New York, 1982.

N.J. Butterfield. Bangiomorpha pubescens n. gen., n. sp.: implications for the evolution of sex, multicellularity, and the Mesoproterozoic/Neoproterozoic radiation of eukaryotes. *Paleobiology*, 26:389–404, 2000.

K. Caldeira. Long-term control of atmospheric carbon dioxide: low temperature seafloor alteration or terrestrial silicate rock weathering. *American Journal of Science*, 295:1077–1114, 1995.

K. Caldeira and J.F. Kasting. The life span of the biosphere revisited. *Nature*, 360:721–723, 1992.

D.E. Canfield. A new model for Proterozoic ocean chemistry. *Nature*, 396 (6710):450–453, 1998.

D.E. Canfield. The evolution of the Earth surface sulphur reservoir. *American Journal of Science*, 304:839–861, 2004.

D.E. Canfield. The early history of atmospheric oxygen. *Annu. Rev. Earth Planet. Sci.*, 33:1–36, 2005.

D.E. Canfield and J. Farquhar. Animal evolution, bioturbation, and the sulfate concentration of the oceans. *PNAS*, 106(20):8123–8127, 2008.

D.E. Canfield and A. Teske. Late Proterozoic rise in atmospheric oxygen concentration inferred from phylogenetic and sulphur-isotope studies. *Nature*, 382:127–132, 1996.

D.E. Canfield and B. Thamdrup. The production of ^{34}S-depleted sulfide during bacterial disproportionation of elemental sulfur. *Science*, 266(5193): 1973–1975, 1994.

D.E. Canfield, S.W. Poulton, and G.M. Narbonne. Late-Neoproterozoic deep-ocean oxygenation and the rise of animal life. *Science*, 315:92–95, 2007.

D.E. Canfield, S.W. Poulton, A.H. Knoll, G.M. Narbonne, G. Ross, T. Goldberg, and H. Strauss. Ferruginous conditions dominated later Neoproterozoic deep-water chemistry. *Science*, 321:949–952, 2008.

R.M. Canup and E. Asphaug. Origin of the Moon in a giant impact near the end of the Earth's formation. *Nature*, 461:708–712, 2001.

D.C. Catling, K.J. Zahnle, and C.P. McKay. Biogenic methane, hydrogen escape, and the irreversible oxidation of early Earth. *Science*, 293:839–843, 2001.

D.C. Catling, C.R. Glein, K.J. Zahnle, and C.P. McKay. Why O_2 is required by complex life on habitable planets and the concept of planetary oxygenation time. *Astrobiology*, 5(3):415–438, 2005.

J.L. Cawley, R.C. Burruss, and H.D. Holland. Chemical weathering in central Iceland: an analog of pre-Silurian weathering. *Science*, 165:391–392, 1969.

T.E. Cerling. Carbon dioxide in the atmosphere: evidence from Cenozoic and Mesozoic paleosols. *American Journal of Science*, 291:377–400, 1991.

J.E. Chambers. Planetary accretion in the inner solar system. *Earth and Planetary Science Letters*, 223:241–252, 2004.

R.J. Charlson, J.E. Lovelock, M.O. Andrewec, and S.G. Warren. Oceanic phytoplankton, atmospheric sulfur, coud albedo and climate. *Nature*, 326: 655–661, 1987.

M.W. Claire, D.C. Catling, and A.K.J. Zahnle. Biogeochemical modelling of the rise in atmospheric oxygen. *Geobiology*, 2006.

S.A. Clough, M.W. Shephard, E.J. Mlawer, J.S. Delamere, M.J. Iacono, K. Cady-Pereira, S. Boukabara, and P.D. Brown. Atmospheric radiative transfer modeling: a summary of the AER codes. *Journal of Quantitative Spectroscopy Radiative Transfer*, 91:233–244, 2005.

K.C. Condie. Episodic continental growth and supercontinents: a mantle avalanche connection? *Earth and Planetary Science Letters*, 163(97108.), 1998.

D. Condon, M. Zhu, S. Bowring, W. Wang, A. Yang, and Y. Jin. U-pb ages from the Neoproterozoic Doushantuo Formation, China. *Science*, 308:95–98, 2005.

P.J. Cook and J.H. Shergold. Phosphorus, phosphorites and skeletal evolution at the Precambrian Cambrian boundary. *Nature*, 308(5956):231–236, 1984. ISI Document Delivery No.: SH155 Times Cited: 86 Cited Reference Count: 75.

T.J. Crowley. *Tectonic Boundary Conditions for Climate Reconstructions*. Oxford University Press, New York, 1998.

T.W. Dahl, E.U. Hammarlund, A.D. Anbar, D.P.G. Bond, B.C. Gill, G.W. Gordon, A.H. Knoll, A.T. Nielsen, N.H. Schovsbo, and D.E. Canfield. Devonian rise in atmospheric oxygen correlated to the radiations of terrestrial plants and large predatory fish. *PNAS*, 107(42):17911–17915, 2010.

N. Dauphas and J.F. Kasting. Low pCO_2 in the pore water, not in the Archean air. *Nature*, 474:E2–E3, 2011.

L.A. Derry. A burial diagenesis origin for the Ediacaran Shuram-Wonoka carbon isotope anomaly. *Earth and Planetary Science Letters*, 294:152–162, 2010.

L.A. Derry, A.J. Kaufman, and S.B. Jacobsen. Sedimentary cycling and environmental changes in the late Proterozoic: Evidence from stable and radiogenic isotopes. *Geochimica et Cosmochimica Acta*, 56:1317–1329, 1992.

D.J. Des Marais. Isotopic evolution of the biogeochemical carbon cycle during the Proterozoic Eon. *Organic Geochemistry*, 27:185–193, 1997.

C. Dessert, B. Dupre, J. Gaillardet, L.M. Francois, and C.J. Allegre. Basalt weathering laws and the impact of basalt weathering on the global carbon cycle. *Chemical Geology*, 202:257–273, 2003.

J.L. Dixon, A.S. Hartshorn, A.M. Heimsath, R.A. DiBiase, and K.X. Whipple. Chemical weathering response to tectonic forcing: A soils perspective from the San Gabriel Mountains, California. *Earth and Planetary Science Letters*, 323-324:40–49, 2012.

Y. Donnadieu, F. Fluteau, G. Ramstein, C. Ritz, and J. Besse. Is there a conflict between the Neoproterozoic glacial deposits and the snowball Earth interpretation: an improved understanding with numerical modeling. *Earth and planetary science letters*, 208:101–112, 2003.

Y. Donnadieu, Y. Godderis, G. Ramstein, A. Nedelec, and J. Meert. A 'snowball earth' climate triggered by continental break-up through changes in runoff. *Nature*, 428(6980):303–306, 2004. ISI Document Delivery No.: 803SG Times Cited: 65 Cited Reference Count: 30.

J.I. Drever. The effect of land plants on weathering rates of silicate minerals. *Geochimica et Cosmochimica Acta*, 58(10):2325–2332, 1994.

H. Elderfield and A. Schultz. Mid-ocean ridge hydrothermal fluxes and the chemical composition of the ocean. *Annu. Rev. Earth Planet. Sci.*, 24: 191–224, 1996.

D.A. Evans, N.J. Beukes, and J.L. Kirschivink. Low-latitude glaciation in the Paleoproterozoic era. *Nature*, 386:262–266, 1997.

J. Farquhar, H. Bao, and M. Thiemens. Atmospheric influence of Earth's earliest sulphur cycle. *Science*, 289:756–758, 2000.

E. Font, A. Ndlec, R.I.F. Trindade, and C. Moreau. Fast or slow melting of the Marinoan snowball Earth? the cap dolostone record. *Palaeogeography, Palaeoclimatology, Palaeoecology*, 295(1-2):215–225, 2010.

S. Franck and C. Bounama. Continental growth and volatile exchange during Earth's evolution. *Physics of the Earth and planetary interiors*, 100:189–196, 1997.

S. Franck, K. Kossacki, and C. Bounama. Modelling the global carbon cycle for the past and future evolution of the Earth system. *Chemical Geology*, 159:305–317, 1999.

L.M. Francois and J.C.G. Walker. Modelling the Phanerozoic carbon cycle and climate: constraints from the 87sr/86sr isotopic ratio of seawater. *American Journal of Science*, 292:81–135, 1992.

K.H. Freeman and J.M. Hayes. Fractionation of carbon isotopes by phytoplankton and estimates of ancient CO_2 levels. *Global Biogeochemical Cycles*, 6:185198, 1992.

R. Frei, C. Gaucher, S.W. Poulton, and D.E. Canfield. Fluctuations in Precambrian atmospheric oxygenation recorded by chromium isotopes. *Nature*, 461:250–253, 2009.

I. Fridovich. Oxygen is toxic! *Bioscience*, 27(7):462–466, 1977.

W.S. Fyfe. The evolution of the Earths crust: modern plate tectonics to ancient hot spot tectonics. *Chemical Geology*, 23(89114.), 1978.

S. Gaffin. Ridge volume dependence on seafloor generation rate and inversion using long term sealevel change. *American Journal of Science*, 287:596–611, 1987.

J. Gaillardet, B. Dupre, P. Louvat, and C.J. Alle'gre. Global silicate weathering and CO_2 consumption rates deduced from the chemistry of large rivers. *Chemical Geology*, 159:3–30, 1999.

R.M. Garrels and A. Lerman. Coupling the sedimentary sulfur and carbon cycles - an improved model. *American Journal of Science*, 284:989–1007, 1984.

R.M. Garrels and F.T. Mackenzie. Sedimentary rock types: relative proportions as a function of geological time. *Science*, 163:570–571, 1969.

I.J. Glasspool and A.C. Scott. Phanerozoic concentrations of atmospheric oxygen reconstructed from sedimentary charcoal. *Nature Geoscience*, 3: 627–630, 2010.

Y. Godderis, Y. Donnadieu, A. Nedelec, B. Dupre, C. Dessert, A. Grard, G. Ramstein, and L.M. Francois. The Sturtian snowball glaciation: fire and ice. *Earth and planetary science letters*, 211:1–12, 2003.

C. Goldblatt and K.J. Zahnle. Faint young sun paradox remains. *Nature*, 474:E3–E4, 2011.

C. Goldblatt, T.M. Lenton, and A.J. Watson. Bistability of atmospheric oxygen and the Great Oxidation. *Nature*, 443(7112):683–686, 2006.

C. Goldblatt, M.W. Claire, T.M. Lenton, A.J. Matthews, A. J.Watson, and K.J. Zahnle. Nitrogen-enhanced greenhouse warming on early Earth. *Nature Geoscience*, 2:891–896, 2009a.

C. Goldblatt, T.M. Lenton, and A.J. Watson. An evaluation of the long-wave radiative transfer code used in the Met Office Unified Model. *Quarterly journal of the Royal Meterological Society*, 2009b.

J.P. Grotzinger and A.H. Knoll. Stromatolites in Precambrian carbonates: evolutionary mileposts or environmental dipsticks? *Annu. Rev. Earth Planet. Sci.*, 27:313–358, 1999.

L.B. Gustafson and J.P. Hunt. The porphyry copper deposit at el salvador, chile. *Economic Geology*, 70:857–912, 1975.

G.P. Halverson, P.F. Hoffman, D.P. Schrag, A.C. Maloof, and A.H.N. Rice. Toward a Neoproterozoic composite carbon-isotope record. *GSA bulletin*, 117:1181–1207, 2005.

G.P. Halverson, B.P. Wade, M.T. Hurtgen, and K.M. Barovich. Neoproterozoic chemostratigraphy. *Precambrian research*, 182:337–350, 2010.

J. Hansen, M. Sato, R. Ruedy, K. Lo, D.W. Lea, and M. Medina-Elizade. Globl temperature change. *PNAS*, 103(39):14288–14293, 2006.

J.D. Haqq-Misra, S.D. Domagal-Goldman, P.J. Kasting, and J.F. Kasting. A revised, hazy methane greenhouse for the Archean Earth. *Astrobiology*, 8(6):1127–1137, 2008.

M. Harada, E. Tajika, and Y. Sekin. Modeling a rise of atmospheric oxygen induced by Paleoproterozoic snowball Earth event (conference paper). *22nd annual V. M. Goldschmidt Conference*, 2012.

L.A. Hardie. Secular variation in seawater chemistry: An explanation for the coupled secula variation in the mineralologies of marine limestones and potash evaporites over the past 600 m.y. *Geology*, 24(3):279–283, 1996.

W.K. Hartmann and D. Davis. Satellite-sized planetesimals and lunar origin. *Icarus*, 24:504–515, 1975.

C.J. Hawkesworth, B. Dhuime, A.B. Pietranik, P.A. Cawood, A.I.S. Kemp, and C.D. Storey. The generation and evolution of the continental crust. *Journal of the Geological Society*, 167:229–248, 2010.

J.M. Hayes and J.R. Waldbauer. The carbon cycle and associated redox processes through time. *Phil. Trans. R. Soc. B*, 361:931–950, 2006.

J.M. Hayes, H. Strauss, and A.J. Kaufman. The abundance of ^{13}C in marine organic matter and isotopic fractionation in the global biogeochemical cycle of carbon during the past 800 Ma. *Chemical Geology*, 161(103125), 1999.

D.S. Heckman, D.M. Geiser, B.R. Eidell, R.L. Stauffer, N.L. Kardos, and S.B. Hedges. Molecular evidence for the early colonization of land by fungi and plants. *Science*, 293(5532):1129–1133, 2001.

D.P.L. Heron, G. Cox, A. Trundley, and A. Collins. Sea ice-free conditions during the Sturtian glaciation (early Cryogenian), South Australia. *Geology*, 39:31–34, 2011.

A.M. Hessler, D.R. Lowe, R.L. Jones, and D.K. Bird. A lower limit for atmospheric carbon dioxide levels 3.2 billion years ago. *Nature*, 428:736–738, 2004.

J.A. Higgins and D.P. Schrag. Aftermath of a snowball Earth. *G3*, 4(3), 2003.

I.A. Hilburn, J.L. Kirschvink, E. Tajika, R. Tada, Y. Hamano, and S. Yamamoto. A negative fold test on the Lorrain Formation of the Huronian Supergroup: Uncertainty on the paleolatitude of the Paleoproterozoic Gowganda glaciation and implications for the great oxygenation event. *Earth and Planetary Science Letters*, 232:315–332, 2005.

D.R. Hilton, T.P. Fischer, and B. Marty. Noble gases and volatile recycling at subduction zones. In D. Porcelli, C.J. Ballentine, and R. Wieler, editors, *Noble Gases in Geochemistry and Cosmochemistry*. Mineralogical Society of America, Washington, D.C., 2002.

P.F. Hoffman and Z.-X. Li. A palaeogeographic context for Neoproterozoic glaciation. *Palaeogeography Palaeoclimatology Palaeoecology*, 277:158–172, 2009.

P.F. Hoffman and D.P. Schrag. The snowball Earth hypothesis: testing the limits of global change. *Terra Nova*, 14:129–155, 2002.

P.F. Hoffman, A.J. Kaufman, G.P. Halverson, and D.P. Schrag. A Neoproterozoic snowball Earth. *Science*, 281:1342–1346, 1998.

K.-H. Hoffmann, D.J. Condon, S.A. Bowring, and J.L. Crowley. U-Pb zircon date from the Neoproterozoic Ghaub Formation, Namibia: Constraints on Marinoan glaciation. *Geology*, 32:817–820, 2004.

H.J. Hofmann. Precambrian microflora, Belcher Islands, Canada: Significance and systematics. *Journal of Paleontology*, 50:1040–1073, 1976.

H.J. Hofmann. Archean stromatolites as microbial archives. In R. Riding and S.M. Awramik, editors, *Microbial Sediments*, pages 315–327. Springer-Verlag, Berlin, 2000.

H.D. Holland. *The chemistry of the atmosphere and oceans.* Interscience, New York, 1978.

H.D. Holland. The phosphate-oxygen connection. *Eos (Transactions, American Geophysical Union)*, 75(3):p. OS96., 1994.

H.D. Holland. The oxygenation of the atmosphere and oceans. *Phil. Trans. R. Soc. B*, 361:903–915, 2006.

H.D. Holland. Why the atmosphere became oxygenated: A proposal. *Geochimica et Cosmochimica Acta*, 73:5241–5255, 2009.

W.T. Holser, M. Schidlowski, F.T. Mackenzie, and J.B. Maynard. Geochemical cycles of carbon and sulfur. In C. B. Gregor, R. M. Garrels, F. T. Mackenzie, and J. B. Maynard, editors, *Chemical Cycles in the Evolution of the Earth*, pages 105–173. Wiley-Interscience., New York, 1988.

J. Horita, H. Zimmermann, and H.D. Holland. Chemical evolution of seawater during the Phanerozoic: Implications from the record of marine evaporates. *Geochimica et Cosmochimica Acta*, 66:37333756, 2002.

R.J. Horodyski and L.P. Knauth. Life on land in the Precambrian. *Science*, 263:494–498, 1994.

C.H. House, J.W. Schopf, K.D. McKeegan, C.D. Coath, T.M. Harrison, and K.O. Stetter. Carbon isotopic composition of individual Precambrian microfossils. *Geology*, 28:707710, 2000.

P.M. Hurley and J.R. Rand. Pre-drift continental nuclei. *Science*, 164: 12291242., 1969.

ICS. (International Commision on Stratigraphy) International chronostratigraphic chart. **http://www.stratigraphy.org**. 2012.

A.U. Igamberdiev and P.J. Lea. Land plants equilibrate O_2 and CO_2 concentrations in the atmosphere. *Photosynthesis Research*, 87(2):177–194, 2006.

W.A. Jackson and R.J. Volk. Photorespiration. *Annu. rev. plant. physiol.*, 1970.

D. T. Johnston, F. A. Macdonald, B. C. Gill, P.F. Hoffman, and D.P. Schrag. Uncovering the Neoproterozoic carbon cycle. *Nature*, 483:320–323, 2012.

T. Jones and W. Chaloner. Fossil charcoal, its recognition and palaeoatmospheric significance. *Palaeogeography, Palaeoclimatology, Palaeoecology*, 97:3950, 1991.

B.B. Jorgensen. A thiosulfate shunt in the sulfur cycle of marine sediments. *Science*, 249(4965):152–154, 1990.

L.C. Kah and J.K. Bartley. Effect of marine carbon reservoir size on the duration of carbon isotope excursions: Interpreting the Mesoproterozoic carbon isotope record. *Geological Society of America Abstracts with Programs*, 36(5,):p.78., 2004.

L.C. Kah and R. Riding. Mesoproterozoic carbon dioxide levels inferred from calcified cyanobacteria. *Geology*, 35:799–802, 2007.

L.C. Kah, T.W. Lyons, and T.D. Frank. Lowmarine sulphate and protracted oxygenation of the Proterozoic biosphere. *Nature*, 431:834–838, 2004.

J.A. Karhu and H.D. Holland. Carbon isotopes and the rise of atmospheric oxygen. *Geology*, 24:867–870, 1996.

S.A. Kasemann, C.J. Hawkesworth, A.R. Prave, A.E. Fallick, and P.N. Pearson. Boron and calcium isotope composition in Neoproterozoic carbonate rocks from Namibia: evidence for extreme environmental change. *Earth and planetary science letters*, 231:73–86, 2005.

J.F. Kasting. Theoretical constraints on oxygen and carbon dioxide concentrations in the Precambrian atmosphere. *Precambrian Research*, 34: 205–229, 1987.

J.F. Kasting. Long-term stability of the Earth's climate. *Palaeogeography Palaeoclimatology Palaeoecology*, 75:83–95, 1989.

J.F. Kasting. Earth's early atmosphere. *Science*, 259(5097):920–926, 1993.

J.F. Kasting. The rise of atmospheric oxygen. *Science*, 293(5531):819–820, 2001.

J.F. Kasting and S. Ono. Paleoclimates: the first two billion years. *Phil. Trans. R. Soc. B*, 361:917929, 2006.

A.J. Kaufman and S. Xiao. High CO_2 levels in the Proterozoic atmosphere estimated from analyses of individual microfossils. *Nature*, 425(279-282), 2003.

A.J. Kaufman, J.M. Hayes, and C. Klein. Primary and diagenetic controls of isotopic compositions of iron-formation carbonates. *Geochimica et Cosmochimica Acta*, 54:3461–3473, 1990.

M. Kennedy, M. Droser, L.M. Mayer, D. Pevear, and D. Mrofka. Late Precambrian oxygenation; inception of the clay mineral factory. *Science*, 311 (5766):1446–1449, 2006.

J.L. Kirschvink. *Late Proterozoic Low-Latitude Global Glaciation: the Snowball Earth*. The Proterozoic Biosphere: A Multidisciplinary Study. Cambridge University Press, 1992.

J.L. Kirschvink, E.J. Gaidos, L.E. Bertani, N.J. Beukes, J. Gutzmer, L.N. Maepa, and R.E. Steinberger. Paleoproterozoic snowball Earth: Extreme climatic and geochemical global change and its biological consequences. *PNAS*, 97:1400–1405, 2000.

L.P. Knauth and M.J. Kennedy. The late Precambrian greening of the Earth. *Nature*, 460(7256):728–732, 2009.

A.H. Knoll. *Life on a Young Planet: The First Three Billion Years of Evolution on Earth*. Princeton University Press, Princeton, N. J., 2003.

A.H. Knoll and E.S. Barghoorn. Archean microfossils showing cell division from the Swaziland System of South Africa. *Science*, 198:396398, 1977.

A.H. Knoll and S.B. Carroll. Early animal evolution: Emerging views from comparative biology and geology. *Science*, 284:2129–2137, 1999.

M.A. Knoll and W.C. James. Effect of the advent and diversification of vascular land plants on mineral weathering through geologic time. *Geology*, 15(12):1099–1102, 1987.

R.E. Kopp, J.L. Kirschvink, I.A. Hilburn, and C.Z. Nash. The Paleoproterozoic snowball Earth: A climate disaster triggered by the evolution of oxygenic photosynthesis. *PNAS*, 102(32):11131–11136, 2005.

A.B. Kudryavtsev, J.W. Schopf, D.G. Agresti, and T.J. Wdowiak. In situ laser-Raman imagery of Precambrian microscopic fossils. *PNAS*, 98:823–826, 2001.

L.R. Kump. Terrestrial feedback in atmospheric oxygen regulation by fire and phosphorus. *Nature*, 335:152–154, 1988.

L.R. Kump. The coupling of the carbon and sulfur biogeochemical cycles over Phanerozoic time. In R. Wollast, F. T. Mackenzie, and L. Chou, editors, *Interactions of C, N, P and S Biogeochemical Cycles and Global Change*, pages 475–790. Springer-Verlag, Berlin, 1993.

L.R. Kump. The rise of atmospheric oxygen. *Nature*, 451:277–278, 2008.

L.R. Kump and R.M. Garrels. Modeling atmospheric O_2 in the global sedimentary redox cycle. *American Journal of Science*, 286:337–360, 1986.

L.R. Kump, J. Kasting, and M.B. . Rise of atmospheric oxygen and the upside-down Archean mantle. *G3*, 2(1):2000GC000144, 2001.

A.C. Lasaga and H. Ohmoto. The oxygen geochemical cycle: Dynamics and stability. *Geochimica et Cosmochimica Acta*, 66(3):361–381, 2002.

A.C. Lasaga, R.A. Benrner, and R.M. Garrels. An improved geochemical model of atmospheric CO_2 fluctiations over the past 100 million years. In The carbon cycle and atmospheric CO_2: Natural variations Archean to present. *Geophysical Monographs*, 32:397–411, 1985.

G. Le Hir, G. Ramstein, Y. Donnadieu, and Y. Godderis. Scenario for the evolution of atmospheric pCO_2 during a snowball Earth. *Geology*, 36(1): 47–50, 2008.

G. Le Hir, Y. Donnadieu, Y. Goddris, R.T. Pierrehumbert, G.P. Halverson, M. Macouin, A. Ndlec, and G. Ramstein. The snowball Earth aftermath: Exploring the limits of continental weathering processes. *Earth and planetary science letters*, 277:453–463, 2009.

J. Leather, P.A. Allen, M.D. Brasier, and A. Cozzi. Neoproterozoic snowball Earth under scrutiny: Evidence from the Fiq glaciation of Oman. *Geology*, 30:891–894, 2002.

T.M. Lenton. Land and ocean carbon cycle feedback effects on global warming in a simple Earth system model. *Tellus Series B-Chemical and Physical Meteorology*, 52(5):1159–1188, 2000.

T.M. Lenton and W.v. Bloh. Biotic feedback extends the life span of the biosphere. *Geophysical Research Letters*, 28(9):1715–1718, 2001.

T.M. Lenton and A.J. Watson. Redfield revisited: I. Regulation of nitrate, phosphate and oxygen in the ocean. *Global Biogeochemical Cycles.*, 14: 225–248, 2000a.

T.M. Lenton and A.J. Watson. Redfield revisited: II. What regulates the oxygen content of the atmosphere? *Global biogeochemical cycles*, 14:249–268, 2000b.

T.M. Lenton and A.J. Watson. Biotic enhancement of weathering, atmospheric oxygen and carbon dioxide in the Neoproterozoic. *Geophysical reseacrh letters*, 31, 2004.

T.M. Lenton and A.J. Watson. *Revolutions that made the Earth*. Oxford University Press, Oxford, UK, 2011.

T.M. Lenton, M.S. Williamson, N.R. Edwards, R. Marsh, A.R. Price, A.J. Ridgwell, J.G. Shepherd, S.J. Cox, and T.G. Team. Millennial timescale carbon cycle and climate change in an efficient Earth system model. *Climate Dynamics*, 26(7-8):687–711, 2006.

T.M. Lenton, M. Crouch, M. Johnson, N. Pires, and L. Dolan. First plants cooled the Ordovician. *Nature Geoscience*, 5:86–89, 2012.

E. Lewis and D.W.R. Wallace. Program developed for CO_2 system calculations. *ORNL/CDIAC-105. Carbon Dioxide Information Analysis Center, Oak Ridge National Laboratory, U.S. Department of Energy, Oak Ridge, Tennessee*, 1998.

J.P. Lewis, A.J. Weaver, and M. Eby. Snowball versus slushball Earth: Dynamic versus nondynamic sea ice? *Journal of Geophysical Research*, 112: C11014, 2007.

Z.-X.A. Li and C.-T.A. Lee. The constancy of upper mantle fO_2 through time inferred from V/Sc ratios in basalts. *Earth and Planetary Science Letters*, 228:483–493, 2004.

Z.X. Li, S.V. Bogdanova, A.S. Collins, A. Davidson, B.D. Waele, R.E. Ernst, I.C.W. Fitzsimons, R.A. Fuck, D.P. Gladkochub, J. Jacobs, K.E. Karlstrom, S. Lu, L.M. Natapov, V. Pease, S.A. Pisarevsky, K. Thrane, and V. Vernikovsky. Assembly, configuration, and break-up history of Rodinia: A synthesis. *Precambrian Research*, 160:179–210, 2008.

J.E. Lovelock. Gaia as seen through the atmosphere. *Atmospheric Environment*, 6:579–580, 1972.

J.E. Lovelock. *Gaia: A new look at life on Earth.* Oxford University Press, Oxford, UK, 1979.

R.P. Lowell and S.M. Keller. High-temperature seafloor hydrothermal circulation over geologic time and Archean banded iron formations. *Geophysical Research Letters*, 30(7), 2003.

F.A. Macdonald, M.D. Schmitz, J.L. Crowley, C.F. Roots, D.S. Jones, A.C. Maloof, J.V. Strauss, P.A. Cohen, D.T. Johnston, and D.P. Schrag. Calibrating the Cryogenian. *Science*, 327:1241–1243, 2010.

L. Margulis and J.E. Lovelock. Biological modulation of the Earth's atmosphere. *Icarus*, 21:471–489, 1974.

J. Marotzke, R. Giering, K.Q. Zhang, D. Stammer, C. Hill, and T.Lee. Construction of the adjoint MIT ocean general circulation model and application to atlantic heat transport variability. *Journal of Geophysical Research*, 104(29):529–547, 1999.

J.C. McElwain and W.G. Chaloner. Stomatal density and index of fossil plants track atmospheric carbon dioxide in the Palaeozoic. *Annals of Botany*, 76:389–395, 1995.

C. McKay. Thickness of tropical ice and photosynthesis on a snowball Earth. *Geophysical Research Letters*, 27(14), 2000.

S.M. McLennan and S.R. Taylor. Continental freeboard, sedimentation rates and frowth of continental crust. *Nature*, 306:169–172, 1983.

V.A. Melezhik, A.E. Fallick, P.V. Medvedev, and V.V. Makarikhin. Extreme $^{13}C_{carb}$ enrichment in ca. 2.0 ga magnesite-stromatolite-dolomite-red beds association in a global context: a case for the world-wide signal enhanced by a local environment. *Earth Science Reviews*, 48:71–120, 1999.

R. Millot, J. Gaillardet, B. Dupre, and C.J. Allegre. The global control of silicate weathering rates and the coupling with physical erosion: new insights from rivers of the canadian shield. *Earth and planetary science letters*, 196:83–98, 2002.

B. Mills, A.J. Watson, C. Goldblatt, R. Boyle, and T.M. Lenton. Timing of Neoproterozoic glaciations linked to transport-limited global weathering. *Nature Geoscience*, 4:861–864, 2011.

S.J. Mojzsis, G. Arrhenius, K.D. McKeegan, T.M. Harrison, A.P. Nutman, and C.R.L. Friend. Evidence for life on Earth before 3,800 million years ago. *Nature*, 384:55–59, 1996.

W.G. Mook. ^{13}C in atmospheric CO_2. *Netherlands Journal of Sea Research*, 20:211–223, 1986.

K.L. Moulton and R.A. Berner. The eect of higher land plants on the weathering of calcium and magnesium silicates in Iceland. *Geological Society of America Meeting Abstracts*, 339, 1996.

J. ONeil, R.W. Carlson, D. Francis, and R.K. Stevenson. Neodymium-142 evidence for Hadean mafic crust. *Science*, 321:1828–1831, 2008.

B.L. Otto-Bliesner. Continental drift, runoff and weathering feedbacks: Implications from climate model experiments. *Journal of Geophysical Research*, 100:11537–11548, 1995.

M. Pagani, M.A. Arthur, and K.H. Freeman. Miocene evolution of atmospheric carbon dioxide. *Paleoceanography*, 14:273292, 1999.

D. Papineau. Global biogeochemical changes at both ends of the Proterozoic: Insights from phosphorites. *Astrobiology*, 10(2):165–181, 2010.

D. Papineau, S.J. Mojzsis, and A.K. Schmitt. Multiple sulfur isotopes from paleoproterozoic huronian interglacial sediments and the rise of atmospheric oxygen. *Earth and Planetary Science Letters*, 255:188–212, 2007.

A. Pavlov and J. Kasting. Mass-independent fractionation of sulfur isotopes in Archean sediments: strong evidence for an anoxic Archean atmosphere. *Astrobiology*, 2:2741, 2002.

A.A. Pavlov, M.T. Hurtgen, J.F. Kasting, and M.A. Arthur. Methane-rich Proterozoic atmosphere? *Geology*, 31:87–90, 2003.

A. Paytan and K. McLaughlin. The oceanic phosphorus cycle. *Chemical Reviews*, 107:563–578, 2007.

P.N. Pearson and M.R. Palmer. Atmospheric carbon dioxide concentrations over the past 60 million years. *Nature*, 406:695699, 2000.

R.T. Pierrehumbert. Climate dynamics of a hard snowball Earth. *Journal of Geophysical Research*, 110, 2005.

N.J. Planavsky, O.J. Rouxel, A. Bekker, S.V. Lalonde, K.O. Konhauser, C.T. Reinhard, and T.W. Lyons. The evolution of the marine phosphate reservoir. *Nature*, 467:1088–1090, 2010.

A. Polat, A.W. Hofmann, and M.T. Rosing. Boninite-like volcanic rocks in the 3.7-3.8 Ga Isua greenstone belt, West Greenland: geochemical evidence for intra-oceanic subduction zone processes in the early Earth. *Chemical Geology*, 184:231–254, 2002.

D. Pollard and J.F. Kasting. Snowball Earth: A thin-ice solution with flowing sea glaciers. *Journal of Geophysical Research*, 110:C07010, 2005.

S.M. Porter, A.H. Knoll, and P. Affaton. Chemostratigraphy of Neoproterozoic cap carbonates from the Volta Basin, West Africa. *Precambrian research*, 130:99–112, 2004.

A.R. Prave. Life on land in the Proterozoic: Evidence from the Torridonian rocks of northwest Scotland. *Geology*, 30:811–914, 2002.

R. Raiswell and R.A. Berner. Pyrite and organic matter in Phanerozoic normal marine shales. *Geochimica et Cosmochimica Acta*, 50:1967–1976, 1986.

R. Raiswell and D.E. Canfield. Sources of iron for pyrite formation in marine sediments. *American Journal of Science*, 298(3):219–245, 1998.

B. Rasmussen, I.R. Fletcher, J.J. Brocks, and M.R. Kilburn. Reassessing the first appearance of eukaryotes and cyanobacteria. *Nature*, 455:1101–1105, 2008.

C.E. Rees. The sulphur isotope balance of the ocean: an improved model. *Earth and Planetary Science Letters*, 7:366370, 1970.

C.T. Reinhard and N.J. Planavsky. Mineralogical constraints on Precambrian pCO_2. *Nature*, 474:E1–E2, 2011.

J.A. Resing, J.E. Lupton, R.A. Feely, and M.D. Lilley. CO_2 and 3He in hydrothermal plumes: implications for mid-ocean ridge CO_2 flux. *Earth and Planetary Science Letters*, 226:449–464, 2004.

G.J. Retallack. Early forest soils and their role in Devonian global change. *Science*, 276:583–585, 1997.

G.J. Retallack. *Soils of the Past, an Introduction to Pedology.* Blackwell Science, Oxford, 2001.

D.C. Rhoads and J.W. Morse. Evolutionary and ecologic significance of oxygen-deficient marine basins. *Lethaia*, 4(4):413–428, 1971.

A. Ridgwell and J. Hargreaves. Regulation of atmospheric CO_2 by deep-sea sediments in an Earth system model. *Global Biogeochemical Cycles*, 21 (GB2008,), 2007.

A. Ridgwell and D.N. Schmidt. Past constraints on the vulnerability of marine calcifiers to massive carbon dioxide release. *Nature Geoscience*, 3: 196 – 200, 2010.

A.J. Ridgwell, M.J. Kennedy, and K. Caldeira. Carbonate deposition, climate stability, and Neoproterozoic ice ages. *Science*, 302:859–862, 2003.

C.S. Riebe, J.W. Kirchner, and R.C. Finkel. Erosional and climatic effects on long-term chemical weathering rates in granitic landscapes spanning diverse climate regimes. *Earth and planetary science letters*, 224:547–562, 2004.

S. Rino, T. Komiya, B.F. Windley, I. Katayama, A. Motoki, and T. Hirata. Major episodic increases of continental crustal growth determined from zircon ages of river sands; implications for mantle overturns in the Early Precambrian. *Physics of the Earth and planetary interiors*, 146:369–394, 2004.

A.B. Ronov. Global carbon geochemistry, volcanism, carbonate accumilation, and life. *Geochemistry International*, 13:172–195, 1976.

A.B. Ronov. *StratisferaIli Osadochnaya Obolochka Zemli (Kolichestvennoe Issledovanie)*. Moskva, 1993.

M.T. Rosing, D.K. Bird, N.H. Sleep, and C.J. Bjerrum. No climate paradox under the faint early sun. *Nature*, 464:744–749, 2010.

D.H. Rothman. Atmospheric carbon dioxide levels for the last 500 million years. *PNAS*, 99(7):4167–4171, 2001.

D.H. Rothman, J.M. Hayes, and R.E. Summons. Dynamics of the Neoproterozoic carbon cycle. *PNAS*, 100(14):8124–8129, 2003.

N.P. Rowe and T.P. Jones. Devonian charcoal. *Palaeogeography Palaeoclimatology Palaeoecology*, 164:331–338, 2000.

D.B. Rowley. Rate of plate creation and destruction: 180 Ma to present. *Geological Society of America Bulletin*, 114(8):927–933, 2002.

D.L. Royer, R.A. Berner, I.P. Montaez, N.J. Tabor, and D.J. Beerling. CO_2 as a primary driver of Phanerozoic climate. *GSA Today*, 14(3):4–10, 2004.

C.V. Rubinstein, P. Gerrienne, G.S.d.l. Puente, R.A. Astini, and P. Steemans. Early Middle Ordovician evidence for land plants in Argentina (eastern Gondwana). *New Phytologist*, 188:365–369, 2010.

B. Runnegar. Precambrian oxygen levels estimated from the biochemistry and physiology of early eukaryotes. *Global and Planetary Change*, 5(1-2): 97–111, 1991.

R. Rye and H.D. Holland. Paleosols and the evolution of atmospheric oxygen: a critical review. *American Journal of Science*, 298(8):621–672, 1998.

R. Rye, P.H. Kuo, and H.D. Holland. Atmospheric carbon dioxide concentrations before 2.2 billion years ago. *Nature*, 378:603–605, 1995.

A.E. Saal, E.H. Hauri, C.H. Langmuir, and M.R. Perfit. Vapour undersaturation in primitive mid-ocean-ridge basalt and the volatile content of Earth's upper mantle. *Nature*, 419:451–455, 2002.

C. Sagan and G. Mullen. Earth and mars: evolution of atmospheres and surface temperatures. *Science*, 177:52–56, 1972.

S. Scheiter, S.I. Higgins, C.P. Osborne, C. Bradshaw, D. Lunt, B.S. Ripley, L.L. Taylor, and D.J. Beerling. Fire and fire-adapted vegetation promoted C4 expansion in the late Miocene. *New Phytologist*, 195:653–666., 2012.

M. Schidlowski. A 3,800-million-year isotopic record of life from carbon in sedimentary rocks. *Nature*, 333:313–318, 1988.

M. Schidlowski. Evolution of the sulphur cycle in the Precambrian. In P. Brimblecombe and A. Yu. Lein, editors, *Evolution of the global biogeochemical sulphur cycle*. John Wiley and Sons Ltd., 1989.

J.W. Schopf. Earths earliest biosphere: status of the hunt. In P. G. Eriksson, W. Altermann, D. R. Nelson, W. U. Mueller, and O. Catuneanu, editors, *The Precambrian Earth: tempos and events*, page 516539. Elsevier., New York, NY, 2004.

J.W. Schopf. Fossil evidence of Archaean life. *Phil. Trans. R. Soc. B*, 361: 869–885, 2006.

J.W. Schopf, A.B. Kudryavtsev, A.D. Czaja, and A.B. Tripathi. Evidence of Archean life: Stromatolites and microfossils. *Precambrian research*, 158: 141–155, 2007.

D. Schwartzman. *Life, temperature and the Earth*. Columbia University Press, 1999.

A.C. Scott and I.J. Glasspool. The diversification of Paleozoic fire systems and fluctuations in atmospheric oxygen concentration. *PNAS*, 103:10861–10865, 2006.

A.C. Scott and I.J. Glasspool. Observations and experiments on the origin and formation of inertinite group macerals. *Int. J. Coal Geol.*, 70:53–66, 2007.

C. Scott, T.W. Lyons, A. Bekker, Y. Shen, S.W. Poulton, X. Chu, and A.D. Anbar. Tracing the stepwise oxygenation of the Proterozoic ocean. *Nature*, 452:456–459, 2008.

J.H. Seo, M. Guillong, and C.A. Heinrich. The role of sulfur in the formation of magmatic-hydrothermal copper-gold deposits. *Earth and Planetary Science Letters*, 282:323–328, 2009.

A.L. Sessions, D.M. Doughty, P.V. Welander, R.E. Summons, and D.K. Newman. The continuing puzzle of the great oxidation event. *Current Biology*, 19:R567R574, 2009.

L.F. Shampine and M.W. Reichelt. The Matlab ODE suite. *SIAM J. Sci. Comput.*, 18:122, 1997.

L.F. Shampine, I. Gladwell, and S. Thompson. *Solving ODEs with Matlab*. Cambridge University Press, New York, 2003.

N.J. Shaviv and J. Veizer. Celestial driver of Phanerozoic climate? *GSA Today*, 13(7):410, 2003.

N.D. Sheldon. Precambrian paleosols and atmospheric CO_2 levels. *Precambrian research*, 147:148–155, 2006.

N.D. Sheldon and M.T. Hren. Extensive life on land 1.1 Ga ago (conference paper). *22nd annual V. M. Goldschmidt Conference*, 2012.

G. Shields and J. Veizer. Precambrian marine carbonate isotope database: Version 1.1. *G3*, 3(6), 2002.

G.A. Shields. Neoproterozoic cap carbonates: a critical appraisal of existing models and the plumeworld hypothesis. *Terra Nova*, 17(4):299–310, 2005.

G.A. Shields. A normalised seawater strontium isotope curve: possible implications for Neoproterozoic-Cambrian weathering rates and the further oxygenation of the Earth. *eEarth*, 2:35–42, 2007.

G.A. Shields, M. Deynoux, S.J. Culver, M.D. Brasier, P. Affaton, and D. Vandamme. Neoproterozoic glaciomarine and cap dolostone facies of the southwestern Taoudeni Basin (Walidiala Valley, Senegal/Guinea, NW Africa). *External geophysics, Climate and Environment*, 339:186–199, 2007.

G. Shields-Zhou and L. Och. The case for a Neoproterozoic oxygenation event: Geochemical evidence and biological consequences. *GSA Today*, 21:4–11, 2011.

S. Sitch, B. Smith, I.C. Prentice, A. Arneth, A. Bondeau, W. Cramer, J.O. Kaplan, S. Levis, W. Lucht, and M.T. Sykes. Evaluation of ecosystem dynamics, plant geopgrahy and terrestrial carbon cycling in the LPJ dynamic global vegetation model. *Global Change Biology*, 9:161–185, 2003.

N.H. Sleep and K. Zahnle. Carbon dioxide cycling and implications for climate on ancient Earth. *Journal of Geophysical Research*, 106(E1):1373–1399, 2001.

R.J. Spencer and L.A. Hardie. Control of seawater composition by mixing of river waters and mid-ocean ridge hydrothermal brines. In R. J. Spencer and M. Chou, I, editors, *Fluid-mineral interactions: A tribute to H. P. Eugster*, volume 19, pages 409–419. Geochemical Society Special Publication, 1990.

W.N. Stewart and G.W. Rothwell. *Paleobotany and the Evolution of Plants*. Cambridge University Press, New York, 1983.

Y. Su and C.H. Langmuir. *Global MORB chemistry compilation at the segment scale. (MS thesis)*. PhD thesis, Columbia University, 2003.

R.E. Summons, L.L. Jahnke, J.M. Hope, and G.A. Logan. 2-methylhopanoids as biomarkers for cyanobacterial oxygenic photosynthesis. *Nature*, 400: 554–557, 1999.

E. Szathmry and J. Maynard Smith. The major evolutionary transitions. *Nature*, 374:227232., 1995.

Y. Tardy, R. N'Kounkou, and J.-L. Probst. The global water cycle and continental erosion during Phanerozoic time (570 my). *American Journal of Science*, 289:455–483, 1989.

K. Thonicke, A. Spessa, I.C. Prentice, S.P. Harrison, L. Dong, and C. Carmona-Moreno. The influence of vegetation, fire spread and fire behaviour on biomass burning and trace gas emissions: results from a process-based model. *Biogeosciences*, 7(6):1991–2011, 2010.

M.M. Tice and D.R. Lowe. Photosynthetic microbial mats in the 3,416-myr-old ocean. *Nature*, 431:549–552, 2004.

M.M. Tice and D.R. Lowe. Hydrogen-based carbon fixation in the earliest known photosynthetic organisms. *Geology*, 34:37–40, 2006.

J. Van der Burgh, H. Visscher, D.L. Dilcher, and W.M. Krschner. Paleoatmospheric signatures in neogene fossil leaves. *Science*, 260:17881790, 1993.

R.D. van der Hilst, S. Widiyantoro, and E.R. Engdahl. Evidence for deep mantle circulation from global tomography. *Nature*, 386:578–584, 1997.

P. VanCappellen and E.D. Ingall. Benthic phosphorus regeneration, net primary production, and ocean anoxia - a model of the coupled marine biogeochemical cycles of carbon and phosphorus. *Paleoceanography*, 9(5): 677–692, 1994.

P. VanCappellen and E.D. Ingall. Redox stabilization of the atmosphere and oceans by phosphorus-limited marine productivity. *Science*, 271(5248): 493–496, 1996.

D. Vance, D.A.H. Teagle, and G.L. Foster. Variable quaternary chemical weathering fluxes and imbalances in marine geochemical budgets. *Nature*, 458:493–496, 2009.

J. Veizer, D. Ala, K. Azmy, P. Bruckschen, D. Buhl, F. Bruhn, G.A.F. Carden, A. Diener, S. Ebneth, Y. Godderis, T. Jasper, C. Korte, F. Pawellek, O.G. Podlaha, and H. Strauss. $^{87}Sr/^{86}Sr$, $\delta^{13}C$ and $\delta^{18}O$ evolution of Phanerozoic seawater. *Chemical Geology*, 161:59–88, 1999.

J. Veizer, Y. Godderis, and L.M. Francois. Evidence for decoupling of atmospheric CO_2 and global climate during the Phanerozoic Eon. *Nature*, 408: 698–701, 2000.

W.F. Vincent and C. Howard-Williams. Life on snowball Earth. *Science*, 287, 2000.

T. Volk. Feedbacks between weathering and atmospheric CO_2 over the last 100 million years. *American Journal of Science*, 287:763–779, 1987.

T. Volk. Sensitivity of climate and atmospheric CO_2 to deep-ocean and shallow-ocean carbonate burial. *Nature*, 337:637–939, 1989.

G. Wachtershauser. Origin of life in an iron-sulfur world. In A. Brack, editor, *The molecular origins of life: assembling the pieces of the puzzle*, page 206218. Cambridge University Press., Cambridge, UK, 1998.

J.C.G. Walker, P.B. Hays, and J.F. Kasting. A negative feedback mechanism for the long-term stabilization of Earth's surface temperature. *Journal of Geophysical Research*, 86(C10):9776–9782, 1981.

M.M. Walsh. Microfossils and possible microfossils from the Early Archean Onverwacht Group, Barberton Mountain Land, South Africa. *Precambrian research*, 54:271–292, 1992.

M.M. Walsh and D.R. Lowe. Filamentous microfossils from the 3500 Myr-old Onverwacht Group, Barberton Mountain Land, South Africa. *Nature*, 314: 530532., 1985.

M.J. Walter, S.C. Kohn, D. Araujo, G.P. Bulanova, C.B. Smith, E. Gaillou, J. Wang, A. Steele, and S.B. Shirey. Deep mantle cycling of oceanic crust: Evidence from diamonds and their mineral inclusions. *Science*, 334:54–57, 2011.

Y. Watanabe, J.E.J. Martini, and H. Ohmoto. Geochemical evidence for terrestrial ecosystems 2.6 billion years ago. *Nature*, 408:574–578, 2000.

A. Watson, J.E. Lovelock, and L. Margulis. Methanogenesis, fires and the regulation of atmospheric oxygen. *BioSystems*, 10:293–298, 1978.

A.J. Watson. *Consequences for the biosphere of forest and grassland fires*. PhD thesis, U. Reading., 1978.

A.J. Watson and J.E. Lovelock. Biological homeostasis of the global environment: the parable of Daisyworld. *Tellus*, 35B:284–289, 1983.

A.J. Watson and J.E. Lovelock. The dependence of flame spread and probability of ignition on atmospheric oxygen: an experimental investigation. In C.M. Belcher, editor, *Fire Phenomena and the Earth System: An Interdisciplinary Guide to Fire Science*. Wiley Blackwell., in press.

C.H. Wellman and J. Gray. The microfossil record of early land plants. *Phil. Trans. R. Soc. B*, 355:717–732, 2000.

C.H. Wellman, P.L. Osterloff, and U. Mohiuddin. Fragments of the earliest land plants. *Nature*, 425:282–285, 2003.

A.J. West. Mountains and monsoons. *Nature Geoscience*, 1(12):814–815, 2008.

A.J. West. Snowballs limited by weathering. *Nature Geoscience*, 4:824–826, 2011.

A.J. West, A. Galy, and M. Bickle. Tectonic and climatic controls on silicate weathering. *Earth and planetary science letters*, 235:211–228, 2005.

A.J. West, J. Hartmann, N. Moosdorf, R. Lauerwald, S. Cohen, and A. Kettner. Steps towards a global chemical weathering model framework: The role of erosion and supply limitation (conference paper). *22nd annual V. M. Goldschmidt Conference*, 2012.

C.G. Wheat, J. McManus, M.J. Mottl, and E. Giambalvo. Oceanic phosphorus imbalance: Magnitude of the mid-ocean ridge flank hydrothermal sink. *Geophysical Research Letters*, 30:1895, 2003.

S.A. Wilde, J.W. Valley, W.H. Peck, and C.M. Graham. Evidence from detrital zircons for the existence of continental crust and oceans on the Earth 4.4 Gyr ago. *Nature*, 409(11):175–178, 2001.

R.A. Wildman, L.J. Hickey, M.B. Dickinson, R.A. Berner, J.M. Robinson, M. Dietrich, R.H. Essenhigh, and C.B. Wildman. Burning of forest materials under late Paleozoic high atmospheric oxygen levels. *Geology*, 32: 457–460, 2004.

B.H. Wilkinson and B.J. McElroy. The impact of humans on continental erosion and sedimentation. *Geological Society of America Bulletin*, 119: 140–156, 2007.

J.K. Willenbring and F.v. Blanckenburg. Long-term stability of global erosion rates and weathering during late-Cenozoic cooling. *Nature*, 465:211–214, 2010.

H.M. Wilson and L.I. Anderson. Morphology and taxonomy of Paleozoic millipedes (Diplopoda: Chilognatha: Archipolypoda) from Scotland. *Journal of Paleontology*, 78(1):169–184, 2004.

C.J. Yapp and H. Poths. Ancient atmospheric CO_2 pressures inferred from natural goethites. *Nature*, 355:342344, 1992.

K. Zahnle, N. Arndt, C. Cockell, A. Halliday, E. Nisbet, F. Selsis, and N.H. Sleep. Emergence of a habitable planet. *Scpace Science Review*, 129:35–78, 2007.

Q. Zhang, X. Chu, and L. Feng. Discussion on the Neoproterozoic glaciations in the South China Block and their related paleolatitudes. *Chinese Science Bulletin*, 54(10):1797–1800, 2009.

M. Zhu, J. Zhang, and A. Yang. Integrated Ediacaran (Sinian) chronostratigraphy of South China. *Palaeogeography Palaeoclimatology Palaeoecology*, 254:7–61, 2007.